University of Virginia

Department of Mechanical and Aerospace Engineering

Doctor of Philosophy Dissertation

Radiative Contributions to Interfacial Thermal Transport

William Hutchins

Advisory Committee:

Prof. Chloe Dedic, *Chair*
Prof. Patrick E. Hopkins, *Advisor*
Prof. Ethan A. Scott
Prof. Jon Ihlefeld
Dr. Paul Danehy

May 2025

APPROVAL SHEET

The dissertation is submitted in partial fulfillment of the
requirements for the degree of

Doctor of Philosophy in Mechanical and Aerospace Engineering

William David Hutchins

This dissertation has been read and approved by the Examining Committee:

Patrick E. Hopkins, Advisor

Chloe Dedic, Chair

Jon F. Ihlefeld

Ethan A. Scott

Paul M. Danehy

Accepted for the School of Engineering and Applied Science:

Jennifer L. West, Dean
School of Engineering and Applied Science
April, 4 2025

Abstract

The continual drive for nanoscale electronic devices to shrink toward atomic length scales poses direct challenges to both our understanding of thermal processes and our implementation of heat dissipation techniques. At the nanoscale, not only does the power density forced through semiconductor devices increase, but the laws that govern thermodynamic processes begin to fail. In conventional theory, thermal transport in solids is mediated by vibrational resonances and electromagnetic waves, phonons and electrons, which store and propagate heat energy within the stretching of crystal bonds and electric charge. Focusing down beneath the characteristic length scale of the average carrier exchange, thermal gradients and even temperatures begin to take on different definitions. It is at these length scales where the intrinsic property of a material to dissipate heat energy, that is *thermal resistance*, becomes restricted by the boundaries of the system and understanding how to move heat across these boundaries is a major obstacle when engineering and designing microelectronics.

Typically, it is thought that the flow of phonons, or conductive transport, across interfaces dominates over any other thermal process, such as radiation or convection. However, recent innovations in calculating radiation across nanometer-scale vacuum gaps in several measurements have begun to challenge that claim. Some measurements show that the evanescent light available at distances below the Wien's Law characteristic wavelength can transmit fluxes that rival conduction.

The main driver in these intense fluxes is phonon resonances in the mid-infrared (MIR) spectral region, so-called optical phonons. Conductively speaking, because of their low group velocity, optical modes are often assumed to negligibly contribute to thermal conductivity. However, when exposed to the intense flux of near field radiation, these MIR oscillations can resonate with light and produce quasi-particles, a.k.a. polaritons, which are accelerated well beyond their group velocity. The investigation of these emergent quasi-particles is a highly active field of research in optics;

most experimental studies neglect their contribution to thermal transport processes.

The goal of this thesis is to investigate how thermal energy can be transmitted by light across solid state interfaces via near-field transport of evanescent radiation. To this end, I will characterize and quantify the thermal transport processes such as thermal boundary conductance (TBC), radiative flux, mode-specific conductance, and polariton velocity at non-equilibrium interfaces in polaritonic systems. To begin, I will develop a theoretical framework for predictions of near-field radiative transport in solid state non-equilibrium systems. I will then design an experimental technique to probe thermally excited polaritonic modes. To demonstrate this effect, I will explore near-field radiative transport from a gold radiator into hexagonal boron nitride (h-BN). I will then engineer an ideal system to quantify the speed at which these modes travel while carrying heat in a cadmium oxide (CdO) structure, while demonstrating a mechanism for an ultrafast heat sink and thermal rectification.

Acknowledgments

You investigate for curiosity, because it is unknown, not because you know the answer.

— **Richard Feynman**, The Pleasure of Finding Things Out

I have been so fortunate to develop my thesis as an exercise in curiosity, just asking questions and solving puzzles. I would not be so lucky without all the people who have given me the freedom and inspiration to develop any of the half-baked ideas that I might have into real research. I would need another thesis just to detail all the nudges which have guided me to this point

From the top, I owe a huge thank you to my advisor, Dr. Patrick Hopkins. His patience, off-hours calls to iron out a scientific idea, and overall passion for discovery have left a massive impact on whom I have become as a scientist. When I stepped foot into "Headquarters" he greeted me with a story of his curiosity that launched me over the edge into discovering my own and joining the ExSiTE lab. His enthusiasm and confidence eventually ended up rubbing off on me; that and his mentorship are among my most valuable assets.

A student is only as great as his teachers and I have been graced with some of the best, all the way from Mrs. Sutton's science class to Mrs. Cullison's English course; each one of my teachers has instilled wisdom in me that I will never forget. This is especially the case for those professors serving on my committee. I'm so grateful to Dr. Dedic and Dr. Ihlefeld for showing me the intricate and fascinating worlds of optics and solid-state physics. Thank you, Dr. Scott, for helping me organize my thoughts and work when things get a bit too confusing. Finally, to one of my greatest teachers who has never assigned me homework, Dr. Paul Danehy, thank you for believing in my academic dreams even more than I did at some points. Your advice every step of the way has been precisely what I needed to hear at those moments.

Of course, my time here at UVA would not have been nearly as rewarding without the wonderful ExSiTE lab that Patrick has cultivated. I've lost count of how many experimental stresses I

have decompressed just by venting on a walk to Starbucks with Dan and Sara in between hours of aligning, or how many research rabbit holes I've been 'nerd-sniped' into from harmless heat transfer discussions I've had with Thomas or Saman. I know that without the morning workouts with Rafiqul, the motorcycle rides with Hunter and Will, or the occasional weekend tailgate with Emma, I would have gone stir-crazy in that basement! Thank you, guys, for everything! Just know that at the very least you have a lifetime collaborator and friend in me.

Finally, I could not have done it without the steadfast support of my family, Carol (Nanny), Bruce (Pop pop), and Spaz; I know I might be difficult to get in contact with while I am in the basement messing around with lasers all week, but just know that the stability of knowing you all are there for me settles my anxious heart, not to mention the advice and encouragement you all provided to me through every stage of my life, shaping me into the man I am today. Thank you so much. Any success I have achieved is a direct result of their love, patience, and life lessons. Last but certainly not least, to my best friend and girlfriend Yadeliz, thank you for always keeping me driven and relaxed, even when I feel like I have lost my way. These past few years have been incredible. Without your encouragement, humor and joy, this PhD would not have been completed.

Contents

List of Figures

List of Tables

Chapter 1

Background and Motivation

In the first few decades of the 21st century, technological advancement has been at a fever pitch, developing ever smaller electronics dropping the scale of a single transistor to < 5 nm [1], which is the size of 10 atoms [2, 3]. In terms of engineering, this pace of innovation requires a profound understanding of how to manage the heat at nanoscale regimes [4, 5]. At these scales, the average mean free path of heat carriers can be an order of magnitude longer than the critical dimension. The traditional model used to predict heat transfer and temperature rises in integrated circuits and transistors is Fourier's Law [6], which describes the heat flux, q [W m^{-2}], as:

$$q = -\kappa \nabla T \tag{1.1}$$

where ∇T [m^{-1} K] is the vector form of the thermal gradient present in the medium, and κ [W m^{-1} K^{-1}]is the thermal conductivity of the material. Thermal conductivity is an intrinsic material property that quantifies the ability of a material to sustain and transmit thermal currents. By the definition of temperature, there must be a local thermodynamic equilibrium established within the medium to assume Eq. 1.1 is valid [7]. However, during operation heat carriers may be ballistic with respect to the boundaries and therefore cannot establish a gradient, and thus the Fourier law fails. As a result, to keep up with the decreasing dimensions of devices, we must have a more intricate map of thermal processes at boundaries that restrict heat flow.

The forced scattering of carriers at the interface between two media provides its own bottleneck to thermal transfer. In fact, at these nanoscale dimensions, the resistance at the interface R_{bd}[W^{-1} m^2 K] $= 1/h_{\mathrm{bd}}$, where h_{bd} is the thermal boundary conductance, can rival the internal resistance between a source and the interface [8]. This means that within a transistor stack or an integrated circuit package, the interfaces can impose a large hurdle to thermal management [9, 10].

1.1 Motivation

Most of the work on heat transport across interfaces has been focused singularly on the conductive contributions of the phonon-phonon boundary scattering (h_{bd}) and the electron substrate scattering (h_{es}), see Fig. 1.1. However, with the recent developments on the formalism of radiation in the near field, a new opportunity has opened for investigations and optimizations of interfacial heat fluxes under the umbrella of thermal radiative transfer ξ.

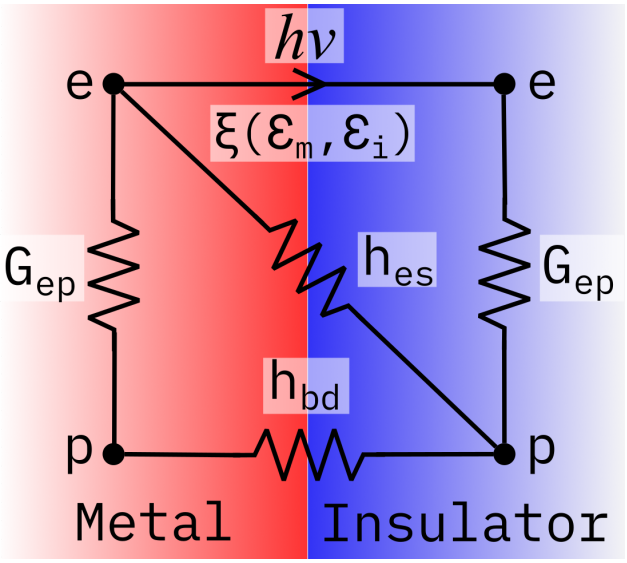

Figure 1.1: **Diagram of the proposed interfacial transport process**. Within each medium, (m)etal or (i)nsulator, the e-p coupling parameter G_{ep} controls the rate by which energy is exchanged within the two thermal baths. Across the metal insulator interface, there are two standard conductive processes: h_{es} the conductance associated with the transition of electronic energy of the metal to the phonons in an insulator, and h_{bd} the phonon-phonon boundary conductance. The mechanism introduced in this proposed work, ξ is the transfer of photonic energy ($h\nu$) across the interface, which depends primarily on the dielectric function of the metal and insulator.

1.1.1 Nanoelectronics

The production of nanoscale electronic devices has surged in the past 20 years with the rise of convenient portable computers and phones. This progress in the development of the field effect transistor has made it possible for intense high-frequency cycles of charging and discharging in transmitters and radars [11]. The fluxes experienced can exceed 1 [kWcm^{-2}] which translates to large thermal gradients throughout a chip [12, 13].

With thermal dissipation being stymied at bottlenecks such as Vias and interfaces within the

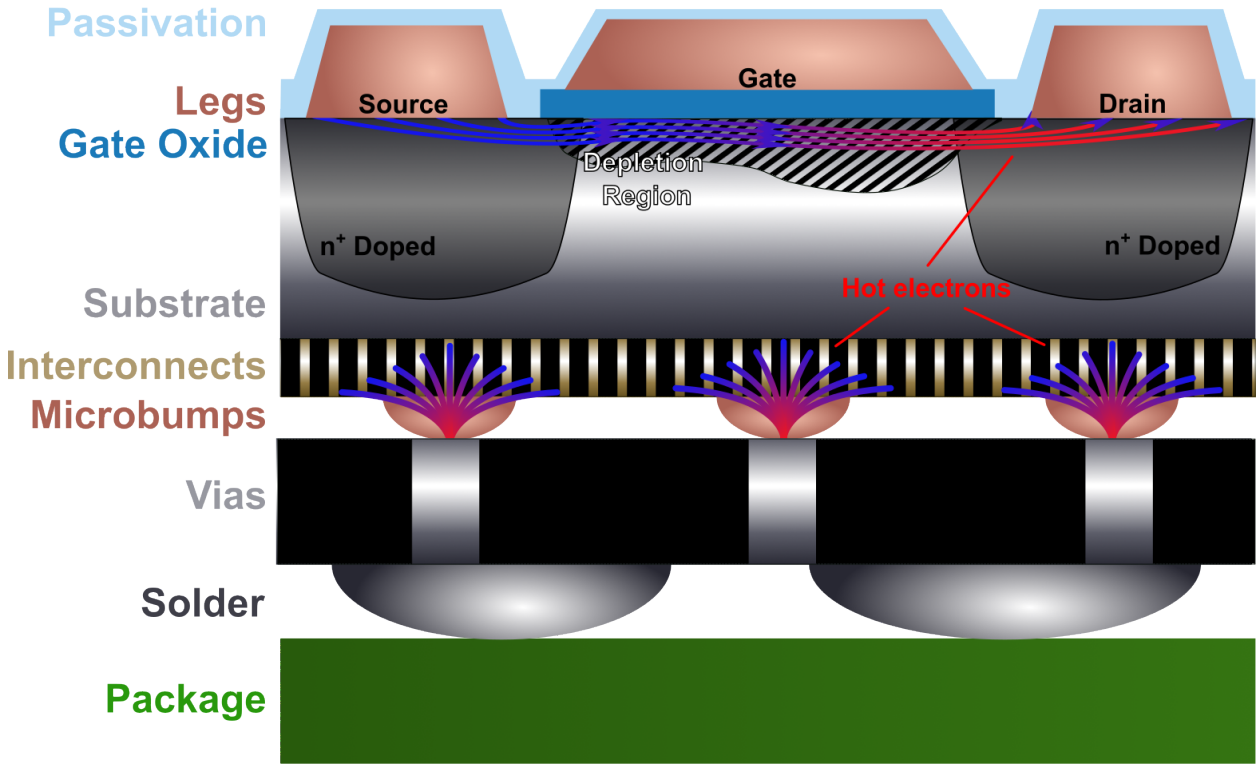

Figure 1.2: **Schematic of a 3D chip stack**. A simplified transistor stack highlighting the many metal dielectric interfaces. Hot electrons both transfer electric information for functional computation and account for a nonequilibrium thermal problem when optimizing the thermal dissipation away from bottlenecks, such as under the gate of a transistor, interconnects, through silicon vias, or at the micorbump/ solder contacts.

transistor geometry, internal sources of heat emerge, increasing operation temperature. Prolonged thermal cycling such as this can cause the overall degradation of the device [14] and even catastrophic failure [15]. This is compounded by next-generation devices stacking transistors in all three dimensions to maintain the rate of innovation [16].

Figure 1.2 is a simplified schematic of such of a chip configuration. At the uppermost level, there is a dielectric passivization layer that serves to reduce the oxidation of the transistor region and electrically insulate the metal legs. Under that would be a series of field-effect transistors (FETs), where hot electrons are shuttled from the source to the drain legs mediated by the gate [17]. Due to the physics of FET devices, the electric field required to activate transmit data trends as ($E \propto \frac{V}{L}$)where V is the voltage from source to drain, and L is the width of the depletion region beneath the gate. This implies that as the gate region is pushed thinner and thinner, the electrons are pushed into a stronger nonequilibrium with higher fluxes [13]. This is the first obstacle

for heat dissipation, the heat that is produced by electrons at the gate contacts and within the semiconductor device must be thermalized with the lattice, and removed through thermally and electrically insulating passivization layers and active device regions. The next layers can be any manner of transistor or RF chips; however, the interconnects and vias between chips and layers highlighted in 1.2, also substantially bottleneck thermal transport. These thin metallic strips and micro-bumps (in some cases much thinner than the mean free path of thermal carriers [18, 19]) direct hot electrons deep within the stack. Entire chips are then soldered to large packages, which can finally efficiently dissipate the heat with bulk fin-type sinks. However, with the current trends within the semiconductor industry, thermal sinks are being pushed further and further away from thermal sources which requires innovative solutions to shuttle the heat across many interfaces as quickly as possible.

1.1.2 Radiative Engineering

In solid-state thermal engineering, the focus of most dissipation efforts have been on maximizing the conductive efficiency. However, recent advancements in radiative techniques present compelling opportunities not only to expel heat [20–23] from the system, but also to harness waste energy for useful work [24–29].

To achieve this, we must engineer the emitted radiation from media and optimize the absorption of the receiver. Radiation is essentially the evaporative cooling of internal energy via the emission of electromagnetic waves. The flux (Q_r) out of a subsystem in local thermodynamic equilibrium and hotter than its surroundings is proportional to the surface area exposed to the surroundings (A) and the quartic difference of the system temperature (T) and the surroundings' temperature (T_s), described by the Stefan-Boltzmann Law [30]:

$$Q_r = \sigma \epsilon A (T^4 - T_s^4) \tag{1.2}$$

where the constant of proportionality (σ) is the Stefan-Boltzmann constant, and ϵ describes the spectral emission character of a sample where $\epsilon = 1$ is the perfect emitter, the so called black-body. Interestingly, a radiating system can be isolated from both the conductive and convective processes of heat transport. However, as radiation comes from the internal oscillations of a system, it is

ever-present even within the vacuum.

Due to the speed of light, the energy of internal oscillations of a media can only be emitted at set frequencies and momenta. The spectral distribution of the emitted radiation is given by Kirchhoff's law [31], which is precisely the absorbance of the system, and can be calculated from the dielectric function as one minus the reflectivity (1-R), assuming an opaque material at normal incidence. However, this simple parameter is not the entire picture. We are implicitly assuming that the emitted energy can propagate in the surrounding medium. For example, consider a system at a set temperature embedded in a material of near perfect reflectance, i.e. $= (1 - R) \ll 1$; we cannot expect that the internal thermal energy of the system will ever be emitted to its surroundings. We thus introduce the idea that there can be modes of light that should contribute to thermal emission, but do not because they are disallowed by an interface based on dielectric mismatch. The converse of this argument can also be extended to a material/vacuum interface. The radiative implications of these disallowed modes are explored in the works of Greffet [32] and Zare [33]. They prove that, by tuning the surface of an emitter, we can engineer thermal emission; however, we should not limit ourselves to the allowed wave-vectors, but push the limits of the entire dispersion of light available as distances shrink below the wavelength of emission. These intense evanescent modes are the foundation of thermal rectifiers [23] and thermo-photovoltaic(TPV) cells [27].

An example of a TPV cell is provided in Figure 1.3. These devices leverage the tunable emission from a surface that is maintained at a high temperature for some useful purpose or consequence (the walls of a foundry, or internals of a combustion chamber [34]). By applying a photonic pattern to the emitting surface, the spectrum of not only propagating photons, but also evanescent photons may be engineered to match the absorption profile of a photovoltaic(PV) cell [35]. The PV cell may work in the standard p-n junction configuration [36], but is often also spectrally tuned to maximize the voltage across the device. This beautiful solution is deriving order and work from the chaos of high entropy waste heat. There is one design consideration of such devices that has extremely limited the scope of current implementation, which is not immediately obvious in Fig. 1.3. To maximize the intensity of evanescent radiation, while not losing large temperature differences to conductive transport, devices are designed with a nanometer scale vacuum gap [37, 38] between the emitter and the TPV cell. We can devise fully solid-state devices which both exhibit near field enhancement and remain simple to manufacture, only by tuning the transmission spectrum of a

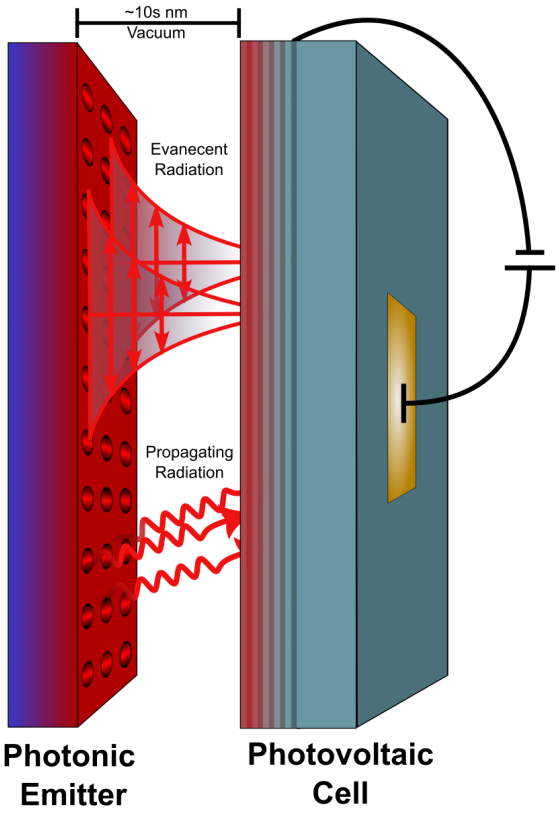

Figure 1.3: **Schematic of a Thermo-photovoltaic**. A sample diagram of a thermo-photovoltaic device for harvesting waste heat energy. The emitter is often heated passively with auxiliary processes, and the emitting surface is patterned to spectrally tune the emission in line with the photovoltaic cell. The cell is a stack of dielectric thin films that absorb the near and far field emissions from the emitter and convert the optical energy into electronic energy.

transparent thermally insulative interlayer.

1.2 Outlines and Objectives

This Dissertation investigates the role of radiation at the interface of two solid media. The major thrust of this work will focus on polaritonic absorption and the contribution of near field thermal emission to the conductance across a metal-dielectric interface. The second thrust will be the design and use of pump probe methodologies to investigate ultrafast thermal transport events within specific carrier sub-systems via spectral tunability.

- Chapter 2, *Heat transport, Phonons, and the Dielectric function*: The fundamentals of solid state thermal transport and radiation are discussed with emphasis on the role of heat carriers

and their dispersion. A general description of the dielectric function is offered along with the relationship of the dispersion of heat carriers and the resultant coupled particles.

- Chapter 3, *Experimental Design and Simulations*: The relevant design of experimental procedures to investigate thermal processes is provided to address the principal thrusts of this work. An introduction to each thermal and optical simulation is detailed, focusing on the interpretation of experimental results.

- Chapter 4, *Interfacial Heat Transport via Evanescent Radiation by Hot Electrons*: Predictions of an additional thermal transport pathway across metal/non-metal interfaces with large electron-phonon nonequilibrium via evanescent radiative heat transfer are made. In such systems, electron scattering processes vary drastically and can be leveraged to guide heat across interfaces via radiative heat transport without engaging the lattice directly. The formalism of fluctuational electrodynamics to simulate the spectral radiative heat flux across the interface of a metal film and a non-metal substrate is expanded to encompass interfacial near field transport at electron-phonon nonequilibrium.

- Chapter 5, *Thermoreflectance of optical phonon resonances*: Analytically quantify and experimentally measure the thermoreflectance coefficient associated with optical phonon resonances through ultrafast pump–probe measurements and variable angle spectroscopic ellipsometry. Due to the intensity of modes in the mid-wave Infrared region, the thermoreflectance coefficient, $\frac{dR}{dT}$, of SiO_2, SiC, and AlN can exceed the thermoreflectance of metal transducers in the visible range. This result opens the door for in-situ thermal characterization of dielectrics and spectrally tuned transient thermoreflectance pump probe measurements.

- Chapter 6, *Demonstration of the thermal excitation of polaritons*: A demonstration of a new avenue for interfacial heat transfer based on broadband radiative coupling from a hot spot in a gold film to hBN via hyperbolic phonon polaritons is presented. This, being the first direct experimental evidence for both the thermal excitation of phonon polaritons and interfacial radiative heat transport, resulted in the confirmation of the calculations described in Chapter 4.

- Chapter 7, *Engineering ultrafast thermal tunneling*: The prospect of the utilization of the

interfacial transport via meta-material engineering is explored. The propagation speeds of thermally dominant optical modes are extracted from the spectrally tuned transient thermoreflectance. Radiative interface conductance is extended to interfacial interlayer for use as an ultrafast thermal diode and more comprehensive solid-state radiative devices.

- Chapter 8, *Summary, Relevance, and Future Directions*: In this chapter, the relevant findings are summarized, and the scientific impact of the dissertation is outlined. Some of the future experiments, and follow-up studies which would extend the findings of this work, are provided. Investigating these would shed light on the conclusions presented here and help engineer device level applications of the solid-state interfacial radiative process.

Chapter 2

Concepts of Solid State Thermal Transport

Fundamentally, the transfer of thermal energy can be classified into three mechanisms: *conduction*, *convection*, and *radiation*. Conduction describes the transfer of thermal energy through the random motion of energy carriers, namely, phonons and electrons, which propagate within solid-state media and across interfaces via energy carriers. In contrast, convection distinguishes how heat can be exchanged though intermolecular collisions within fluids at surfaces. Finally, radiation is the emission of thermal energy as electromagnetic waves, present in all media. This dissertation serves as a bridge between conduction and radiation, as such this chapter serves as a brief introduction to the concepts of thermal transport.

2.1 Conduction

In cases of thermal nonequilibrium, we must rely on the heat diffusion equation:

$$C_v \frac{\partial T}{\partial t} = \nabla \cdot (\kappa \nabla T) + Q_{\text{source}} \tag{2.1}$$

where C_v is the volumetric heat capacity of the material, t is time and Q_{source} is any thermal source that generates heat within the closed system. Fourier's Law given in the previous chapter is a simplification of the heat diffusion equation when $t \to \infty$, the steady state limit. In this regime, the effect of thermal capacitance on thermal transport is negligible and thus, Eq. 2.1 reduces to Eq. 1.1.

The two key parameters in the heat equation above are: thermal conductivity and heat capacity. Thermal conductivity can be derived from the basic thermodynamics of ideal gasses, so-called kinetic theory [31],

$$\kappa = \frac{1}{3} C_v v \lambda = \frac{1}{3} C_v v^2 \tau \tag{2.2}$$

where v is the velocity of the carrier and λ is the mean free path that a carrier travels between successive collisions while propagating. Similarly, τ is the time between successive collisions, the so-called relaxation time, where $\tau = v/\lambda$. Due to the complexity of scattering processes present within a medium, it is common to apply Mathiesson's rule [31] to the carrier lifetime, such that the total lifetime is given by the inverse sums of the lifetimes of known independent sub-processes or $\tau_{\text{total}}^{-1} = \tau_a^{-1} + \tau_b^{-1} + \dots$.

Finally, for the sake of completeness, the heat capacity of a carrier, C_c, can be defined from basic thermodynamics

$$U_c = \int_\epsilon \epsilon \mathcal{D}_c f_c d\epsilon \tag{2.3a}$$

$$C_c = \frac{\partial U}{\partial T} \tag{2.3b}$$

where $\mathcal{D}$ and f are the amount and the distribution of carriers, at a given energy ϵ. $\mathcal{D}$, the density of states, can be found, assuming we know the dispersion relation between the frequency (ω) and wavevector (k) of the energy carrier, by summing the number of states that exist in a $N-1$ dimensional space with thickness dk per unit cell of momentum space L^N, where N is the dimension the carrier propagates in. Put simply, if we assume a 3D system, we need to consider the number of states contained within a two-dimensional surface in k-space multiplied by the thickness dk per unit volume L^3. f is determined by the unique statistics of each carrier subsystem. Now, using the first law of thermodynamics*, the isochoric heat capacity for any system is defined as:

$$C_v = \left.\frac{\partial Q}{dT}\right|_{V=const.} = \left(\frac{\partial U}{\partial T}\right)_V = \int_0^\infty \frac{\partial f(\epsilon)}{\partial T} \cdot \epsilon D(\epsilon) d\epsilon \tag{2.4}$$

The following two sections will detail the derivation of the thermal statistics and transport properties for the two most common thermal baths, the vibrations of the lattice sites, *phonons*, and the

*The first law of thermodynamics requires that dU = ∂Q - ∂W; where the change in internal energy, dU, is related to the change in the heat of the system, ∂Q, minus the work done to or performed by the system, ∂W. In an isochoric process, no work is done, thus, $dU = \partial Q$

motion of free charges, *electrons*.

2.1.1 Phonons

In non-metal systems, the principal energy carriers are phonons. The wave-like collective vibrations of lattice sites around their equilibrium positions. The preferred modes of these vibrations are quantized into bands, called phonons. Originally proposed by Einstein [39], phonons can behave as both waves and particles propagating through a lattice as in Fig. 2.1

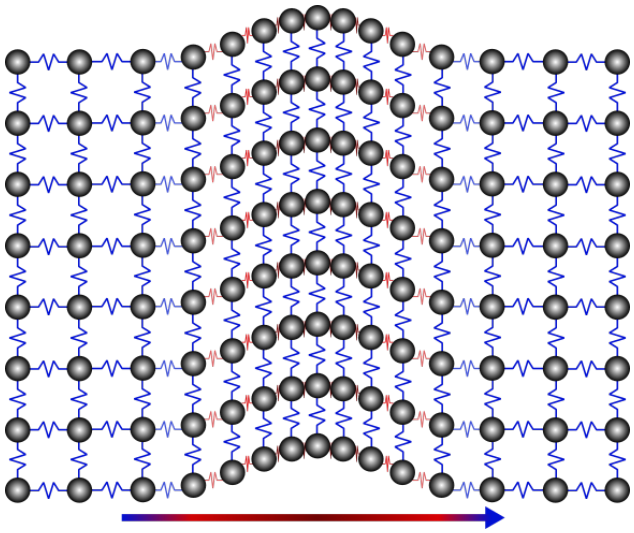

Figure 2.1: **Phonon Propagation**: Heat is stored within the energy of the tension and compression of bonds between lattice sites.

The dispersion of phonons, relates the frequency of a given phonon mode, ω, to a wavevector, $k = 2\pi/\lambda$. As we are attempting to describe the propagation of heat, we must consider the equations of motion for any one lattice position in a crystal. The most common simplification in this regard is the assumption of a 1D chain of lattice positions. In other words, a lattice consisting of only the top layer of depiction in Fig. 2.1. We then assign each lattice site, j, with some weight, M, separated by the lattice constant, a, and the bonds between each lattice position having some elasticity described as a spring with force constant, K. Then, summing the forces on any site returns,

$$F_j = K(u_{j+1} - u_j) + K(u_{j-1} - u_j) \tag{2.5}$$

where $u_j = x_j - x_j^0$ is the displacement of the lattice site away from its equilibrium position x_j^0. We can then apply Newton's Second Law for the differential equation of motion:

$$M\ddot{u}_j = K(u_{j+1} - u_j) + K(u_{j-1} - u_j) \tag{2.6}$$

where $\ddot{u}_j$ is the second time derivative of u_j, acceleration. We can assume the solution to the above equation takes the form

$$u_j \propto e^{i(jka-\omega t)} \tag{2.7}$$

where, ω and k are exactly the frequency and wavevector described above. Furthermore, we can then apply this solution to the equation of motion in 2.6 to get,

$$M\omega^2 = 2K(1 - \cos(ka)) \tag{2.8}$$

Thus, when solving for $\omega(k)$ the dispersion relation is found for a 1D chain as

$$\omega(k) = 2\sqrt{\frac{K}{M}}\left|\sin\left[\frac{1}{2}ka\right]\right| \tag{2.9}$$

we need only consider the solutions to Eq. 2.9 when k is within $\pm\,\pi/a$, as this is the period of the mode; in other words, the solutions to Eq. 2.9 do not change under the substitution $k = k + 2\pi n/a$ for any integer n. This periodicity is integral to the band structure of vibrational modes when increasing the 1D solution to higher dimensions, therefore, the reciprocal lattice vector ($b = 2\pi/a$) is often used instead of the real space lattice vector, a. All vibrational information is contained within this range of $\pm b/2$, referred to as the Brillouin zone. A graph of the dispersion relation for the case of a mono-atomic lattice is provided in Fig. 2.2a

Phonon dispersions describe two critical aspects of phonon modes, which describe the amount of heat energy a phonon can propagate with. Firstly, from the dispersion relation provided in Eq. 2.9, it is apparent that each phonon with energy $E = \hbar\omega$[†] has a distinct momentum, $p = \hbar k$. This may seem obvious, but is important when considering the storage and exchange of energy between the carriers within different bands. Finally, the velocity of a "wave-packet", v_g[‡] propagates at the

[†] $\hbar$, refers to Plank's constant, h, which describes a finite quantum of action [40], reduced by division on 2π.

[‡] Schrödinger used this to describe the groups that emerged when impressing *modulation* on a *carrier* frequency. [41], We can think of these groups more simply as wave pulses.

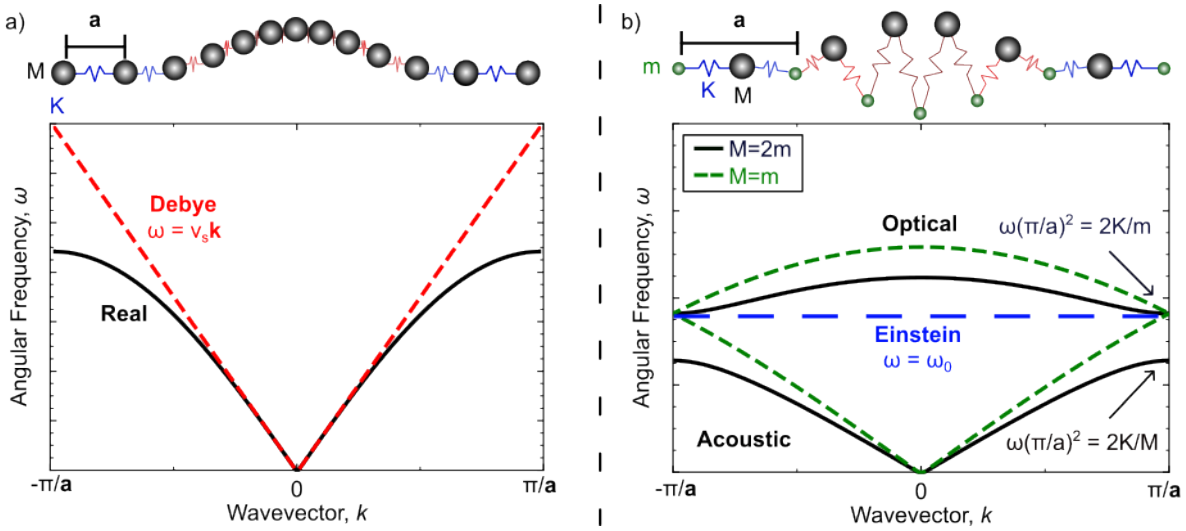

Figure 2.2: **Phonon Dispersion Curves**: calculated for (a) a monoatomic lattice, and (b) a diatomic lattice. These correspond to the solutions to Eq. 2.9 and 2.12, respectively. (a) The "dispersion" associated with the Debye model is also provided which, as shown, over-predicts the velocity of the band near the edge of the Brillouin Zone. (b) Both cases for m=M and m=$\frac{1}{2}$M are provided to show the effective "zone-folding" in the diatomic case, as well as build intuition on the emergence of the opto-acoustic phonon band gap. A close approximation for the dispersion of optical modes is the Einstein model, where the phonon branch exists at the same frequency ω_0 at all wavevectors.

speed:

$$v_g = \frac{\partial \omega}{\partial k} \tag{2.10}$$

the slope of the dispersion curve at some given wavevector. The phonon branch shown in Fig. 2.2a is referred to as an acoustic mode due to it physically describing in-phase vibrations at the center of the Brillouin zone, the speed of which approaches that of the sound speed,v_s.

It is this value which Debye famously made to simplify understanding the dispersion and phonon propagation. Debye assumed that phonons propagate in a perfectly elastic continuous media and therefore all waves propagated at a constant v_s. Thus, the expression of the Debye dispersion is $\omega(k) = v_s k$. We can see from Fig. 2.2a that this approximation far overpredicts the speed and frequency of phonons at wavevectors near the edge of the Brillouin zone, and thus, the Debye approximation is a poor predictor of the propagation of phonons at temperatures where high wavevectors contribute, but when predicting the heat capacity of phonon modes it can be quite powerful.

The two atom basis is of particular interest to the focus of this dissertation, as most semiconductors have a polyatomic basis. The simplest example of a poly-atomic lattice is the two-atom basis shown in Fig. 2.2b where, m, is the mass of a lighter atom and, M, is a relatively heavier mass identical to the one used in the monoatomic chain. To describe the phonons in a diatomic lattice, the dispersion relation can be described by a similar derivation as above in Eq. 2.5-2.6. However, we must alter the lattice vector that describes the periodicity of the "m, M" unit. This new lattice vector A is twice that of the monoatomic lattice vector a. We also must simultaneously solve two coupled equations of motion:

$$M\ddot{u}_j = K(\mathrm{w}_{j+1} - u_j - \mathrm{w}_{j-1}) \tag{2.11a}$$

$$m\ddot{w}_j = K(u_{j+1} - \mathrm{w}_j - u_{j-1}) \tag{2.11b}$$

where w is the displacement of the smaller m mass, and again assuming wavelike solutions to these equations, and solving for ω^2 gives:

$$\omega^2 = K\left(\frac{1}{M} + \frac{1}{m}\right) \pm \left(\left(\frac{1}{M} + \frac{1}{m}\right)^2 - \frac{4}{Mm}\sin^2[kA]\right) \tag{2.12}$$

This dispersion relation, unlike the monoatomic chain, supports two solutions for each wavevector, the lower branch is the acoustic branch and the upper is referred to as the optical branch. The physical picture of the differences in these branches can be seen in the ball and spring cartoons above the phonon dispersion curves in Fig. 2.2a, and b. The acoustic branch is in both the monoatomic and diatomic lattices but is depicted in Fig. 2.2a. The modes at zone center propagate with a $k = 0$ thus by, Eq. 2.9, $\omega = a\sqrt{K/M}k$. In other words, the Debye approximation holds, and the lattice can be approximated as a continuous medium where waves propagate in-phase with each other as sound waves. In the optical phonon shown above the dispersion in Fig. 2.2b above the dispersion, we can see that, every other lattice site moves out of phase with the one before. We call these phonons "optical", as they correspond to the oscillations of small dipoles at the same wavevector and energy as light.

All of the derivations presented here can be extended to three dimensions and anisotropy, but

this process is not always trivial. For each atom in the basis of the crystal, N number of equations will be needed to describe each degree of freedom, where N is the dimensionality of the structure. Thus, the dispersion relation for solutions to the equations of motion have N acoustic branches and $B(N-1)$ optic branches, where B is the number of unique atoms in the basis.

To formalize the phononic system, in thermal transport we will now derive the density of states for an isotropic solid in the third dimension. We will assume a Brillouin zone of size $2\pi/a$ and for simplicity we will construct a unique treatment for the acoustic and optical branches. As alluded to above, the Debye approximation provides a simple and relatively accurate model of the low frequency acoustic modes of a system. Formally, the Debye approximation assumes a linear relationship between frequency and wavevector, the equation in Fig. 2.2a. In three dimensions, we also know that $\mathcal{D}$ represents the number of modes, n, within a spherical shell of thickness dk per unit volume, V, where $V = L^3$. In other words,

$$\mathcal{D}(\omega) = \frac{1}{V}\frac{dn}{d\omega} \tag{2.13}$$

then applying the Debye approximation $\omega = kv_A$ for some acoustic mode A with velocity v_A. We also note that the volume of a phonon mode in k space is $(2\pi/L)^3 = (2\pi)^3/V$. Applying these to Eq. 2.13 for any acoustic branch, A, again gives:

$$\mathcal{D}(\omega) = \sum_A \frac{4\pi k^2 dk/(2\pi/L)^3}{V d\omega} = \frac{2\omega^2}{2\pi^2 v_{TA}}\bigg|_{0\to\omega_{max,TA}} + \frac{\omega^2}{2\pi^2 v_{LA}}\bigg|_{0\to\omega_{max,LA}} \tag{2.14}$$

where v_{TA}, and v_{LA} are the velocities for the longitudinal and transverse branches, respectively. The max evaluation frequencies $\omega_{max,TA}$, and $\omega_{max,TA}$, define the values of each branch at the edge of the Brillouin zone, which under the Debye approximation is $\omega_{max,j} = v_j(6\pi^2 N_a)^{1/3}$, with N_a being the atomic density. [31]

Due to their dispersive nature [42], the optical modes cannot be approximated with the Debye approximation. However, depending on their frequency, these optical modes can contribute significantly to thermal transport both directly and indirectly. The simplest approach to describe the density of these optical modes is following Einstein's model assuming that the phonon mode only exists exactly at a single phonon frequency across all wavevectors, highlighted in the optical modes of Fig. 2.2, implying $\mathcal{D}(\omega) = \delta(\omega_0)$ where, δ is the Dirac-delta function.

This approximation, while useful, neglects the frequency envelope that *real* optical modes occupy. Instead, for a wider optical branch reminiscent of reality, a Lorentzian from is used

$$\mathcal{D}(\omega) = \frac{\Gamma}{\pi\left[(\omega-\omega_0)^2+\Gamma^2\right]} \tag{2.15}$$

where Γ is a dampening term describing the spectral width of a phonon mode. The Lorentzian model here is merely a convenient substitution for Einstein's model[§]. Later, this form will be used in later sections when discussing the line-widths of the optical phonon branches, in Lorentz's original context [43].

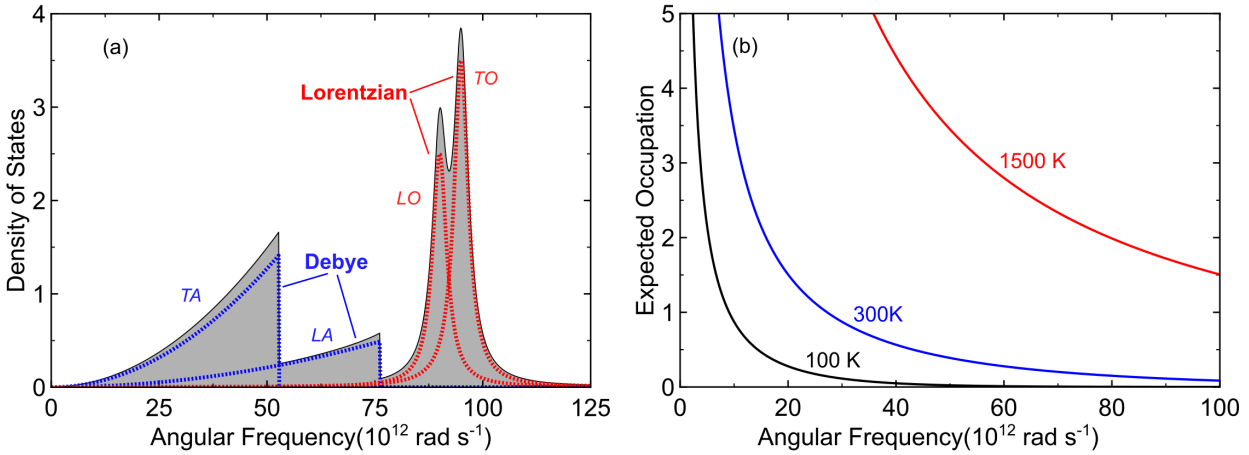

Figure 2.3: **The Density of phononic states and Bose-Einstein distribution**: (a) An example of phonon density of states computed for a sample 3D dipole system. The gray shaded region is the total phonon density of states accounting for all branches. Both transverse acoustics (TA), and the longitudinal (LA) were simulated with the Debye density of states described in Eq. 2.14, with $v_L = 8433$ m s^{-1}, and $v_T = 5843$ m s^{-1}. The optical modes were positioned at $\omega_{\mathrm{TO}} = 95$ THz and $\omega_{\mathrm{LO}} = 90$ THz. The optical modes were simulated as Lorentzians for a more realistic estimation of the Einstein model, with each dampening term was set to 2 THz. (b) The Bose-Einstein distribution Eq. 2.16 computed at T= 100 K (black), 300 K (blue), and 1500 K (red).

Finally, the distribution of phonons varies with temperature based on Bose-Einstein statistics [39, 44]:

$$f_{BE}(\epsilon) = \frac{1}{e^{\frac{\hbar\omega}{k_b T}} - 1} \tag{2.16}$$

where k_b is Boltzmann's constant, which relates the total thermal energy contained in the particles

[§]The Lorentzian, L, is consistent with the Einstein model as $L(\omega)|_{\Gamma\to 0} = \delta(\omega)$

of a gas to the thermodynamic temperature of the ensemble. We can see from Fig. 2.3 that low frequency modes, i.e., acoustics modes, dominate the system at room temperature and therefore, should dominate thermal transport at lower temperatures. We can then plug Eqs. 2.16, 2.15, and 2.14 into Eq. 2.4 ensuring to apply the temperature derivative to the distribution function.

$$C_{v,ph} = \sum_j \int_0^{\omega_{max,j}} \frac{\hbar^2 \omega^4 e^{\frac{\hbar\omega}{k_b T}}}{2\pi^2 k_b T^2 v_j^3 \left(e^{\frac{\hbar\omega}{k_b T}} - 1\right)^2} d\omega \tag{2.17}$$

Finally, the thermal conductivity can be assessed from Eq. 2.2, and the Debye heat capacity:

$$\kappa_{ph} = \frac{1}{3} \sum_j \int_0^{\omega_{max,j}} \mathcal{D}_j(\omega) \frac{\hbar^2 \omega^2 v_j^2 e^{\frac{\hbar\omega}{k_b T}}}{k_b T^2 \left(e^{\frac{\hbar\omega}{k_b T}} - 1\right)^2} \tau_j d\omega \tag{2.18}$$

Each of these expressions should be computed in accordance with the real dispersion, and thus density of states, but the Debye model is a sufficient approximation for first estimates, at low temperatures, where phonons are nearly all zone-center acoustics. τ_j, and v_j are the most notable contributors to the trends in thermal conductivity. The velocity can be simply computed as the slope of the dispersion, implying that the relatively sluggish optical modes should not contribute strongly to the thermal conductivity. Experimentally, optical modes have been shown to contribute much as 5% in bulk systems, confirming this intuition. The impact of scattering rate, however, is less intuitive. We can make the simplifying assumption of Mathiesson's rule, but the most dominant scattering mechanisms must be rigorously computed. I have provided the three most significant for the discussions of this work, but this is not nearly an exhaustive list:

$$\frac{1}{\tau_j} = \frac{1}{\tau_{pp,j}} + \frac{1}{\tau_{b,j}} + \frac{1}{\tau_{pi,j}} = AT\omega^2 e^{-C/T} + \frac{v_j}{d} + D\omega^4 \tag{2.19}$$

Where $\tau_{pp,j}$, $\tau_{b,j}$, and $\tau_{pi,j}$ are the scattering rates among three phonons, phonons and boundaries, and phonons and static impurities, respectively. A, C, and D, are material properties that define the intensity of the respective scattering events detailed in Ref. [45]. At the nanoscale, scattering at the boundary becomes dominant as mean free paths of carriers become limited.

Some notable temperature trends for the thermal properties discussed above are shown in figure 2.4.

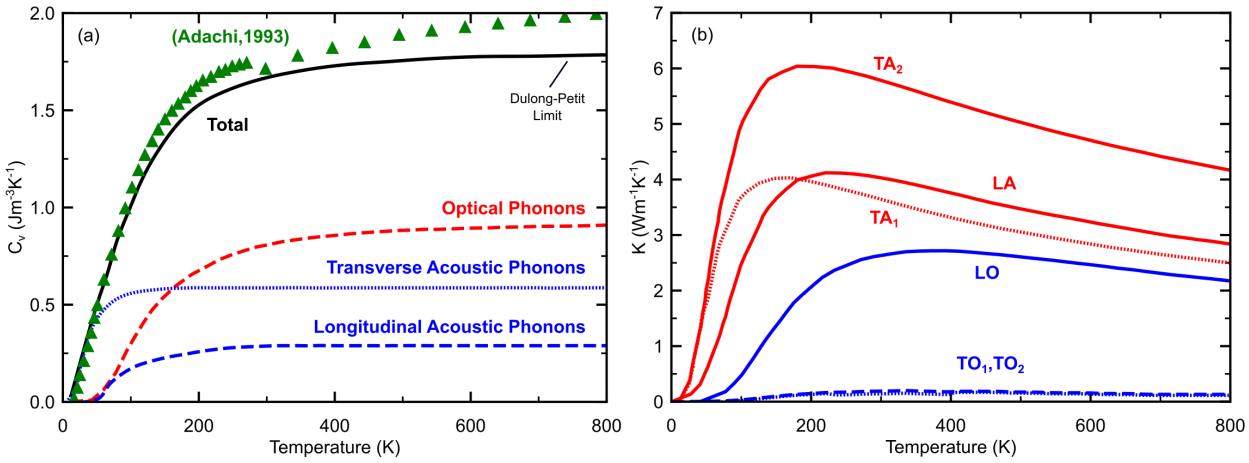

Figure 2.4: **The Temperature Dependence of the Phonon Contributions to Thermal Transport Properties**:(a) Estimated contributions to the volumetric heat capacity for each phonon branch, reproduced, from Ref. [7]. θ_D, the Debye temperature, defines the temperature beyond which all the phonon modes are active in the system. Thus, the constant region in C_v referred to as the Dulong-Petit limit. (b) Contributions of each phonon branch to thermal conductivity of a 20 nm Silicon nanowire reported in Ref. [46].

We can see that the optical phonon modes contribute significantly to the heat capacity even at relatively low temperatures, where not all phonon modes are represented in the structure. With their low group velocity, you can approximate them to be "standing" phonon waves in the medium, their localization means they contribute as a scattering mechanism for the higher velocity acoustic modes [47], locally storing and exchanging energy mediating transport. Counterintuitively, it has been shown that optical phonons can contribute up to 20% of thermal conductivity as the critical dimension of a system is reduced [46], highlighting the need to understand the transport mechanisms of the optical phonon modes in nanoscale systems.

2.1.2 Electrons

In electrically conducting systems, the principal energy carriers are electrons. In the presence of bonding and a periodic structure, electrons collect in bands and, based on the total number of electrons in the system as well as the binding strength of the bond, the electrons can exist in a band which is bound, below the Fermi energy, or free above the fermi energy. To describe the thermal motion of these particles, we have to begin with the quantum theory pioneered by Schrödinger [48] which describes their dispersions. A graphic describing this thermal motion is shown in Fig. 2.5

We begin with Scrodinger's Equation,

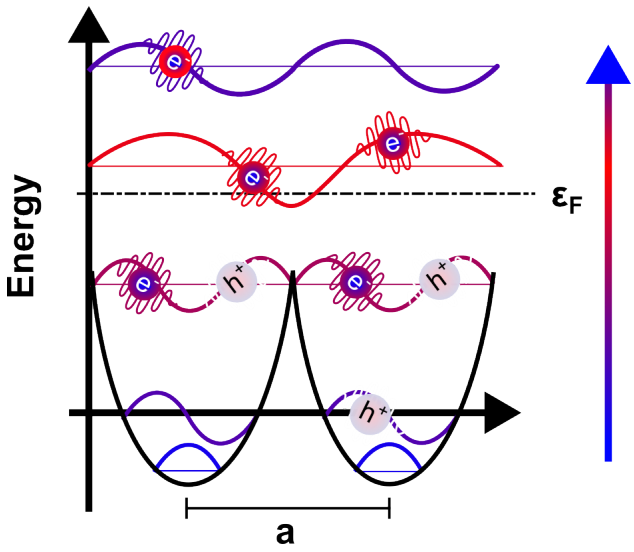

Figure 2.5: **Electron Propagation**: Heat is stored within the energy levels or bands of the system, thermal energy is transmitted through the smearing of the of electrons into higher energy bands. At bands higher than the Fermi energy, the electrons are "unbound" and may propagate freely across lattice sites, contributing to conduction. At temperatures above absolute zero, electrons populate higher bands opening holes below the Fermi energy, increasing total electron mobility. In metals, this Fermi energy intersects a band allowing for free electronic conduction of both electronic and thermal energy.

$$-\frac{\hbar^2}{2m_e}\frac{\partial^2\Psi}{\partial x^2} + V\Psi = i\hbar\frac{\partial\Psi}{\partial t} \tag{2.20}$$

where m_e is the mass of the electron, Ψ is the electron wave function which is a function of both space, x, and time t, and V is the potential that the electrons exist within. Only a fundamental understanding of this equation is required to describe the motion of electrons within solid media. Therefore, for more detailed of derivations of this equation, Ref. [49] can be used.

Electrons within crystals are subject to a periodic potential, $V_{lattice}$, or the interatomic potential. This potential is a functionalization of the electrostatic tension holding the lattice together, a simple periodic potential well is used in Fig. 2.5 for illustration but when solving for the band structure of real systems a more complex model can be used [50, 51]. These potentials are often simplified to be independent of time. We therefore can solve Eq. 2.20 with a separation of temporal and spatial variables, giving $\Psi(x,t) = \psi(x)\phi(t) = \psi\phi$, where for brevity the functional dependence of ψ, and ϕ are dropped. Then we have,

$$\left[-\frac{\hbar^2}{2m_e}\frac{\partial^2\psi}{\partial x^2}+V\psi\right]\frac{1}{\psi}=i\hbar\frac{\partial\phi}{\partial t}\frac{1}{\phi}=E \tag{2.21}$$

where E is an eigenvalue solution to Eq. 2.21. The LHS of Eq. 2.21 can be solved easily giving,

$$\phi\propto e^{\frac{-iEt}{\hbar}}E \tag{2.22}$$

This is simply a plane wave in time with a frequency of $\omega=\frac{E}{\hbar}\Rightarrow E=\hbar\omega$, thus, the eigenvalue E is precisely the energy states of the electron. Now analyzing the spatial component of Eq. 2.21,

$$-\frac{\hbar^2}{2m_e}\frac{\partial^2\psi}{\partial x^2}+(V-E)\psi=0 \tag{2.23}$$

This equation contains all the information on the electronic states E subject to a periodic crystal.

On the structure of the model presented below, we will make an effective, albeit extreme, simplification to the complex interatomic potentials present in real 3D crystals. This simplified system called, the Kronig-Penny model, assumes a repeating finite square potential well, separated by the interatomic spacing a. We can define it mathematically as a piecewise function,

$$V=\begin{cases}0 & \text{for} \quad 0<x\leq b\\ V_0 & \text{for} \quad -c\leq x\leq 0\end{cases} \tag{2.24}$$

we subject these wells to the periodicity of the lattice, such that $V(x+b+c)=V(x)$, and where $a=b+c$, then using exponential solutions to Eq. 2.23, we retrieve,

$$\Psi=\begin{cases}Ae^{iMx}+Be^{-iMx} & \text{for} \quad 0<x\leq b\\ Ce^{iLx}+De^{-iLx} & \text{for} \quad -c\leq x\leq 0\end{cases} \tag{2.25}$$

where A,B,C,D can be found from applying the boundary conditions and,

$$E=\frac{\hbar^2M^2}{2m} \tag{2.26a}$$

$$V_0-E=\frac{\hbar^2L^2}{2m} \tag{2.26b}$$

M, and L are the eigenstates of the electron in question. The characteristics at the boundaries will not be fully computed here, however the most crucial to develop the thermal statistics in real crystals is the periodic boundary, in other words an application of Bloch's Theorem [52],

$$\psi(x+(b+c)) = \psi(x)e^{-x(b+c)} = \psi(x)e^{ika} \tag{2.27}$$

where k is the wavevector. Then, by application of this boundary condition and others can be found explicitly solved in [7], we achieve our goal being the dispersion relation between energy, E and k indirectly via the relation between M and k, recognizing the relationship between M and E. rearranging Eq. 2.26a into $M = \sqrt{\frac{2mE}{\hbar^2}}$. The dispersion relation we retrieve is,

$$\frac{M^2 - L^2}{2ML}\sinh(Lc)\sin(Mb) + \cosh(Lc)\cos(Mb) = cos[k(b+c)] \tag{2.28}$$

where $\sinh(x)$ and $\cosh(x)$ are the hyperbolic trig functions. Now for any wavevector, k, the only unknown in Eq. 2.28, is E which is embedded in both, M and L. To simplify, let us imagine where $c \to 0$ and $V_0 \to \infty$, while maintaining $L^2cb/2$ being equal to some constant P. We see under these conditions that $\sinh(Lc) \approx Lc$, and $\cosh(Lc) \approx 1$ Eq. 2.28 reduces to,

$$\frac{P}{2Mb}\sin(Mb) + \cos(Mb) = cos[kb] \tag{2.29}$$

The RHS of Eq. 2.29 restricts the solutions of this dispersion relation to the range of [-1,1]. The LHS of this equation exists beyond this range, however, under the Kronig-Penny model, these solutions are forbidden, indicating the existence of what we now call "band gaps" between allowed electronic states within certain interatomic potentials. We also observe a similar periodicity about $\pm\pi/(b+c) = \pm\pi/a$, which is exactly the Brillouin Zone discussed in the prior section. The final simplification we will make is that of the free electron, the states in which the electrons do not "feel" the interatomic potential which other lower energy electrons are bound by. This type of system emerges in conducting media, so is pertinent to our discussion on metals. We thus apply the condition that $L = M$[¶], and as such P=0, our dispersion Eq. 2.29,

[¶]equivalent by Eq. 2.24 where $V_0 = 0$

$$\cos(Mb) = cos[kb] \tag{2.30}$$

and we therefore, by inspection, retrieve the free electron dispersion relation,

$$E = \frac{\hbar^2 k^2}{2m} \tag{2.31}$$

A less circuitous route to achieve this relation is to solve Eq. 2.20 under the condition $V = 0$, an electron under no potential, this derivation is discussed further in [49]. An example of both the *realistic* Kronig-Penny model, and the more *idealistic* free electron model is provided in 2.6.

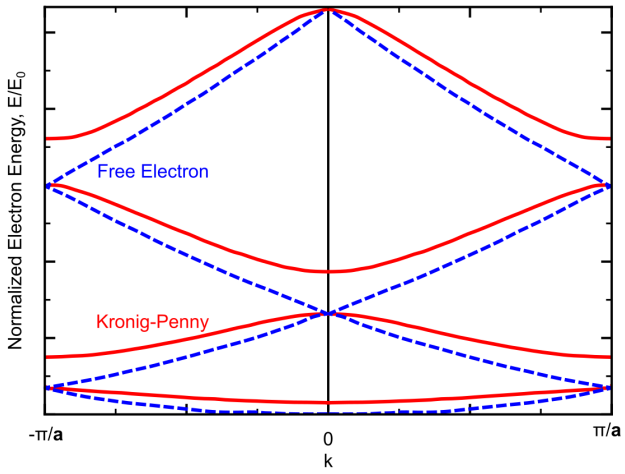

Figure 2.6: **Electron band structure**: The folded zone representation of the electron band structure or energy dispersion, showing both the Kronig-Penny model and the Free electron model.

Interestingly for electrons, they do not obey the same filling rules as phonons, and for that matter, bosons in general. This is due to the spin characteristics of these particles, which we will not discuss in detail, but can be found in Ref. [49]. These rules dictate that the energy levels of electrons must be filled from the lowest energy to the highest energy, and by Pauli exclusion [53], only two electrons may occupy the same state. This is opposed to phonons, and other bosons, which may have an infinite number of particles at a given state. For each medium, we follow this filling procedure for each state and band until no other electrons remain for a given element. We define this final energy level at absolute zero, the Fermi-Energy (ϵ_F), and particles that obey this filling procedure Fermions based on the foundational theory of Fermi [54] and Dirac [55] in the 1920's.

This leads us to the definition of a semiconductor, that being some medium where the uppermost electronic state lies within a forbidden region of the dispersion. This is contrasted by the Fermi energy laying at the center of a band, as in the case with metals. Any Fermion, in either of these two cases, obeys a statistical distribution referred to as the Fermi-Dirac distribution,

$$f_{FD} = \frac{1}{e^{\frac{(\epsilon-\epsilon_F)}{k_b T}} + 1} \tag{2.32}$$

We may now begin to interrogate the thermal statistics governing electronic heat flow. On this point, for the sake of brevity, we will only follow the derivation for the case of the free electron. The density of electronic states, given the free electron dispersion

$$\mathcal{D}_e = \frac{1}{V}\frac{dN}{dE} = \frac{1}{2\pi^2}\left(\frac{2m_e^*}{\hbar^2}\right)^{3/2}(E-\epsilon_F)^{1/2} \tag{2.33}$$

A depiction of such a density of states is given in Figure 2.7, after applying the Fermi-Dirac distribution and several temperatures.

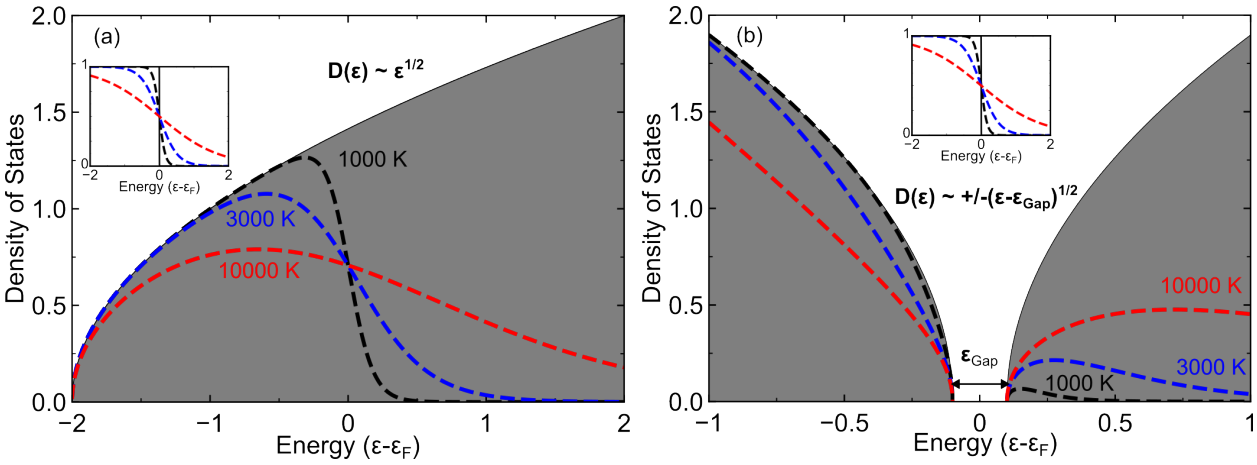

Figure 2.7: **Electron Occupied Density of States**: The density of occupied electronic states at several temperatures of (a) A free electron metal where the Fermi energy lies in the middle of a parabolic band, and (b) A semiconductor with a band gap of ϵ_{Gap}. The insets in each depicting the Fermi-Dirac distribution at the given temperatures.

Note the given temperatures are much higher than the temperatures simulated in the previous subsection due to the higher energies within electronic systems. There is also an example of a semiconducting system with a small band gap of 0.2 band gap and a Fermi energy lying precisely in the center of the two bands.

By these definitions, we then arrive at the electronic specific heat we must make the simplifying assumption that the thermal changes in density of states occur near the Fermi energy, and as the Fermi energy is also much larger than the thermal energy present in the system at room temperature, that we can simply use the density of states at the Fermi energy$\mathcal{D}(\epsilon_F)$ as a substitute for $\mathcal{D}(\epsilon)$. We can plug in Eqs., 2.33, and 2.32 into the form of Eq. 2.4 for the heat capacity of electrons,

$$C_{v,e} = \mathcal{D}_e(\epsilon_F) \int_0^\infty \frac{(E-\epsilon_F)^2}{k_b T^2} \frac{e^{\frac{(E-\epsilon_F)}{k_b T}}}{\left(e^{\frac{(E-\epsilon_F)}{k_b T}} - 1\right)^2} \tag{2.34}$$

and similarly we can retrieve the thermal conductivity as,

$$\kappa_e = \frac{1}{3} v_F^2 \tau_e \mathcal{D}_e(\epsilon_F) \int_0^\infty \frac{(E-\epsilon_F)^2}{k_b T^2} \frac{e^{\frac{(E-\epsilon_F)}{k_b T}}}{\left(e^{\frac{(E-\epsilon_F)}{k_b T}} - 1\right)^2} \tag{2.35}$$

where v_F is the slope of the electronic dispersion at the Fermi energy, the so-called Fermi velocity, which describes the speed at which electrons at the Fermi energy propagate. τ_e is the scattering rate of the electrons, which needs to be computed via Boltzmann transport theory [56] but can be more simply decomposed by Mathiesson's rule as,

$$\frac{1}{\tau_e} = \frac{1}{\tau_{ee}} + \frac{1}{\tau_{ep}} + \frac{1}{\tau_{eb}} = A_{ee} T_e^2 + B_{ep} T_p + \frac{v_F}{d} \tag{2.36}$$

Whereτ_{ee}, τ_{ep}, and τ_b are the scattering rates between, an electron and, the other electrons on the Fermi surface, the phononic subsystem, and boundaries respectively. A_{ee}, and B_{ep} are related to the collisional frequencies intrinsic to the electrons, and between the electrons and the phonons which can be computed from the theories of Fermi liquid Theory [57] and the Cerenkov radiation of sound waves [58], each of which is detailed in the below investigations.

2.2 Radiation

Now that we have established the thermal statistics governing conduction, we must discuss the same for the most prevalent form of heat transport, by definition the fastest carriers, which is

radiation. Any time a charged particle moves the resultant undulation in electric field emits light. We intuitively understand this emission as the "glow" of hot steel as it exits a forge. However, this emitted energy happens at all temperatures and circumstances as it is merely a consequence of thermal motion, a universal default ensuring the second law of thermodynamics[‖].

The electromagnetic laws governing light and therefore radiant heat are known as Maxwell's Equations, which, under the assumption of a non-magnetic material, are [59],

$$\nabla \times \mathbf{E}(\mathbf{r},\omega) = \mathbf{i}\omega\mu_{\mathbf{0}}\mathbf{H}(\mathbf{r},\omega) \tag{2.37}$$

$$\nabla \times \mathbf{H}(\mathbf{r},\omega) = -i\omega\varepsilon(\omega)\mathbf{E}(\mathbf{r},\omega) + \mathbf{J}(\mathbf{r},\omega) \tag{2.38}$$

$$\nabla \cdot \mathbf{E}(\mathbf{r},\omega) = 0 \tag{2.39}$$

$$\nabla \cdot \mathbf{H}(\mathbf{r},\omega) = 0 \tag{2.40}$$

where E, H, and J are the electric, magnetizing, and current fields, respectively. $\mathbf{r}$ is the spherical spatial variable,μ_0 is the magnetic permeability of the vacuum, and $\varepsilon(\omega)$ is the electric permittivity of the media in which the light is present in, for the vacuum $\varepsilon(\omega) = \varepsilon_0$. Hidden inside the equations specifically when assessing a region of vacuum with no charge or currents, taking the curl ($\nabla\times$) of Eqs. 2.37, and 2.38, we get,

$$\mu_0\varepsilon_0\frac{\partial^2\mathbf{E}}{\partial t^2} + \nabla^2\mathbf{E} = 0 \tag{2.41}$$

and,

$$\mu_0\varepsilon_0\frac{\partial^2\mathbf{H}}{\partial t^2} + \nabla^2\mathbf{H} = 0 \tag{2.42}$$

These equations describe a wave with a speed, $v_{wave} = \sqrt{\mu_0\varepsilon_0} = c_0$ where c_0 is the speed of light. Maxwell did not immediately draw this conclusion in his earliest works, but recognizing this as a constant among all light, implies that the dispersion relation must be simply,

[‖] The second law of thermodynamics is, as stated by Clausius, $dS \leq 0$ or, more colloquially, heat seeks equilibrium. Implying that the temperature of an object held in a perfect vacuum chamber at a lower temperature must lose energy in some way to equilibrate to the walls of the chamber. Electromagnetic radiation is the only thermodynamic process capable of achieving this in this instance.

$$k = \frac{\omega}{c_0} \tag{2.43}$$

Furthermore, the distribution of photonic states, avoiding the pitfalls of an *ultraviolet catastrophe*** was first described by Planck [40] understanding the fundamental quantum nature of light. Planck wrote that the maximum spectral energy density per wavelength of light $\lambda = \omega/2\pi c_0$ emitted from a radiating body is,

$$u_\lambda(\lambda, T) = \frac{8\pi h c_0}{\lambda^5} \frac{1}{e^{\frac{hc}{\lambda k_b T}} - 1} \tag{2.44}$$

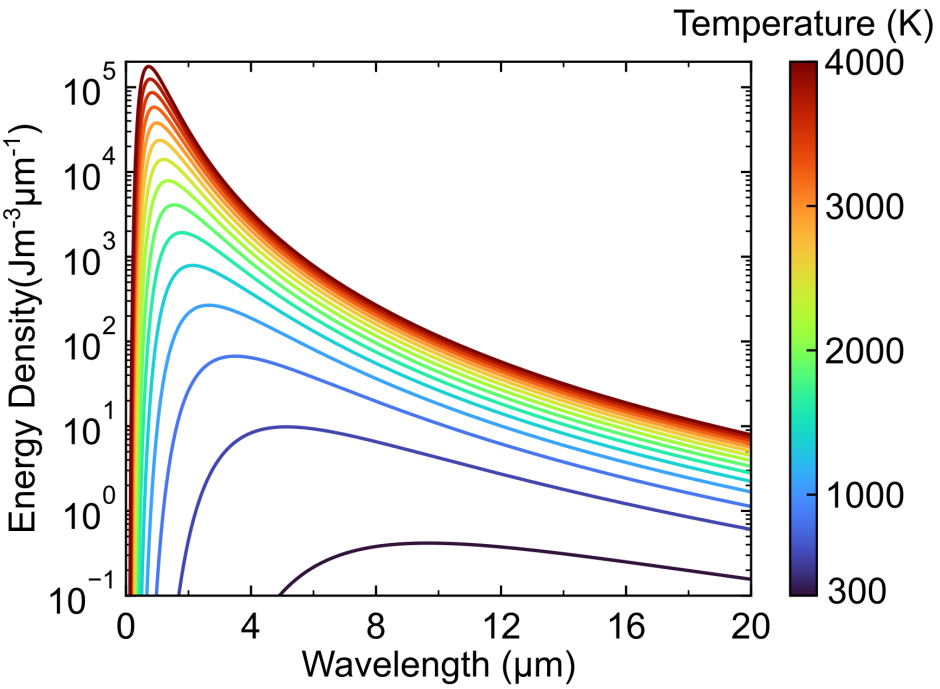

Figure 2.8: **Spectral Energy Density of a Blackbody**: The spectral energy density of photonic states plotted versus wavelength in microns at several temperatures given in the colorbar.

Figure 2.8 depicts the spectral energy density emitted from a perfectly black emitter. Finally, by integrating Eq. 2.44 across all wavelengths, we obtain the total emissive power of a perfect emitter,

**The discrepancy between measurements of radiant heat and theoretical formulations based around classical statistical mechanics.

$$q_{total} = \int_0^\infty u_\lambda(\lambda, T) d\lambda = \sigma T^4 \tag{2.45}$$

and thus we have, The Stefan-Boltzmann law. This emissivity term is key to understanding the realistic emitted power from a body. By Kirchhoff's law [60] the spectral distribution of the emitted radiation is exactly the absorbance of the system, which can be calculated from the dielectric function as one minus the reflectivity (1-R) assuming an opaque material at normal incidence. Therefore, to fully understand the emitted spectra of a body we must assess the absorption and transmission of a body, given by the relative permittivity of a medium $\varepsilon_r(\omega)$ in Eq. 2.42 or, the dielectric function.

2.2.1 Dielectric function

In real systems, the intrinsic electric and magnetic structures of a medium distort and restrict the range of possible electromagnetic states. We quantify this effect as the dielectric function ε in order to describe the response of a medium to an incident electromagnetic field. We intuitively understand that light, when interacting with a non-scattering non-magnetic medium, can behave in three ways, reflection, R, absorption, A, and Transmission, T.

To compute the coefficients of each of these modalities, we will begin with factorizing the generally complex $\varepsilon(\omega)$ into the optical constants, n and k,

$$\varepsilon(\omega) = \varepsilon'(\omega) + i\varepsilon''(\omega) = (n^2 - k^2) + 2ikn \tag{2.46}$$

where $\varepsilon'(\omega)$ describes the changes in phase experienced by incident light, and $\varepsilon''(\omega)$ represents the energy lost as light propagates through the medium. In this form n refers to the index of refraction, which is the ratio of the speed of light in the medium, and k is the extinction coefficient, detailing the absorption of the medium. From these constants, angle of incidence and polarization, the percentage of light that is absorbed, reflected to transmitted can be calculated via the Fresnel coefficients with details outlined in Ref. [61].

Importantly for our discussion, ε is a function of the internal fields of a system; therefore, it depends on the electronic band structure, as well as dipole vibrations, such as optical phonon branches. As the speed of light c_0 produces a dispersion of light with such an intense slope on

the scales of the electron and phonon dispersion can be treated as the vertical axis. Thus, due to conservation of momentum, when looking for modes which directly interact with light, they must exist in the dispersion intersecting the vertical axis. In other words, based on its dispersion light can interact directly with, optical phonons, electronic transitions from sub-band to the Fermi surface[††], or the direct oscillation of free charges at the Fermi energy for metals. Each of these modes is classically treated as a Dirac-delta function at the frequency of the resonance, as in the Einstein model, however, due to scattering in real systems, these modes are spectrally broader than such an approximation. We will therefore make a similar generalization as we did when we plotted Einstein's model for density of states, by substituting the Dirac-delta for a Lorentzian [43]. This leads us to the simple formulation of the dielectric function as the sum of Lorentzians, however, as we will focus on the interactions of metals and dielectrics for this work, we will have different treatments for each.

For metals, we will assume pure elemental metals, and therefore we will assume a monoatomic basis with no contribution from the lattice to the dielectric function. We then would only have the contributions of free electron oscillations described by Drude theory [62], and the inter-band transitions [63]

$$\varepsilon_m(\omega) = 1 - \frac{f_p\omega_p^2}{\omega^2 - i\omega\Gamma_p} + \sum_j \frac{f_j\omega_p^2}{\omega_j^2 - \omega - i\omega\Gamma_j} \tag{2.47}$$

with,ω_j, f_j, and Γ_j describes the wavelength, strength, and dampening of the j^{th} inter-band transition oscillations. ω_p, f_p, and Γ_p are the wavelength, strength, and dampening of the free carrier oscillation. It is important to note that the dampening of each oscillation is exactly the τ^{-1} computed in the prior section associated with the thermal statistics of the mode, with the free carrier dampening representing the total scattering rate of a conducting electron described in Eq. 2.36, and the inter-band transition dampening term specifying the electron-electron collision rate between the sub band being promoted and the conduction band.

Dielectrics are far simpler when calculating the dielectric function we need only consider the optical phonon branches, and the behavior of the medium at high frequencies ε_∞ giving,

[††]The Fermi surface is a generalization of the Fermi level in three-dimensional k space

$$\varepsilon_d(\omega) = \varepsilon_\infty + \sum_j \frac{f_j}{\omega_j^2 - \omega - i\omega\Gamma_j} \tag{2.48}$$

where the terms ω_j, f_j, and Γ_j, refer again to the wavelength, strength, and dampening of the j^{th} optical phonon. Γ_j is also again correlated with the phonon scattering term calculated for the thermal conductivity prediction.

Thus far, we have computed the general forms for dielectric function used throughout this thesis, however, we have only considered the reaction of a medium to incident light. To thoroughly understand the nature of radiation, we must identify how light propagates from hot internal vibrations, and into vacuum. This can be done with the Maxwell's equations as listed above, however, we must consider the interaction between light and internal currents associated with the carrier oscillations, the coupled modes that emerge are called polaritons.

Polaritons: Coupled Modes

Fundamentally, polaritons are the electromagnetic modes of solid state media: light trapped by matter that arise when electromagnetic fluctuations propagate through solids and resonate with internal degrees of freedom. For example, polar insulators exhibit the optical phonon modes which are so called infrared active, that is, they contain within their dispersion wave vectors that infrared light can also propagate in free space. These electromagnetic waves can then couple to dipole vibrations within the lattice, which leads to the propagation and creation of polaritons. These oscillations fall purely out of Maxwell's equations where both waves cannot be solved alone and must be solved together, i.e., they are coupled.

Polaritons exist in many varietals, including the ones described above and shown in the dispersion in Fig. 2.9: Phonon-polaritons (PhPs) which are light coupled with lattice oscillations or plasmon-polaritons (PlPs), and many more corresponding to several quasi-particles and their coupled light mode. Regardless of the sort, polaritons exist mainly in two flavors with respect to dispersion of light: evanescent or propagating. That is, either the polariton has a correct momentum such that it can freely propagate in the bulk of the material, whether that be with photon-like or phonon-like propagation. Evanescent polaritons are heavily spatially confined and thus can only propagate at specified directions or momenta, and are exponentially decaying elsewhere. When

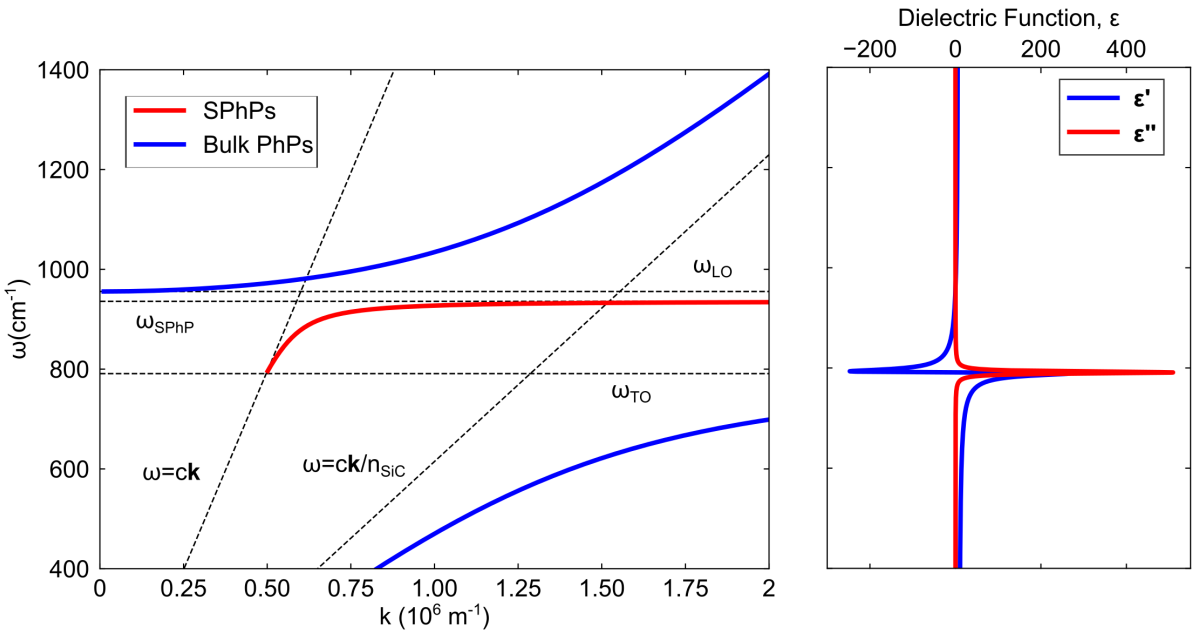

Figure 2.9: **Schematic dispersion space of phonon polaritons in SiC** [64]: There is an anti-crossing condition associated with the free space light line ($\omega = c\mathbf{k}$) and the transverse optical phonon ($\omega_{TO} = 794$ cm^{-1}) which gives rise to two branches of phonon polaritons, Bulk, and surface modes. The plot on the right is the corresponding real and imaginary components of the dielectric function (ε') for SiC, highlighting the significant features that give rise to polariton modes

discussing the surface confined modes, I will use the prefix S- for specificity. There also exists polaritonic modes that can both propagate volumetrically but have similar spacial confinement to the surface modes called hyperbolic H-; these hyperbolic modes are evanescently confined to specific momenta such that an iso-frequency surface of a hyperbolic mode resembles a hyperbola when plotted with respect k_x and k_y . With the definitions aside, we can examine the impact of these modes at large, and specifically through a thermal transport lens.

2.2.2 The Near-Field

In the entirety of this section, we have been implicitly assuming that the emitted energy can propagate in the surrounding medium, which is not a complete description of radiation. For example, we would not expect that a black body system embedded in a material of perfect reflectance to ever lose any energy. We have then stumbled upon the idea that there can be modes of light that should contribute to thermal emission but do not because they are disallowed by an interface on the basis of dielectric mismatch or reflection. The converse of this argument can also be ex-

tended to a material/vacuum interface. There exists some modes of radiant heat that are hindered at the material-vacuum interface which remain within the medium referred to as "frustrated" In general, these disallowed modes are classified as "evanescent" as they exponentially decay away from the interface shown in Fig. 2.10. They extend a distance away from the surface proportional to wavelength, within this distance, neighboring bodies can absorb these high wave-vectors. For this reason, the idea of a classical "black body" breaks down, and the available radiation does not follow the expected spectral distribution. This region is referred to as the near-field. This is best illustrated by the plots of Fig. 2.10 where we see that the spectral energy density radiating from a SiC surface can be dramatically enhanced as the distance to the surface, d, reduces to the near field.

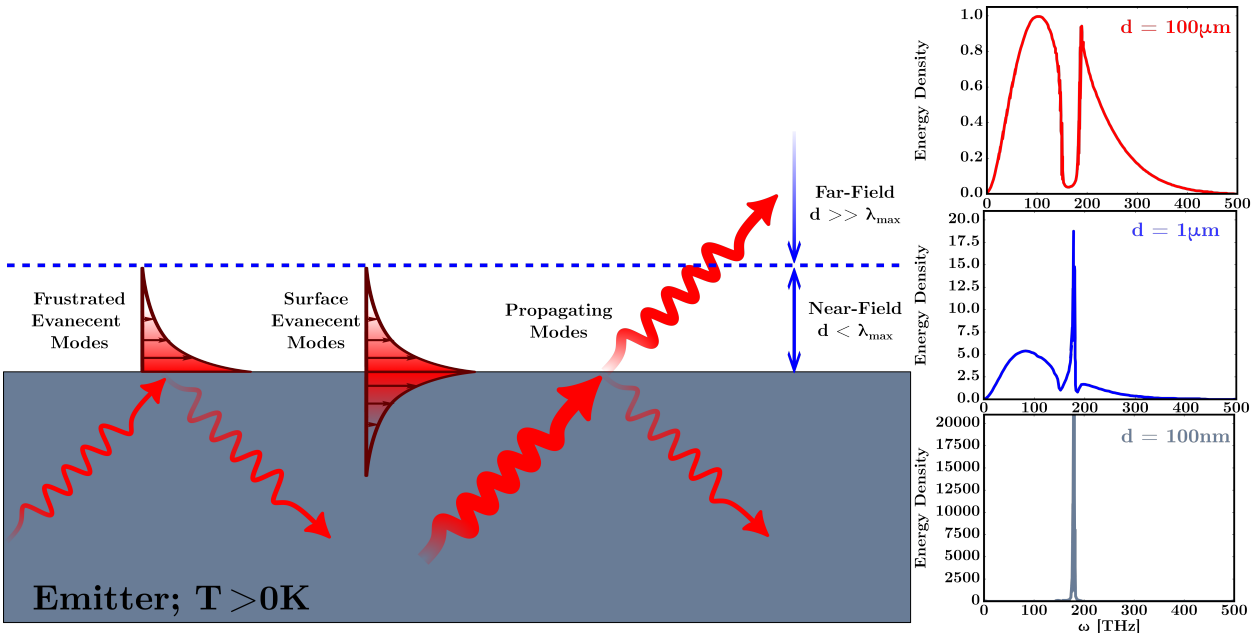

Figure 2.10: **Graphic showing the different mechanisms of thermal radiation**. Evanescent modes will only extend exponentially into the near field but, they do not have correct momentum to propagate into the far field. The three plots from top to bottom represent the emitted spectral distribution observed at a distance d above the surface of SiC [65]. The far field ($d = 100\mu$m) is limited to an emissivity of 1 and the flux is similarly limited, however as you move to the near field the spectrum of emitted radiation becomes both spectrally local and, as it has no upper-bound on intensity, going well beyond the black body limit.

There has been considerable work to decipher and model radiation in the near field [65, 66]. We begin by obtaining the oscillating electric and magnetic fields using dyadic Green's functions $\mathbf{G}^H$, and $\mathbf{G}^E$ with a thermally stochastic current field at a given position $\mathbf{r}$ $\mathbf{J}^T(\mathbf{r}', \omega)$ [67]:

$$\mathbf{E}(\mathbf{r},\omega) = i\omega\mu_0 \int_V \mathbf{G}^E(\mathbf{r},\mathbf{r}',\omega)\cdot\mathbf{J}^T(\mathbf{r}',\omega)dV \tag{2.49a}$$

$$\mathbf{H}(\mathbf{r},\omega) = \int_V \mathbf{G}^H(\mathbf{r},\mathbf{r}',\omega)\cdot\mathbf{J}^T(\mathbf{r}',\omega)dV \tag{2.49b}$$

where V is the volume of the sample, and the current fluctuations are given by the fluctuation dissipation theorem [66, 68].

$$\Big\langle \mathbf{J}^T(\mathbf{r}',\omega)\otimes\mathbf{J}^{T*}(\mathbf{r}'',\omega)\Big\rangle = \frac{4}{\pi}\omega\varepsilon_0\mathrm{Im}[\varepsilon(\omega)]\Theta(\omega,T)\delta(\mathbf{r}'-\mathbf{r}'')\delta(\omega-\omega') \tag{2.50}$$

Where, the delta functions account for the locality of the dielectric constant, and $\Theta(\omega,T)$ is the mean energy of an electromagnetic state [65],

$$\Theta(\omega,T) = \frac{\hbar\omega}{e^{\frac{\hbar\omega}{k_bT}}-1} \tag{2.51}$$

The energy flux thermally emitted in the near field is then given by the time averaged Poynting vector S,

$$\Big\langle S(\mathbf{r},\omega)\Big\rangle = \frac{1}{2}\mathrm{Re}\left[\Big\langle \mathbf{E}(\mathbf{r},\omega)\times\mathbf{H}^*(\mathbf{r},\omega)\Big\rangle\right] = q^{prop}(\omega)+q^{evan}(\omega) \tag{2.52}$$

where $*$ refers to the Hermitian conjugate. $q^{prop}(\omega)$ and $q^{evan}(\omega)$ represent the propagating and evanescent contributions of the flux given by,

$$q^{prop}(\omega) = \frac{\Theta(\omega,T)}{\pi^2}\sum_{q=s,p}\int_0^{k_0} k\left[\frac{(1-|r_E^q|^2)(1-|r_R^q|^2)}{|1-r_E^q r_R^q e^{2ik_{z,0}d}|^2}\right]dk \tag{2.53}$$

and,

$$q^{evan}(\omega) = \frac{\Theta(\omega,T)}{\pi^2}\sum_{q=s,p}\int_{k_0}^{\infty} ke^{-2ik_{z,0}d}\left[\frac{\mathrm{Im}(r_E^q)\mathrm{Im}(r_R^q)}{|1-r_E^q r_R^q e^{2ik_{z,0}d}|^2}\right]dk \tag{2.54}$$

where $r_{E,R}$ are the Fresnel coefficients between the vacuum and the emitter, receiver respectively. $k_{z,0}$ is the z component of the vacuum wavevector, k_0, and q refers to the polarization of light [68]. For the propagating case, this solution reduces to the flux predicted by Planck's law, where emissivity is equal to 1-R. The evanescent case we see two features to note: one this flux is exponentially

decreasing as we separate the emitter and receiver implying the intensity we can expect in contact to greatly exceed the classical black body, and secondly the flux depends primarily on the imaginary component of the dielectric function. This dependence on the dielectric function is precisely the root of the intense radiation in the near field shown in Fig. 2.10 around the TO mode of SiC. [64]

2.3 Transport across interfaces

From the above discussion on intrinsic thermal transport, we can see that as critical dimensions of electronic devices reduce, the most significant contribution to scattering and, therefore, thermal resistance is the interface by limiting the mean free path of thermal carriers. There is also a competing effect to this, which is defined by the ability of an interface itself to transfer energy. This interfacial conductance, h, was first defined by Kapitza, when interrogating the temperature difference between liquid helium and the walls of a pipe:

$$h = \frac{Q}{\Delta T} \tag{2.55}$$

Where, Q is the heat flux applied to the interface and ΔT is the change in temperature across the interface. There are many models that compute the thermal transport across interfaces, they vary based on the character of the scattering event experienced by the thermal carrier at the interface. [69]. The standard assumption is that carriers scatter elastically, with the interface, as an example, for phonons this implies that a phonon of frequency ω_1 will emit a phonon of ω_1 across the interface. This equal energy exchange will be assumed for this section but, it has been shown to lack nuance when considering real-world systems due to the emergence of interfacial modes [70], or large subsystem nonequilibrium [71]. As the focus of this dissertation is the interfacial transport at the interfaces of the electron dominant metals and phonon dominated dielectrics, I provide two models to describe energy transfer at the interface between the phonons within the metal and phonons of a substrate, and electrons of a metal to phonons of a dielectric substrate.

To formulate the heat flux Q in Eq. 2.55 in the case of phonon transport, we can use the equation of phonon radiative transfer (EPRT) [10]:

$$q = \sum_j \int_{\Omega=4\pi} \int_0^{\omega_{max,j}} cos(\theta_i) I_j(z,t,\omega,v,\Omega) d\omega d\Omega = h_{bd}\Delta T \tag{2.56}$$

where θ_i is the angle of incidence for the phonon relative to the interface normal, Ω is the solid angle relative to the same normal. The differential solid angle is simply $d\Omega = d\varphi \sin(\theta_i) d\theta$ under spherical coordinates. I is the directional spectral intensity of phonons per unit area, and as with the phonon formalism above, each phonon branch, j, is calculated and summed separately. I can be calculated as,

$$I_j = \frac{1}{4\pi} v_j f_{BE} \hbar\omega \mathcal{D}_j \tag{2.57}$$

the factor of $(4\pi)^{-1}$ accounts for the intensity per solid angle,Ω. Which finally gives a general form of the heat flux at the interface under the EPRT,

$$h_{bd}^{i\to 3-i} = \frac{1}{2} \sum_j v_{i,j} \int_0^{\frac{\pi}{2}} \int_0^{\omega_{i,j}^{max}} \hbar\omega \mathcal{D}_{i,j} \zeta_j^{i\to 3-i}(\omega) \frac{\partial}{\partial T^*} [f_j] \cos(\theta_i) \sin(\theta_i) d\omega d\theta \tag{2.58}$$

where i here refers to the phonons in the medium before the interface and $3-i$ refers to the medium beyond the interface. T^*, is an effective temperature if the distribution of f is not sufficiently thermalized. $\zeta_j^{i\to 3-i}(\omega)$ refers to the transmission probability of a flux of mode j from side i to side $3-i$. We will use this form in our further derivations for interfacial thermal transport in this section.

In the special case of phonons of a *metal* which impinge on an interface with a *dielectric*, we cannot expect the low frequency thermal modes in the metal to spectrally match the higher frequency modes in the dielectric. Therefore, to estimate the phonon-phonon interface conductance, we must understand the vibrational mismatch at the interface, to account for this, Swartz and Pohl used the EPRT to develop the diffuse mismatch model (DMM) at a realistic interface. [69].

Applying DMM, we assume the phonons to "forget" their incident polarization at the interface, i.e., diffuse scattering. For an isotropic Debye solid, the most simplified form of DMM is,

$$h_{bd}^{DMM} = \frac{1}{8\pi^2} \sum_j \frac{1}{v_{i,j}^2} \int_0^{\omega_{max,j}^i} \zeta^{i\to 3-i}(\omega) \frac{\partial}{\partial T} \left[\frac{\hbar\omega^3}{e^{\frac{\hbar\omega}{k_b T}} - 1} \right] \tag{2.59}$$

Everything else is known in this formulation except for the transmission coefficient, $\zeta^{i\to 3-i}$, which is the heart of the calculation. According to the principle of detailed balance [72] and elastic scattering, the phonon flux with energy $\hbar\omega$ originating on side i must be equal to the flux on the 3-i side. Thus,

$$\sum_j \frac{1}{v_{i,j}^2} f_{BE}\,\omega^2 \zeta_j^{i\to 3-i} = \sum_j \frac{1}{v_{i-3,j}^2} f_{BE}\,\omega^2 \zeta_j^{3-i\to i} \tag{2.60}$$

as described above, by the definition of diffuse scattering $\zeta^{i\to 3-i} = 1 - \zeta^{3-i\to i}$. We can therefore re-arrange Eq. 2.60 to solve for the transmission coefficient:

$$\zeta^{i\to 3-i} = \frac{\sum_j \frac{1}{v_{i-3,j}^2} f_{BE}\,\omega^2}{\sum_j \frac{1}{v_{i,j}^2} f_{BE}\,\omega^2 + \sum_j \frac{1}{v_{i-3,j}^2} f_{BE}\,\omega^2} \tag{2.61}$$

This can be simplified further by noticing that for elastic scattering, no phonons at frequencies above the lowest ω_{max}, between side i and 3-i can participate in energy transport, and therefore,

$$\zeta^{i\to 3-i} = \frac{\sum_j \frac{1}{v_{i-3,j}^2}}{\sum_j \frac{1}{v_{i,j}^2} + \sum_j \frac{1}{v_{i-3,j}^2}} \tag{2.62}$$

with the simplifying assumptions made, we have a frequency independent expression for the transmission coefficient.

The form presented here can even be further extended to an upper limit, where the transmission coefficient for all modes is set to 1, Swartz and Pohl call this upper bound to interfacial transport, the phonon radiation limit, a model of the total phonon flux that can possibly be "pushed" through an interface.

$$h_{bd}^{PRL} = \frac{1}{8\pi^2} \sum_j \frac{1}{v_{i-3,j}^2} \int_0^{\omega_{i,j}^{max}} \frac{\partial}{\partial T} \left[\frac{\hbar\omega^3}{e^{\frac{\hbar\omega}{k_b T}} - 1} \right] \tag{2.63}$$

When in equilibrium conditions, conduction across the interface is dominated by the scattering and transmission of phonons across an interface. However, under the conditions present within microelectronics, and laser irradiation, the electronic subsystem can be skewed and thrown into nonequilibrium with respect to the lattice, in this state the Fermi surface, widens massively, see Fig. 2.7. This results in many more electronic states available to scatter into for both the electrons

and phonons, thereby increasing the transmission of energy across the interface. To simulate the effect of this we can make a similar approximation to the EPRT but instead of the phonon modes incident to the interface we consider the electronic carriers incident to the interface. We then approach Eq. 2.58 under the assumption that the i modes follow the electronic thermal statistics. In turn, the electron-substrate boundary conductance h_{es} becomes [73],

$$h_{es}^{e\to p} = \frac{1}{4}\int_{\epsilon} v_F(\epsilon-\epsilon_F)\mathcal{D}_e\zeta^{e\to p}(\epsilon)\frac{\partial}{\partial T^*}\left[f_e\right]d\epsilon \tag{2.64}$$

where $\zeta^{e\to p}(\epsilon)$ is the transmission coefficient between the electronic energy in the metal to the phononic structure within the dielectric, and ϵ_F, and v_F are the Fermi velocity and Fermi energy respectively. Conveniently, this process is similar to the mechanism of electron-phonon equilibration described briefly above, in which a hot electron may relax within a single media via the emission of a phonon. During this process, the transition probability can be estimated from as a three-level system, $E_1 = \epsilon_F - \hbar\omega$, $E_2 = \epsilon_F$, and $E_3 = \epsilon_F + \hbar\omega$, and thus, $\zeta^{e\to p}(\epsilon) = \mathcal{J}_{\epsilon_F+\hbar\omega\to\epsilon_F} + \mathcal{J}_{\epsilon_F-\hbar\omega\to\epsilon_F} + \mathcal{J}_{\epsilon_F\to\epsilon_F+\hbar\omega} + \mathcal{J}_{\epsilon_F-\epsilon_F\to\hbar\omega}$. Due to the scale of the energies between the electrons and phonons, the phonons above and below the electronic transition $\pm\hbar\omega$, are extremely close to the Fermi energy. By Pauli exclusion we know that these transitions must occur extremely close to the Fermi surface, therefore using the thermal statistics developed above, the transition probability of emitting or absorbing a phonon in this system $\mathcal{J}_{\epsilon_F\pm\epsilon_F\to\hbar\omega}$ is,

$$\mathcal{J}_A = \mathcal{J}_{\epsilon_F+\epsilon_F\to\hbar\omega} = f_{FD}(\epsilon_F+\hbar\omega)[1-f(\epsilon_F)]P_E \tag{2.65a}$$

$$\mathcal{J}_E = \mathcal{J}_{\epsilon_F-\epsilon_F\to\hbar\omega} = f_{FD}(\epsilon_F-\hbar\omega)[1-f(\epsilon_F)]P_A \tag{2.65b}$$

Where, in a homogeneous medium, the probabilities of the absorption and emission of a phonon P_A, and P_E are given by [74],

$$P_A(\omega, T_e^*, T_0) = \frac{f_{BD}(\hbar\omega, T_0)(k_T + 2k_L)}{f_{FD}(\epsilon - \hbar\omega)v_F\left[\frac{k_L}{v_L} + \frac{2k_T}{v_T}\right] f_{BD}(\hbar\omega, T_0)(k_L + 2k_T)} \tag{2.66a}$$

$$P_E(\omega, T_e^*, T_0) = \frac{(f_{BD}(\hbar\omega, T_0) + 1)(k_T + 2k_L)}{f_{FD}(\epsilon - \hbar\omega)v_F\left[\frac{k_L}{v_L} + \frac{2k_T}{v_T}\right] (f_{BD}(\hbar\omega, T_0) + 1)(k_L + 2k_T)} \tag{2.66b}$$

where T_0 is the lattice temperature, k_T, and k_L are the wavevectors of the transverse and the two degenerate longitudinal phonons respectively.

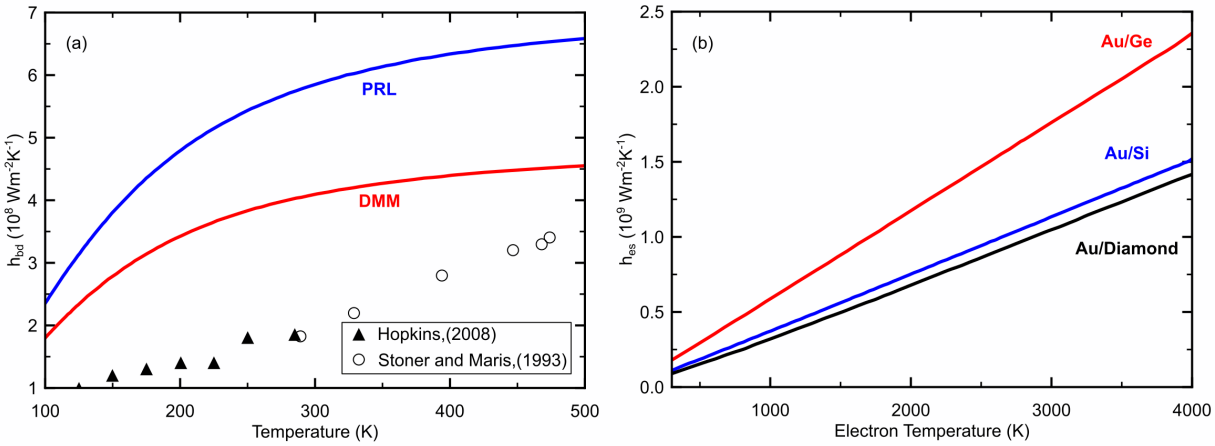

Figure 2.11: **The temperature dependence of Thermal boundary conductance models**: (a) Thermal boundary conductance across the Aluminum sapphire interface, with calculations of the DMM and PRL models. Data was acquired from [75], and [76]. The two models dramatically overpredict the transport across the interface, which Hopkins attributes to the influence of inelastic processes. (b) A supplemental model describing the role of nonequilibrium electrons at the interface of Gold and Si(blue), Ge(red), and Diamond(Black) [73]. As this model leverages the Debye model for the phononic structure it has limits in its application to real interfaces, but based on the calculations described there is plenty of flux in a non equilibrium electron distribution to influence interfacial transport.

Figure 2.11, provides exemplar calculations for each of the models presented in this section. Specifically, the predictions of the PRL and DMM fail to fit the trends across temperature, which necessitates further theoretical understanding of interfacial transport phenomena. The h_{es} predictions highlight the magnitude of flux available during phonon-electron nonequilibrium, and how those large fluxes might translate to strong coupling across the interface. It should be noted that more sophisticated models exist for computing the transfer probabilities in the above models, namely the Boltzmann transport [56, 77] and nonequilibrium greens functions [78], but a full

description of those models is outside the scope of this thesis. These large fluxes do not necessarily have to sink directly in to conductive pathways, instead intensely hot carriers also radiate via radiative processes.

Chapter 3

Metrology

3.1 Transient Thermoreflectance

After the invention of the laser, its uses in emergent measurement techniques have been widespread. With the ability to probe intimate material properties such as the interaction of electrons and vibrations, the overall structure of electronic bands, and thermal transport at the nanoscale, optical techniques have opened the door for novel investigations of previously only theoretical works. Cleverly, with the principles set forth by Scouler [79], Paddock and Eesley [80] used the changes in reflectivity of a thin metal film as a thermometer to measure the transient temperature changes at picosecond timescales. This transient thermoreflectance (TTR) method relied on the small thermal perturbations induced by a laser heater as a controlled input flux and a time delayed probe laser to interrogate the temperature induced reflectance changes as a thermometer. Although the relative thermoreflectivity $\left(\frac{\partial R}{\partial T}\right)$ of different material systems can vary wildly as long as the thermal event is kept small, the relationship is assumed to be linear as below,

$$\frac{\Delta R}{R} = \left(\frac{1}{R}\frac{\partial R}{\partial T}\right)\Delta T = C_{\mathrm{TR}}\Delta T \tag{3.1}$$

where R is the reflectivity of the surface of the material in vacuum at the baseline temperature, and C_{TR} is the coefficient of thermoreflectance.

TTR is the foundational method on which all pump probe thermometry techniques are based. It relies on the absorption of optical energy into the material by a "pump" laser beam, creating a temperature rise. Then, the reflectivity of the surface is measured with a "probe" beam during thermalization. With a fast enough sampling rate of the reflectivity, one can determine the surface temperature as it conductively cools to the larger cooler thermal bath of the substrate, thus determining the thermal properties governing this cooling mechanism. This process takes an amount

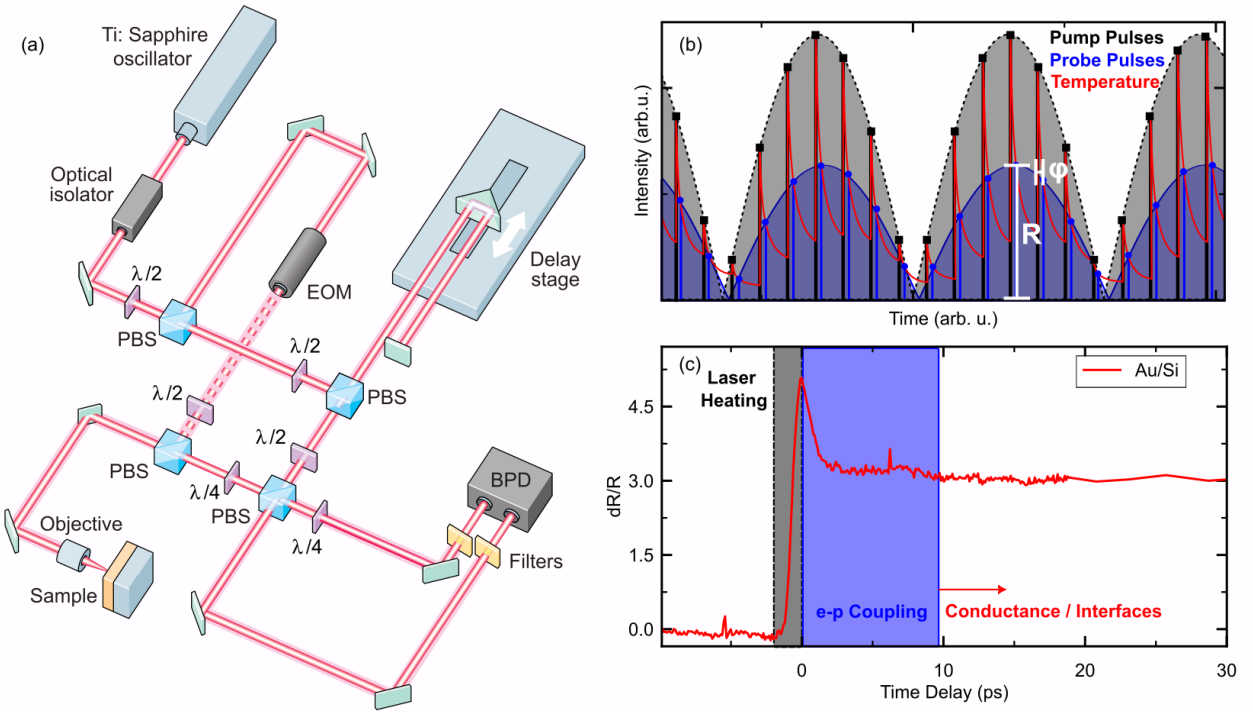

Figure 3.1: **Outline for thermoreflectance based pump probe measurements**: (a) A diagram of the table optics required for data collection; (b) a sample ultrafast thermoreflectance curve, with each non-equilibrium regime highlighted; (c) an example view of the relationship between the incident pump events and the detected reflectance signal. The magnitude R refers to the amplitude of the received waveform and the phase ϕ describes the physical lag between the input heat and the reaction of the physical system.

of time on the order of the conductive characteristic time described in the previous chapter. More critically for the present work, with even faster sampling rates one can determine non-thermal relaxation events such as those within the electronic or phononic subsystems. A generic diagram of laser-based transient thermoreflectance techniques is provided in Fig. 3.1 a. The characteristic timescales referenced here are laid out in Fig. 3.1 c, outlining the dominant non-equilibrium processes at each timescale.

The reflected signal is then compared to the incident beam to record the change in intensity and phase relative to the incident beam. This differential signal is then filtered for any oscillations at the pump modulation frequency, retrieving the phase, ϕ, the magnitude, R, of the reflected (see Fig. 3.1 b). Each of these signals can be selected for different thermometry techniques in order to extract the thermal properties of the system. Steady-state thermoreflectance (SSTR), uses only the magnitude at low modulation frequencies (where the phase difference is negligible) to compare

the maximum temperature rise at different absorbed powers. Frequency domain thermoreflectance (FDTR) sweeps across the modulation frequency, measuring the phase change of the reflected signal. Finally, time-domain thermoreflectance (TDTR) uses the curvature of the tangent of phase in time to predict the thermal gradients within the sample. As the main thrusts of this work are the use of a transient thermoreflectance method to observe mechanisms of heat transfer, rather than the direct determination of thermal properties in nanoscale systems, a full description of the auxiliary thermoreflectance methods used in my study have been omitted. The works of Cahill, Braun, and Schmidt can be referenced for more detailed and thorough design of FDTR [81], SSTR [82], and TDTR [83].

3.1.1 Spectrally tuned transient thermoreflectance

To study the ultrafast heat transfer processes of the optical phonons, we utilize an ultrafast pump-probe system with tunable probe wavelengths. Our experiment is built around a regenerative amplified laser system (Spectra Physics Spirit) emanating ∼400 fs, 1040 nm pulses at a repetition rate of 500 kHz. The output of this laser is directed into two paths, the "pump" and "probe". The pump path is frequency doubled to 520 nm then passed down a mechanical translation stage, which changes the path length relative to the probe pulse; in our configuration, we advance the delay line of the pump with respect to the probe to generate our transient reflectivity data. The pump beam is then chopped at a rate of 451 Hz and focused onto the surface of the sample of interest. The probe pulse gets passed through a mid-Infrared (MIR) optical parametric amplifier (OPA) which then outputs a range of wavelengths from 2 to 16 microns. The OPA splits the input beam into two paths. The first is used as a high-energy "Pump" (520 nm, the second harmonic, SH, of the seed), which is primarily used for power amplification of the input via a nonlinear crystal. After this amplification step, the result is referred to as the "Signal" beam (680-840 nm) and is used in mixing to generate the desired output. The second internal path is sent though a white light generation (600-1100 nm, WLG) crystal and is subsequently used for the process of amplification. Each amplification step results in additional photons which constitute the "Idler" beam (1350-2060 nm). These three beams have a simple relationship (below) between their wavelengths given by

the conservation of energy.

$$\frac{1}{\lambda_{\text{Idler}}} = \frac{1}{\lambda_{\text{Pump}}} - \frac{1}{\lambda_{\text{Signal}}} \tag{3.2}$$

A similar process of amplification is repeated using the Signal (680-850 nm) from the first amplification step, and the SH Pump are combined in a nonlinear crystal amplifying the Signal. This amplified Signal from the second amplification step and the fundamental seed (1040 nm residual after the SH generation) is combined one final time, resulting in the tunable Signal (1350-2060 nm) and Idler (2060-4500 nm) beams used as outputs. This tunability is derived from the spectral overlap of the pump and WLG pulses in the first amplification step. The two beams resultant from the final amplification step can finally be combined into a difference frequency generation (DFG) crystal for tunable output from 4-16 µm. In this work, we spectrally filter the Idler and Signal out of the path using a Germanium window and use wavelength from the DFG beam as the probe, allowing us to access probe wavelengths at 15 nm increments through a broad MIR spectrum based on the application. This probe is then focused onto the sample surface, centered around the pump. The relative positions and spot-sizes for each beam are measured via scanning slit broadband pyro-electric beam profiler, and are found to be $30 \pm 5\ \mu m^2$ for the pump beam at 520 nm, and $50 \pm 7\ \mu m^2$ for the probe beam at 5000 nm.

The sample is oriented on a sample holder such that the probe light incident on the surface is p-polarized. P-polarized light was chosen somewhat arbitrarily due to physical limitations on the measurement table. Transfer matrix method calculations (detailed below) were used to assure that the signals would be polarization-independent for each sample tested. The reflected probe signal is then measured by a HgCdTe photodetector sensitive to our frequency range (Vigo PC-4TE-14-1x1). Then, to filter out some noise in the raw signal, a lock-in amplifier is used at the chopper frequency of the pump modulation. The system used throughout this work then further filters the reflected signal by the native repetition rate of the pulse train to amplify the small signals present in the Infrared region even more. This data is then averaged for 1–3 seconds at each time delay to reduce overall variance of the reported data. We monitor this transient thermoreflectivity scans at different probe wavelengths, shown in the chapters**??**.

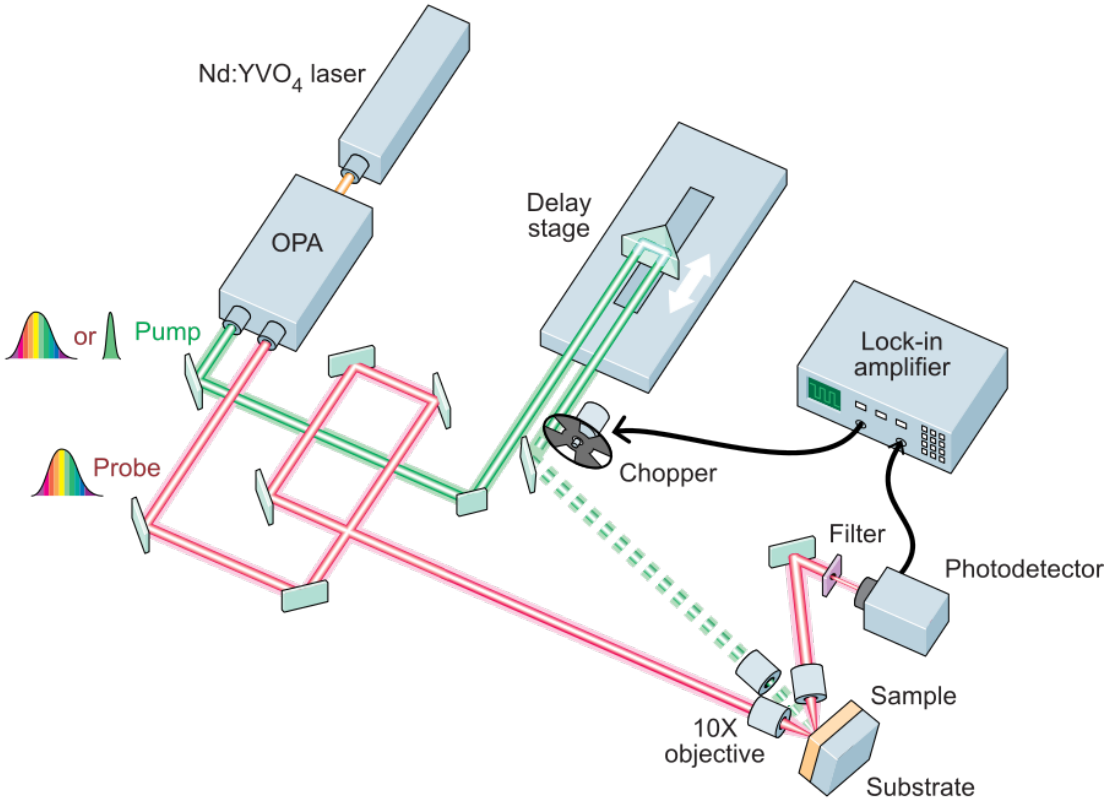

Figure 3.2: **Transient Infrared Thermoreflectance**. A 400 fs 500 kHz pulsed Nd:YVO4 seed laser is piped across an optical table and path length matched with an second harmonic generated optical pump pulse.

3.2 Variable-Angle Spectroscopic Ellipsometry

The dielectric function of samples is often at the heart of any optical measurement technique, and even simple metallic systems can vary dramatically from sample to sample [84, 85]. For this reason, when a testing a novel material, we must measure the dielectric properties before investigating the thermal transients within the system. To determine the dielectric character of a system, we use variable-angle spectroscopic ellipsometry (VASE). The principle of the technique relies on light's interaction with a medium changing the polarization of the reflected beam, best summarized by what is called the ellipsometry equation [86],

$$\frac{r_p}{r_s} = \rho = \tan(\Psi)e^{i\Delta} \tag{3.3}$$

where r_p and r_s are the Fresnel reflection coefficients for p and s polarized light respectively*. ρ, Ψ and Δ are frequency dependent fitting terms used in the analysis of data. The measurement is performed by linearly polarizing a broadband light source and reflecting this light off of an unknown sample at a set angle. The reflected light is then analyzed across spectra to find its exact polarization components determined. The resultant fitted terms can then be used to calculate the exact complex dielectric function ε,

$$\varepsilon = \varepsilon' + i\varepsilon'' = (n + ik)^2 = \sin^2(\theta_i)\left[1 + \tan^2(\theta_i)\left(\frac{1-\rho}{1+\rho}\right)^2\right] \tag{3.4}$$

where θ_i is the angle of the incident beam.

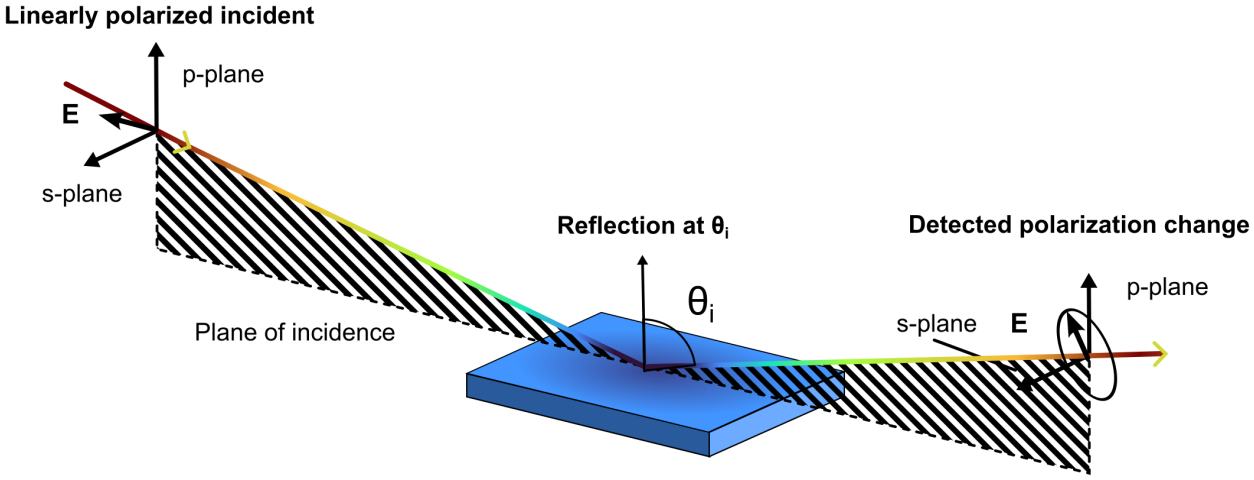

Figure 3.3: **Variable-angle spectroscopic ellipsometry**. A linearly polarized broadband light source incident on a sample surface will be reflected as elliptically polarized.

A schematic of the VASE technique is provided in Fig. 3.3. The dielectric measurements detailed in this thesis were performed primarily on the JA Woollam IR-VASE system. This system measures in the spectral range of 2000 to 30000 nm. Some auxiliary measurements were made using the JA Woollam M2000 VASE system in the range from 200 to 1700 nm. As the VASE technique measures the ratio of the $s-$ and $p-$ polarized light for analysis, it is highly accurate, and can reproducibly

*The polarization of light is often de-convolved into components that are in-plane, relative to the sample surface, s, and out of plane to the sample surface, p [87].

measure the optical constants or even the thickness of individual layers in a stack [88, 89].

3.3 Simulations and Analysis

3.3.1 Density Functional Theory

Determining the intrinsic scattering parameters of individual carriers of a system relies on the assumptions made in the prediction of exact dispersions of thermal carriers and interactions between thermal baths. To reduce the total assumptions in the simulations in this thesis, we determine the electronic and phononic interactions with an *ab initio* approach to predict the ground state configuration of the electronic structure. Every interaction between the electrons and the lattice is governed by some Hamiltonian, (H). Under the assumption that the electrons and lattice behave based on coulombic interactions, Born and Oppenheimer [90] separated the degrees of freedom between the electrons and the nuclei. Furthermore, by this approximation, electronic motion is governed by the time independent Schrödinger equation,

$$H_e \Psi_n = E_n \Psi_n \tag{3.5}$$

where E_n and Ψ_n refer to the n^{th} energy and wavefunction of the n^{th} eigenstate of the electronic Hamiltonian H_e, which depends on the exact repulsion and attraction kinetics between the electron and a lattice site or nuclei .

Density functional theory (DFT) was first postulated by Hohenberg and Kohn's seminal work [91], where they posit that knowledge of the ground state electron density we can determine all electronic properties in both excited and ground states. By the Rayleigh-Ritz variational principle, the universal energy functional takes the form,

$$E(n) = \int V_e(\mathbf{r}) \rho_e(\mathbf{r}) + F(\rho_e) \tag{3.6}$$

where F is the functional of the electron density ρ_e, valid for any number of particles and any potential. Minimizing this energy functional will reveal the ground state energy of the electronic system and therefore, can predict the properties for a given potential. In modern approaches to this minimization process, it is common to shift this complex form of the energy functional to the

Kohn-Sham approach [92],

$$E(n) = 2\sum_{n=1}^{N/2} E_n + E_x(n) - \frac{e^2}{2}\int \left[V_{SCF}(\mathbf{r}')n(\mathbf{r}) - v_x(\mathbf{r})n(\mathbf{r})\right] d\mathbf{r}d\mathbf{r}' \tag{3.7}$$

where N is the total number of electrons in the system, V_{SCF} refers to the self-consistent field, and E_x and v_x refer to the exchange correlation energy and potential, respectively. This equation can be now solved in various self-consistent ways giving all electronic properties, that is assuming one can find some exchange correlation energy E_x. Over 200 approximations have been attempted to obtain E_x.[†] These methods range from the simplest, the local density approximation [92], to a more complex the Hartree-Fock method [93], or even Monte-Carlo numerical solutions. Once an approximation is made, small perturbations can be made to the interatomic potentials and electronic density, resulting in a perturbative theory which can result in a numerical solution to not only the electronic structure and properties, but also output the phonon bands and interactions as well [94]. An aggregation of these ab initio methods is provided in the open-source software Quantum Espresso [50]. The dissertation work below uses this software, with a self-consistent field approach under standard pseudo-potentials [95].

3.3.2 Two-Temperature Model

For TDTR, the two-temperature model (TTM) [96, 97] can separate the temporal dynamics of two thermal baths. As another pulsed pump-probe technique, the IR-TTR system will utilize a similar, but more general framework. There are three different temporal regimes that the IR-TTR measurement is sensitive to: thermal excitation, ultra-fast coupling, and diffusive propagation. At timescales before thermal equilibrium, we see at least two competing temperatures. The temperatures of the non-equilibrium bath and the diffusive bath. The dynamics of the non-equilibrium bath can vary with sample, probe frequency, and nature of the thermal event. As an example, we can devise a measurement of the thermal oxide on a Si wafer. Using a visible pump and an infrared probe centered at the edge of the Reststrahlen band of SiO_2 IR-TTR will be sensitive to three subsystems. First, we would have ultrafast electronic heating of the electrons in Si proportional

[†]The exchange correlation energy is so confounding that even Richard Feynman referred to it as the *stupidity energy*, as the accuracy of DFT models depends on the approximations used.

to the pulse width of the pump. Then, as it has been shown that non-equilibrium electrons can preferentially heat TO phonon modes [98–100], we must consider the coupling of heat across this pathway first. Finally, the reflectivity will trend with the diffusive processes at play within the SiO_2. Even in this simple thought experiment, TTM is insufficient to describe the dynamics at play.

To remedy this, we can use different models to describe thermal systems in non-equilibrium, such as the Boltzmann transport equation (BTE) [101, 102] and non-thermal lattice model (NLM) [103]. As each has its merits, our hypotheses and intuition on the thermal dynamics of the system should infer what model is used. In general, for unknown monolithic samples, BTE informed by prerequisite density functional theory (DFT) [50] will require the least number of assumptions. This makes it the most realistic simulation of thermal transfer. However, when in more complex systems such as layered structures with physically predictable parameters, the simpler NLM or TTM can be used. In the below work, we will primarily use the NLM for our analysis as it is the simplest model that can still describe systems with a complex quasi-particle landscape. The NLM is at its foundation a solution to the heat equation with multiple thermal baths. We begin with the heat equation as,

$$\frac{\partial T}{\partial t} = \frac{\kappa}{C_v}\nabla^2 T \tag{3.8}$$

NLM then makes the approximation that the temperature in the system is broken into $N_\mu + 1$ different equations, where N_μ is the number of different phonon modes that are activated plus one more associated with the individual modes' coupling to the electronic subsystem (g_μ),

$$C_p^\mu \frac{\partial T_p^\mu}{\partial t} = \nabla \cdot (\kappa_p^\mu \nabla T_p^\mu) + g_\mu (T_e - T_p^\mu) + \sum_\mu \frac{T_p^{\mu'} - T_p^\mu}{\tau_{\mu'\mu}} \tag{3.9}$$

$$C_e \frac{\partial T_e}{\partial t} = \nabla \cdot (\kappa_e \nabla T_e) + \sum_\mu^{N_\mu} g_\mu (T_p^\mu - T_e) + S(x,t) \tag{3.10}$$

where $\tau_{\mu'\mu}$ is the lifetime of the non-thermal phonon μ' and the thermal phonon μ collision, and C_p^μ, κ_p^μ, g_μ and C_e, κ_e are the heat capacities, thermal conductivities and coupling parameters [103] of the μ^{th} phonon band and electrons, respectively. These equations can be solved numerically at each node of space and each time-step with the Crank-Nicolson finite difference method [104].

Finally, $S(x,t)$ is a pulsed laser source term applied to the surfaces as a pump to the electrons, or phonons depending on the pump frequency. The laser source term is defined as ,

$$S(x,t) = \sqrt{\frac{4\ln(2)}{\pi}}\frac{(1-R)\phi}{\delta t_p} \times \exp\left\{-\frac{x}{\delta} - 4\ln(2)\left[\left(\frac{t}{t_p}\right)^2\right]\right\} \tag{3.11}$$

t_p, ϕ, R and δ are the pulse duration, applied laser fluence, reflectivity of the surface, and the optical penetration depth respectively. NLM is general enough to be sufficient to calculate any heat capacity, thermal conductivity and scattering rate from p to p' or e to p. Thus, with clean and artifact-free temporal information, we can extract the thermal collision rates and dominant carriers in each layer. We can also simplify the above model to a simple TTM used in TTR experiments by stetting $N_\mu = 1$, essentially simplifying the phononic subsystem to a single bath of carriers, appropriate for cases of thermalized phonons.

3.3.3 Scattering and Transfer Matrix Methods

When simulating the reflection and absorption of light for some bulk material, the classical Fresnel coefficients [87] are ideal. However, for complex multilayer stacks maintaining the bookkeeping for all polarizations and all frequencies at each interface can become nontrivial. To simplify this, A matrix method is used where each layer and interface can be assembled into a large matrix to which the incident wave can be applied and the reflected and absorbed electric field can be solved.

There are two main matrix methods which treat the interface between materials differently, but foundationally they are solutions to the electric fields of Maxwell's Equations. Therefore, each method is merely a functional change in formalism, and solutions are equivalent. The scattering matrix method (SMM) [105, 106], relates the incident fields to the outgoing electric fields at a given interface. The transfer matrix method (TMM) [107, 108] instead relates the incident and outgoing fields on one side of an interface to those across an interface. In the near field radiation formalism given by Francoeur [66], he uses a scattering matrix approach to solve Maxwell's Equations under the fluctuation dissipation theorem. However, to solve for the final transfer coefficients between radiating bodies, the TMM must be used.

As the methods are mathematically equivalent, for convenience I will briefly describe the formulation of TMM. Fig. 3.4 depicts the system our simulation will be approximating, where the

electric field $|\vec{E}|$ is to be computed at any position z within the stack, via the transfer matrix.

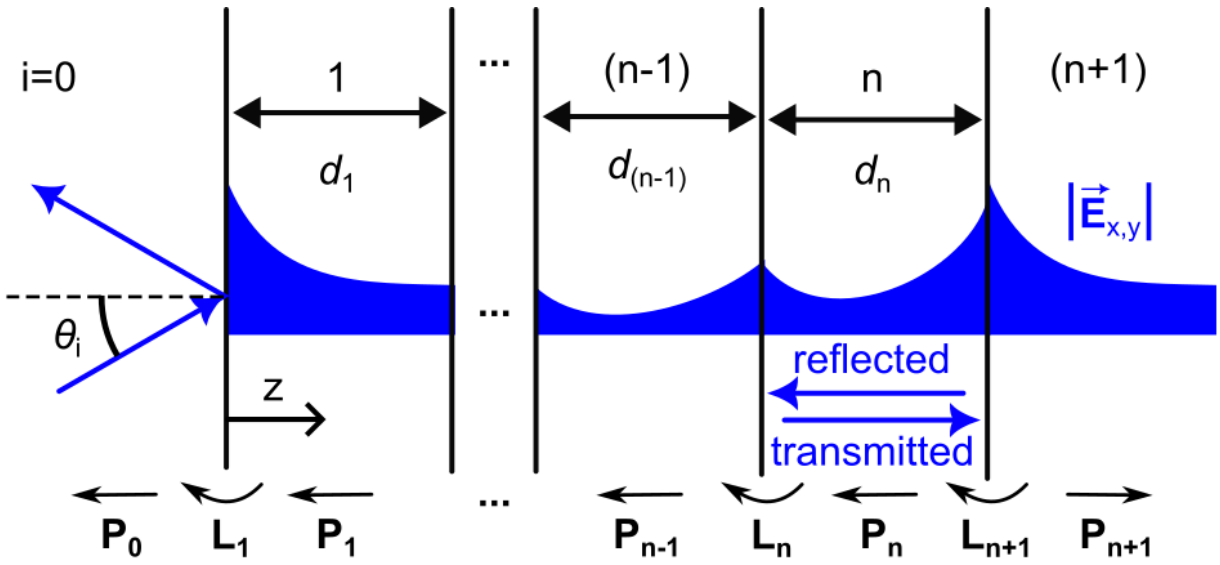

Figure 3.4: **Transfer Matrix Method**. The distribution of the electric field at any point within a multilayer stack can be calculated by multiplication of each propagation matrix **P** and interface matrix **L**.

The transfer matrix Γ_n is,

$$\Gamma_n = \mathbf{L}_{n+1} \prod_{n=0}^{n} \mathbf{L}_n \mathbf{P}_n \tag{3.12}$$

where **L**, and **P** are the interface and propagating matrices defined at each position below,

$$\mathbf{P}_n(z) = \begin{bmatrix} e^{i\frac{\omega}{c}q_{1,n}z} & 0 & 0 & 0 \\ 0 & e^{i\frac{\omega}{c}q_{2,n}z} & 0 & 0 \\ 0 & 0 & e^{i\frac{\omega}{c}q_{3,n}z} & 0 \\ 0 & 0 & 0 & e^{i\frac{\omega}{c}q_{4,n}z} \end{bmatrix} \tag{3.13a}$$

$$\mathbf{L}_n = \mathbf{A}_{n-1}^{-1}\mathbf{A}_n \tag{3.13b}$$

where $q_{j,i}$ is the j^{th} eigen mode for layer, i, which specify the polarization and propagation direction for the electric field. The intermediate matrix, **A**, is,

$$\mathbf{A}_n = \begin{bmatrix} \gamma_{n,11} & \gamma_{n,21} & \gamma_{n,31} & \gamma_{n,41} \\ \gamma_{n,12} & \gamma_{n,22} & \gamma_{n,32} & \gamma_{n,42} \\ \frac{1}{\mu_n}(q_{n,1}\gamma_{n,11} - \xi\gamma_{n,13}) & \frac{1}{\mu_n}(q_{n,2}\gamma_{n,21} - \xi\gamma_{n,23}) & \frac{1}{\mu_n}(q_{n,3}\gamma_{n,31} - \xi\gamma_{n,33}) & \frac{1}{\mu_n}(q_{n,4}\gamma_{n,41} - \xi\gamma_{n,43}) \\ \frac{1}{\mu_n}q_{n,1}\gamma_{n,12} & \frac{1}{\mu_n}q_{n,2}\gamma_{n,22} & \frac{1}{\mu_n}q_{n,3}\gamma_{n,32} & \frac{1}{\mu_n}q_{n,4}\gamma_{n,42} \end{bmatrix} \tag{3.14}$$

where ξ, and $q_{n,j}$ are eigenmodes of the incident and intrinsic electric field, respectively solved in Refs. [108] and [109]. $\gamma_{n,jk}$, and μ_n are both direct functions of the dielectric function of the media at layer n and are also provided in Refs. [108], and [110]. We then obtain the reflection and transmission coefficients for the entire structure [111],

$$r_{pp} = \frac{\Gamma^*_{21}\Gamma^*_{33} - \Gamma^*_{23}\Gamma^*_{31}}{\Gamma^*_{11}\Gamma^*_{33} - \Gamma^*_{13}\Gamma^*_{31}} \qquad t_{pp} = \frac{\Gamma^*_{33}}{\Gamma^*_{11}\Gamma^*_{33} - \Gamma^*_{13}\Gamma^*_{31}} \tag{3.15a}$$

$$r_{ss} = \frac{\Gamma^*_{11}\Gamma^*_{43} - \Gamma^*_{41}\Gamma^*_{13}}{\Gamma^*_{11}\Gamma^*_{33} - \Gamma^*_{13}\Gamma^*_{31}} \qquad t_{ss} = \frac{-\Gamma^*_{11}}{\Gamma^*_{11}\Gamma^*_{33} - \Gamma^*_{13}\Gamma^*_{31}} \tag{3.15b}$$

$$r_{sp} = \frac{\Gamma^*_{41}\Gamma^*_{33} - \Gamma^*_{43}\Gamma^*_{31}}{\Gamma^*_{11}\Gamma^*_{33} - \Gamma^*_{13}\Gamma^*_{31}} \qquad t_{sp} = \frac{\Gamma^*_{31}}{\Gamma^*_{11}\Gamma^*_{33} - \Gamma^*_{13}\Gamma^*_{31}} \tag{3.15c}$$

$$r_{ps} = \frac{\Gamma^*_{11}\Gamma^*_{23} - \Gamma^*_{21}\Gamma^*_{13}}{\Gamma^*_{11}\Gamma^*_{33} - \Gamma^*_{13}\Gamma^*_{31}} \qquad t_{ps} = \frac{\Gamma^*_{13}}{\Gamma^*_{11}\Gamma^*_{33} - \Gamma^*_{13}\Gamma^*_{31}} \tag{3.15d}$$

where r and t are the new Fresnel-like coefficients of a complex stack, and Γ^*_{xy} are the components of the transfer matrix, Γ, transformed to comply with the formalism set out by Ref. [111].

Chapter 4

Interfacial Heat Transport via Evanescent Radiation by Hot Electrons

This section focuses on the development of current near field radiation theory to envelop the radiation transported through metal-dielectric interfaces in the presence of nonequilibrium electrons. The work presented in this section has been accepted in *Physical Review Letters*.

4.1 Background

The thermal boundary conductance (TBC) between two solids relates the heat flux, q, to the temperature drop ΔT across the interface. Over the past few decades, theories that describe the interactions among electrons and phonons at interfaces have elucidated various fundamental carrier scattering and conversion processes that drive these interfacial thermal transport pathways [69, 112–116].

One of the most fundamental and ubiquitous transfer mechanisms, thermal radiation, has been neglected in this interfacial heat transfer discussion and concomitant thermal boundary conductance theories. The relatively small fluxes inhibited by the blackbody limit seem negligible when compared to traditionally studied conductive pathways driven by electrons and phonons. In recent years, there has been a renewed interest in this field due to the verification of the prediction of super Planckian enhancement due to the contribution of evanescent modes [117–119]. This is of special importance in the 'near-field' regime, when the separation distances are smaller than the thermal wavelength [120]. The contribution of evanescent radiative modes can be the dominant thermal transport mechanism within these distances [121]. With the ability of evanescent radiative heat transfer (RHT) to exceed the blackbody limit, many experiments have been performed for a range of different geometries, materials, and gaps ranging from micrometers down to nanometers [122, 123]. Due to this new

capability, there is growing interest in the effect that evanescent RHT can have on various thermal technologies such as thermophotovoltaics (TPVs) [124], heat-assisted magnetic recording (HAMR) devices [125, 126], scanning thermal microscopy [127, 128], and coherent thermal sources [32, 129, 130]. Hence, we must envelop our standard thermal theory of interfacial transport [69] to leverage evanescent RHT in the solid state.

The largest RHT enhancements in natural materials have been reported in polar dielectrics, such as SiC, SiO_2, and hBN, where phonon polariton (PhPs) dominate the evanescent modes [131, 132] in the near field as predicted via Rytov's formalism of fluctuational electrodynamics [67, 133]. This theory predicts thermal radiation mediated by all propagative, frustrated and surface modes at an arbitrary distance from an emitting body. The frustrated and surface modes are not allowed to propagate outside the emitting body (i.e., they are evanescent), as the parallel component of the wavevector (k_ρ) for these modes is greater than the free-space wavevector (k_0). However, when another medium is brought close to this body, the evanescent modes can be coupled to the receiving system, and the heat is transported radiatively. The interfaces adjacent to polar dielectric systems are also the source of major thermal boundary resistances due to the large phononic mismatches that occur at metal/dielectric interfaces in devices [113, 116], thus heavily reducing the possible thermal management at these scales. To compound this, the electrons of metal interconnects are often an order of magnitude hotter than the phonon subsystem during operation [134]. Capitalizing on evanescent RHT, the thermal boundary conductance across metal/dielectric interfaces can be tuned by using the electron-phonon non-equilibrium.

4.2 Simulation details

In this Letter, we model the transduction of thermal radiation from a metallic emitter into an insulating dielectric substrate, specifically under the case of strong electron-phonon non-equilibrium. By leveraging the formalism of fluctuational electrodynamics (FED) as well as the classic Drude-Sommerfeld theory of free electrons [60], we also examine the effect of electron temperature in the metallic thin film on interfacial radiative conductance, h_{rad}, in the presence of polaritonic and hyperbolic insulators. By doing so, we demonstrate that there can be more than two-fold increases in overall thermal interfacial transport at high electron temperatures due to the contribution of

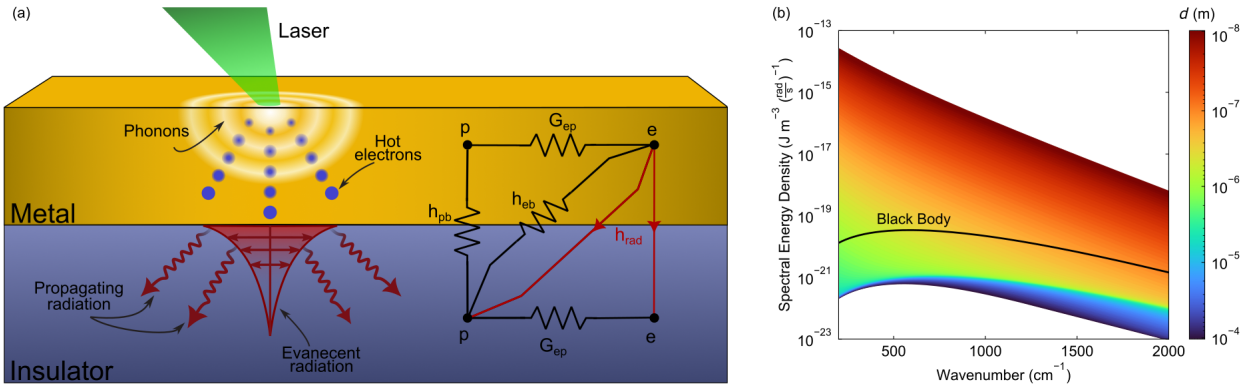

Figure 4.1: (a) Diagram of interfacial transport phenomena. The schematic depicts energy transfer processes between electrons (e), phonons (p), and boundary (b) immediately after an ultrashort laser pulse is absorbed. The evanescent and propagating radiation due to ballistic hot electrons is absorbed into the substrate based on the dielectric properties beneath the interface. (b) The spectral energy density due to radiation of propagating and evanescent modes from a gold film at a distance d (shown in the color bar) away from the surface calculated using FED. The solid black line shows the far-field blackbody limit.

evanescent radiative heat flux at metal-insulator interfaces.

The configuration studied here is schematically depicted in Fig. 4.1a, where non-equilibrium is illustrated as the separation in thermal energy immediately after excitation from short pulsed laser absorption. Another example of this non-equilibrium occurs in the gate of high-frequency electronic devices [130, 135, 136]. These events can cause the electronic bath at temperatures of thousands of Kelvin while maintaining a cold lattice. This non-equilibrium manifests as the opening up of the Fermi surfaces, resulting in an increase in the population and the scattering rates of conducting electrons [137–140]. These increases open up possible radiative photonic states in both the propagating and evanescent regions of the photonic dispersion. The proposed mechanism of RHT across interfaces is fueled by the absorption in insulating dielectrics. These dielectric materials with high indices can courie the evanescent modes from the metal into high-wavevector photonic states, enhancing thermal transport.

All the processes of the thermal transfer across the interface are depicted in Fig. 4.1a, where 'e' and 'p' refer to the electronic and phononic subsystems, respectively. Each material has its electron-phonon coupling rate, G_{ep} [96], at which electronic energy is converted to phonon energy. The conductance across the interface includes the phonon contribution to the boundary resistance (h_{pb}) [69] and the contribution associated with electron collisions at the interface producing phonons

in the insulator (h_{eb}) [73]. Finally, there exists a conductance associated with the mechanism proposed by this work, where the thermal radiation emitted by the electrons may be absorbed into the phonons or electrons in the substrate (h_{rad}). To represent the scale of available energy contained in thermally excited evanescent modes of a metallic emitter, we calculate the energy density at a distance d away from a gold layer with bulk properties (Fig. 4.1b) using FED [65, 67, 118]. As d decreases, the emitted flux increases due to the evanescent contribution, such that it exceeds the blackbody limit by several orders of magnitude.

The formalism for thermal emission by a system with non-equilibrium carriers was provided by Greffet *et al.* [141] asserting that the subsystem temperature of a carrier in non-equilibrium should be used along with its contribution to the dielectric function. Thus, the emission of the metallic layer is dominated by the free-electron contribution during non-equilibrium and before electron-phonon thermalization (i.e., at timescales less than ~ 10 ps after an electronic excitation). At this short time scale, there is an opportunity to sink this heat before the bulk system reaches a high-entropy equilibrium dominated by diffusive processes. The dielectric behavior of free electrons is described by the Drude model as

$$\varepsilon_m(\omega) = 1 - \frac{\omega_p^2}{\omega^2 + i\omega\Gamma_{tot}} \tag{4.1}$$

where ω_p is the plasma frequency and Γ_{tot} is the total electronic scattering term. As the Drude model predicts a broadband dielectric function across the infrared region of the spectrum (where most of the RHT occurs), the spectral energy density due to thermal emission by the metallic layer also exhibits a broadband behavior, as shown in Fig. 4.1b for gold as an example.

When considering a non-equilibrium system with elevated electron temperatures, we need to investigate the scope of the Drude oscillator parameters (i.e., ω_p and Γ_{tot}) which varies noticeably with electron temperature. The strength of the Drude oscillator is given by the plasma frequency defined as

$$\omega_p(T_e) = \sqrt{\frac{n_e(T_e)e^2}{4\pi m^*(T_e)\epsilon_0}} \tag{4.2}$$

where e and ϵ_0 are the elementary charge and free-space permittivity, respectively. The parameters which depend on the electron temperature, T_e, are the effective mass (m^*) and the number density

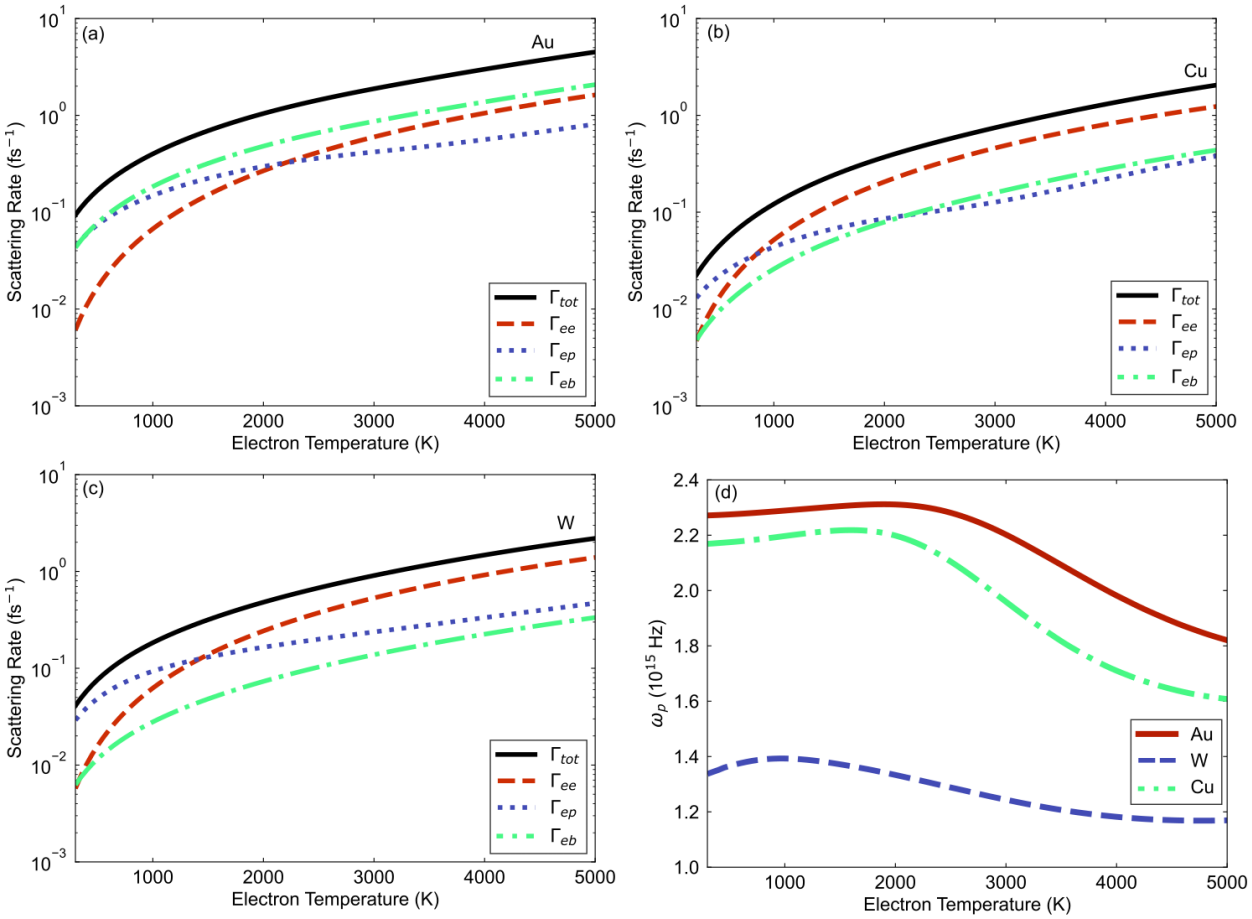

Figure 4.2: (a)-(c) Electron-electron, electron-phonon, electron-boundary, and total scattering rates in a film of gold, copper, and tungsten, respectively. The thickness of the film is set to 10 nm. (d) Electron temperature trend of the plasma frequency for each metal film.

of electrons (n_e) given by integrating the occupied density of electronic states over all energies. The temperature dependencies of m^* and n_e can be computed from the total electron density of states (eDOS) and the chemical potential, μ, detailed in the Supplemental Materials.

There is also a sizable increase in the total electronic scattering rate, Γ_{tot}, at high temperatures due to the increase in average collisions experienced by electrons at the broadened Fermi surface. The classic Drude model assumes independent electrons, but at the nanoscale, elastic collisions between electrons and boundaries become significant. To account for this effect, we extend the Drude model using Matthiessen's rule [142], providing a more accurate total relaxation time, Γ_{tot}, as

$$\Gamma_{tot} = \Gamma_{ee} + \Gamma_{ep} + \Gamma_{eb} \tag{4.3}$$

where Γ_{ee}, Γ_{ep}, and Γ_{eb} are the electron-electron, electron-phonon, and electron-boundary scattering rates, respectively. Each of these rates can be calculated from first principles under the theories of Fermi liquid theory (FLT) [57, 143], electronic Cerenkov radiation of sound waves [58], and inelastic electron scattering from a vibrating boundary [71], with the inputs taken from refs. [50, 137] (see Supplemental Materials for details). Throughout the simulations performed in this work, we consider a metal film thickness of 10 nm with a 'cold' lattice, i.e., $T_p = 300$ K. This assumption represents the initial transient phase of strong electron-phonon non-equilibrium following an intense electronic excitation. During this scenario, T_e can reach thousands of Kelvin while T_p remains nearly constant on the timescale of picoseconds due to the relatively slow electron-phonon energy exchange. This isolates the impact of hot electrons on radiative heat flux in non-equilibrium conditions, such as after ultrafast laser excitation [144] or during high-power electronic device operation [134, 145].

The temperature dependence of these scattering rates along with the total scattering rate in three representative metals (i.e., Au, Cu, and W) are shown in Fig. 4.2a-c. At the low-temperature limit of $T_e \sim 300$ K, the dominant mechanism is electron-phonon scattering as the system is close to equilibrium and the phonons scatter more readily since they have higher heat capacity than the free electrons. At electron temperatures higher than 2500 K, this trend inverts and the self-interaction of the electronic sea, i.e., the electron-electron scattering, dominates over the electron-phonon counterpart. While all three metal films show somewhat similar electron-electron scattering rates, the gold film exhibits a higher electron-phonon scattering rate than copper and tungsten. Although gold has the lowest electron-phonon coupling among these three metals [137], the electron-phonon scattering rate is the highest since gold has the lowest sound speed (see Supplemental Materials). Additionally, the lower sound speed in gold causes electron-boundary scattering to be the dominant contributing mechanism to the total scattering.

Fig. 4.2d shows the trends in the plasma frequencies, where Au and Cu exhibit a characteristic downturn, in contrast to the relatively stable trend in tungsten. Gold and copper are both noble metals that conduct via their outer s-band at lower temperatures. The general trend for these noble metals is a trend upward in number density at moderate electron temperatures ($T_e < 2000$ K) due to Fermi smearing into the d-bands, resulting in a increase in ω_p. However, at higher temperatures, the tail of Fermi smearing starts to gain access to the heavy d-bands. Hence, while the number density keeps increasing, the competing effect of the effective mass of the d-band electrons dominates

the trend at $T_e > 2000$ K and thus, decreases ω_p . Tungsten, a non-noble transition metal, has a much smoother trend with electron temperature due to the d-bands participating in conduction throughout the temperature ranges simulated.

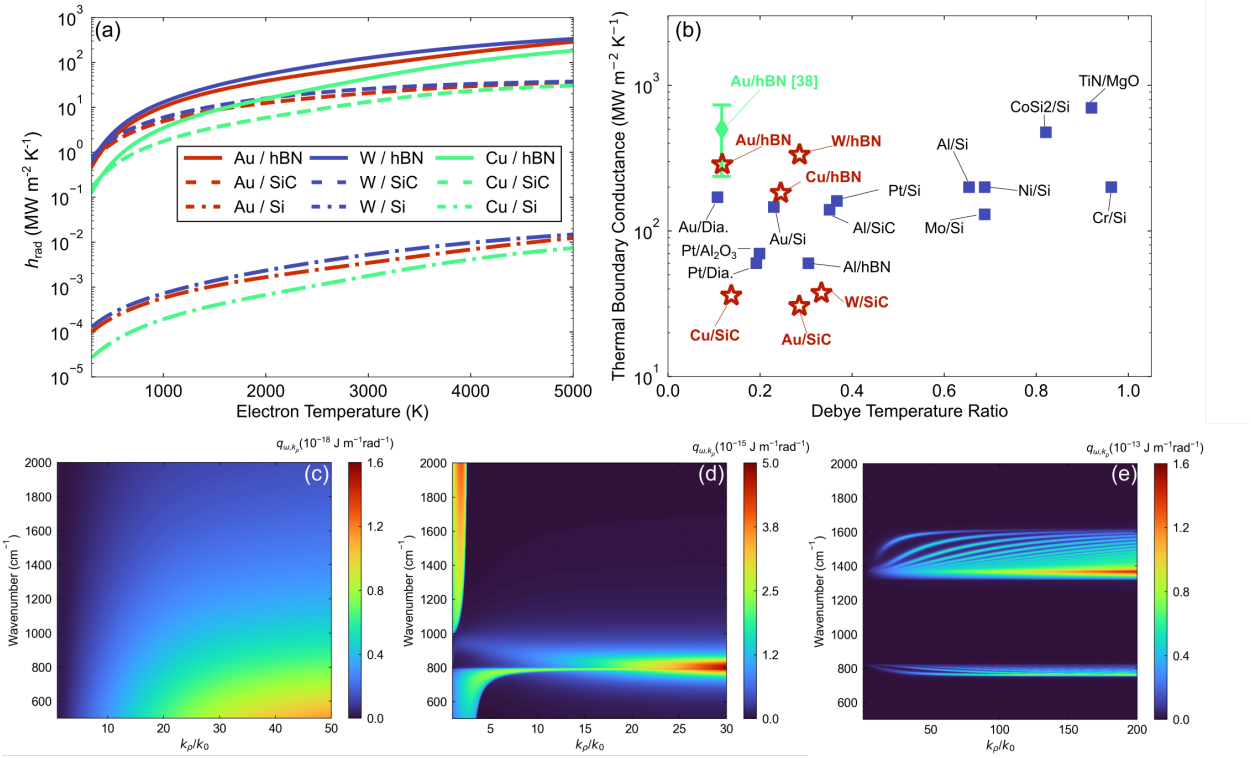

Figure 4.3: (a) FED predictions of radiative TBC at varying electron temperatures. The highest h_{rad} can be expected from the absorption into high-wavevector phonon polaritons in hBN and SiC. The lack of polaritonically active optical modes in the Si results in small values of h_{rad} during non-equilibrium. (b) Comparison of non-equilibrium h_{rad} calculated in this work (red stars) with measured TBC values at non-equilibrium (green diamond [146]) as well as room-temperature phonon-phonon TBCs (blue squares [113]). The values of TBC are plotted against the ratio of the film and substrate Debye temperatures, which gives a first approximation to the effective acoustic impedance matching used to estimate the efficiency of interfacial phonon transport. (c)-(e) Representative dispersion of evanescent radiative spectral heat flux per unit wavevector transferred from the metal to the substrate in the cases of 10-nm Au film with $T_e = 5000$ K on Si, 3C-SiC, and hBN, respectively.

With the Drude parameters calculated at high electron temperatures, we can utilize FED to determine the radiative heat flux associated with propagating and evanescent modes across the interface between the metallic thin film and an insulator substrate [66, 147] , as described in Appendix C. This flux is then used to calculate the thermal boundary conductance with $\Delta T = T_e - T_p$. We considered three semi-infinite substrates (i.e., Si, 3C-SiC, and hBN) with different

dielectric behaviors in the infrared region. While Si does not support any optical features that would significantly enhance the radiative heat flux, 3C-SiC and hBN can support evanescent polaritonic modes [148] that cause a resonant increase in the heat flux. 3C-SiC is an isotropic polar wide-bandgap semiconductor with a large transverse optical (TO) absorption peak in the infrared region and supports phonon polaritons [65, 149, 150]. Also, hBN is an anisotropic uniaxial medium with different in-plane and cross-plane dielectric functions. hBN possesses two hyperbolic spectral regions, in which the in-plane and cross-plane dielectric functions have opposite signs and hyperbolic phonon polaritons can be excited resulting in a broadband enhancement of radiative heat flux [151]. The dielectric functions of these substrate materials are found using available literature parameters [64, 148].

4.3 Near Field Radiative Calculation

Fig. 4.3a shows the calculated results for evanescent radiative conductances, h_{rad}, for all nine interfaces. We observe a two-order-of-magnitude increase in the interfacial radiative conductance at high electron temperatures when compared to near-equilibrium conditions (i.e., low T_e). The magnitude of these radiative conductances, however, is only significant for polar substrates with strong dipole oscillators supporting strong resonant modes at high wavevectors. For polaritonically active substrates, the value of h_{rad} approaches the order of conductive transport ($\sim 100'$s MW m^{-2} K^{-1}) [113] at electron temperatures above 3000 K. Fig. 4.3b presents a range of literature values for total TBC measured during local thermodynamic equilibrium, i.e., $T_e = T_p = 300$ K. Comparing our calculated values at $T_e = 5000$ K to the literature values, we see that h_{rad} can be the dominant mechanism under non-equilibrium. Au and W show the highest evanescent transfer to polaritonic substrates, up to 333.7 MW m^{-2} K^{-1} at $T_e = 5000$ K. In the case of tungsten, this is due to the dramatically lower ω_p of the metal (see Fig. 4.2d), resulting in a small negative dielectric function allowing more modes through the metal-insulator interface. Gold compensates for a high ω_p with overall higher scattering rates which broaden the envelope of evanescent modes and results in a comparable flux to that of W (see Section B of the Supplemental Materials for sensitivity of heat flux to each Drude term).

We focus on electron temperatures up to 5000 K to model scenarios of strong electron-phonon

non-equilibrium, where electrons transiently reach high temperatures before thermalization with the lattice. The only measured value of radiative TBC in such non-equilibrium conditions is for Au/hBN interface, reported by Hutchins *et al.* [146]. The ultrafast heat transfer measurement described in Ref. [146], involving evanescent coupling between hot electrons in gold and hyperbolic phonon polaritons in hBN, aligns with the theoretical predictions presented here. The reported "polaritonic interface conductance" of 500 MW m^{-2} K^{-1} at high electron temperatures agrees within uncertainty with our calculated h_{rad}.

To elucidate the effect of substrate on the radiative flux, we show the spectral heat flux per unit k_ρ emitted by the gold film with $T_e = 5000$ K into the three substrates in Figs. 4.3c-e. The absorption from the Drude oscillator in Si results in a weak broadband heat flux. In the case of 3C-SiC (Fig. 4.3d), the radiative heat flux is dominated by the excitation of bulk phonon polaritons at lower wavevectors and the TO absorption at high wavevectors. The latter occurs at a narrow spectral region, resulting in a quasi-monochromatic heat flux between the metallic layer and the substrate. The transfer of flux across the interface is dictated by the allowed electromagnetic modes at each side of the interface; thus, the strongest optical phonons and/or polaritons result in the most radiative flow. The metal-substrate paring that resulted in the highest h_{rad} was that of W on hBN due to the intense absorption into the high-wavevector hyperbolic phonon polaritons excited within two hyperbolic regions of hBN, as illustrated in Fig. 4.3e. These hyperbolic modes result in a directional volumetric sinking of heat from the emitting metal layer. Such enhancement of radiative interfacial heat transport under strong electron-phonon non-equilibrium has potential applications in hot electron transistors [152, 153], thermal switching [154, 155], thermophotovoltaics [29, 124, 156], and nanophotonic devices [125, 126, 157]. This work provides a foundation for designing advanced materials and devices that leverage these radiative mechanisms for efficient energy transduction. The presented results in Fig. 4.3 show that while the photonic energy transfer across solid-state dielectric interfaces is often overlooked when tuning the efficiency of thermal transport, the evanescent flux emitted can become significant in cases of extreme non-equilibrium.

In summary, we investigated evanescent RHT under extreme non-equilibrium in various thin film metals in contact with several dielectric absorbers. Using fluctuational electrodynamics, we predicted interfacial radiative conductance for electron temperatures ranging from 300 to 5000 K. We found that polaritonic substrate supporting surface or hyperbolic phonon polaritons in the

infrared region could achieve radiative conductance comparable to its conductive counterpart. The highest conductance was observed for a tungsten film on hBN at high electron temperature due to hyperbolic phonon polaritons, surpassing 300 MW m^{-2} K^{-1} and rivaling typical phonon-phonon interfacial conductances. The trends observed in radiative TBC suggest that electrons impinging on an insulating interface can emit energy not only via e-p coupling but via the transduction of thermal energy into polaritonic and photonic modes of the absorber, providing an additional pathway for thermal transport and energy transduction at the nanoscale.

Chapter 5

Infrared Phonon Thermoreflectance in Polar Dielectrics

This section focuses on the development of current near field radiation theory to envelop the radiation transported through metal-dielectric interfaces in the presence of non equilibrium electrons. The work presented in this work is being prepared for submission.

5.1 Background

Modulation spectroscopy techniques, such as thermoreflectance, piezoreflectance, and electroreflectance [158], have been fundamental in probing the physics of material systems. In thermal sciences, these methods are employed to measure periodic reflectivity perturbations induced by the absorption of light, forming the foundation of optical pump-probe techniques such as time-domain thermoreflectance (TDTR) [83], frequency-domain thermoreflectance (FDTR) [159] and, more recently, steady-state thermoreflectance (SSTR) [82]. The non-contact and adaptable nature of these techniques has enabled the study of thermal transport across a wide array of material systems, ranging from meso- to nano-scales. These techniques and their derivatives have led to advances in understanding electron-phonon coupling [160, 161], ballistic phonon transport [162], and the thermal management of electronic devices [163]. Optical approaches are also well-suited for in-situ growth characterization and device quality assurance [164, 165]. However, a fundamental aspect of these techniques is the presence of a thin film at the top surface that absorbs optical energy from the pump and serves as a thermometer to characterize the resulting temperature rise with the probe. This "transducer" film is central to the design of thermoreflectance methods.

A thorough understanding of the physical and chemical properties of the transducer, including thermal conductivity, thermal stability, specific heat, adhesion, and dielectric function, is essential

for accurate measurements. Thereby, extensive research has been conducted on the optimal choice of transducer [79, 166–168]. FDTR, TDTR, and SSTR techniques all utilize a metal transducer, which serves two primary functions: efficiently converting an optical excitation into a broadband thermal response and acting as a reflective surface with well-characterized thermoreflectance, enabling the assessment of thermal gradients. Metal transducers have become the standard for this role due to their high thermoreflectance [169, 170] and strong absorption from inter-band transitions in the visible range [170, 171], allowing for effective flux reception. The signal strength in a thermoreflectance technique is therefore directly influenced by the pump beam's absorption at the inter-band transitions, which dictates the thermal amplitude of heating, as well as the magnitude of thermoreflectance, which determines sensitivity to any thermal variations. Since the most commonly used transducers are thin metal films deposited after the growth procedure, thermoreflectance techniques have primarily been limited to post-growth characterization.

Various qualitative assessments have been conducted on metallic transducers by measuring the thermoreflectance coefficient, dR/dT. However, these studies have been limited in both the range of materials examined [79, 172] and the spectral regimes explored [169]. In most applications, restricting transducers to metals is intuitive, as pulsed laser systems typically operate in the visible to near-infrared range, where metals exhibit strong electronic absorption and thermoreflectance. Metals are also advantageous as transducers due to their small optical penetration depth at the pump wavelength, ensuring the heat deposited by the beam is purely absorbed into the surface, simplifying analysis. For decades, the prevalence of laser wavelengths in the visible range of spectra [173, 174] reinforced the use of metal transducers. However, with advancements in optical parametric amplification [175], the spectral range of optical pump-probe techniques has expanded, necessitating a reassessment of optimal transducer materials [146, 176, 177].

While metallic transducers have played a critical role in thermoreflectance measurements, their reliance on inter-band transitions for high thermoreflectance [170] inherently limits their application to specific wavelength ranges. Expanding transducer options beyond metals could unlock new capabilities in thermal metrology, particularly in the mid-infrared regime, where strong phonon resonances in dielectric materials can enhance sensitivity. Dielectrics offer additional flexibility, as their transparency in certain spectral regions enables thermal event transduction at various depths within a multilayer system. By shifting the focus from metallic absorption to optical phonon modes, new

transducer materials can provide improved thermoreflectance performance while offering greater versatility in probing buried interfaces and sub-surface thermal transport.

In this letter, we expand the range of viable transducers into the mid-infrared regime, specifically by leveraging the optical modes present in dielectrics to achieve higher thermoreflectance coefficients for stronger signals and enhanced absorption for more intense thermal events. Using variable-angle spectroscopic ellipsometry, we measure $\Delta R/\Delta T$ for a series of dielectric materials across the mid-infrared range. Our temperature-dependent ellipsometry results provide precise calculations of dn/dT and dk/dT for these materials, allowing for a direct comparison of transducer efficiency. To quantify the effectiveness of materials in pump-probe thermoreflectance measurements, we introduce a transducer figure of merit (FOM) accounting for the absorption of pump energy as well as the intensity of the probe thermoreflectance signal. Notably, we observe that the thermoreflectance of dielectric materials can exceed that of commonly used metal transducers, resulting in an enhanced FOM and demonstrating the potential of dielectrics as superior alternatives for mid-infrared thermoreflectance applications.

5.2 Infrared pump-probe

The principal parameter needed to transduce the optical response of a material to temperature, is the functionality of the material's reflectivity. At a normal incidence, a material's reflectivity is found from the Fresnel equations as

$$R = \frac{(n-1)^2 + k^2}{(n+1)^2 + k^2} \tag{5.1}$$

where the optical constants n and k represent the refractive index and the extension coefficient, respectively. Both n and k can be derived from optical measurements, and are related to the complex dielectric function $\varepsilon = n^2 + ik^2$. The dielectric behavior of polar dielectrics in the infrared region can be modeled by use of standard Lorentzian modes [43] of the dielectric function as

$$\varepsilon(\omega) = \varepsilon_\infty \left(1 + \sum_j \frac{A_j^2}{\omega_j - \omega^2 + i\Gamma_j \omega} \right) \tag{5.2}$$

where A_j, and ω_j are the amplitude and centroid frequency of the j^{th} mode, respectively. The

breadth or dampening associated with each mode is given by Γ_j.

To experimentally determine the magnitude of induced reflectance following a thermal excitation, we employ a standard transient thermoreflectance technique. A 32W Spectra-Physics 1040 nm seed laser is split into two paths. The probe path utilizes an optical parametric amplifier (OPA) to tune the wavelength within the range of 2–16 microns, while the pump path is directed through a second harmonic generation crystal to produce a 520 nm wavelength beam, as shown in Fig. 5.1a. The probe is delayed relative to the pump (via advancing the pump) and guided to the sample surface in an off-angle configuration to minimize the pump bleed-through. The reflected probe is then spatially filtered from the pump and focused onto an MCT detector.

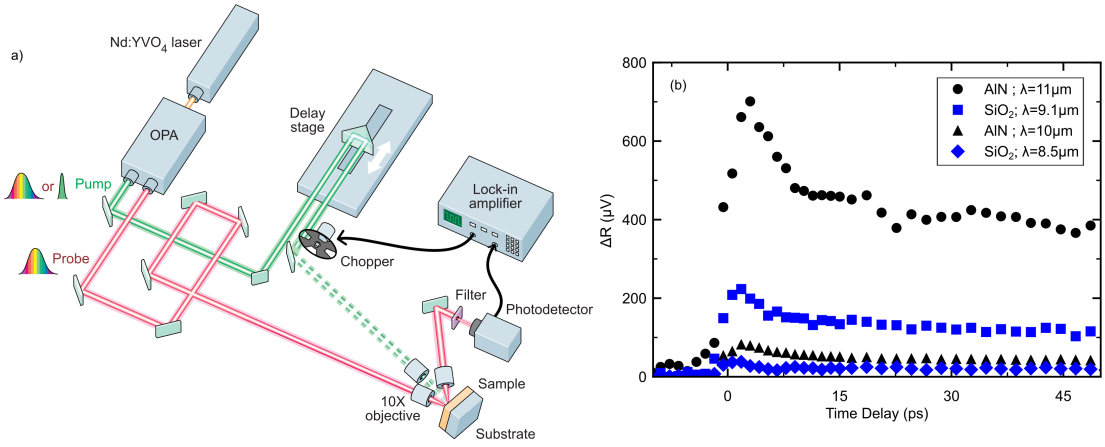

Figure 5.1: (a) Transient thermoreflectance data for dielectric substrates with an optically thin gold transducer. Measurements were performed on AlN and HPFS using a probe wavelength at the peak of thermoreflectance and a visible (520 nm) pump to transduce the optical energy into heat, ensuring identical heating events for direct thermoreflectance comparison. The AlN substrate exhibits overall higher signals due to the stronger relative contributions of its transverse optical phonon oscillators compared to HPFS. (b) Schematic of the transient thermoreflectance system used in the experiments shown in (a).

This configuration is designed to isolate the reflected response of the optical phonons of the substrate. We use a 5 nm gold transducer to create a reproducible heating event, ensuring that the pump energy is uniformly absorbed within the metal film. Since the selected substrates, including high-purity fused silica (HPFS) and aluminum nitride (AlN), are transparent to the pump wavelength, heat deposition is restricted to the surface. Additionally, an optically thin transducer is chosen to ensure that the reflected light contains thermoreflectance contributions from both the metal surface and the underlying substrate. This experimental design allows us to investigate the spectral dependence of the thermoreflectance response of the substrate. By comparing the thermoreflectance response on an optical phonon resonance to the response further away from the same peak, we isolate for the variance in thermal properties of the sample stack. To achieve this, we select probe wavelengths near the center of a known optical mode resonance for maximium signal, and with an identical system de-tune the probe by $\sim 1\mu$m. A direct comparison, such as this, also minimizes the thermoreflectance contribution of the metal transducer as the Drude dielectric function lacks any spectral features in the MIR spectrum. The measured data, shown in Fig. 5.1a, demonstrate that for an identical applied flux, the net thermoreflectance response in AlN at 11 μm is nearly 4 times higher than in HPFS at 9 μm. In both cases, the thermoreflectance response of the gold transducer alone is staggeringly low at the wavelengths, shown in the off resonance data at 10 μm and 8.5 μm. This observation aligns with theoretical predictions, since the major modulated reflectance response in metals in the infrared region primarily arises from free electron contributions, which are relatively weak at the wavelengths measured [171]. As such, the difference between AlN and HPFS signals suggests a $\sim$4-time difference between their thermoreflectances in the mid-infrared region.

5.3 Temperature dependent ellipsometry

With the thermoreflectance of optical phonons experimentally verified, we expand our search for optimal transducer candidates by extracting the thermoreflectance of multiple dielectric materials using spectroscopic ellipsometry. The spectroscopic ellipsometry method measures the change in polarization in light after it interacts with a material surface. The wavelength-dependent complex refractive index of the measured sample can then be extracted. The measured sample set in this

study includes HPFS, AlN, quartz, sapphire, gallium nitride (GaN), silicon carbide (SiC), and magnesium oxide (MgO). We perform measurements in the wavelength range of 2-30 μm using a J.A. Woollam IR-VASE. When determining the temperature dependence of each optical parameter, we integrate a Linkam TSEL1000 heater stage into the IR-VASE system. To maintain consistency with previously reported thermoreflectance measurements [169], each sample is measured at 300 K and 500 K.

It is evident from Eq. 5.1 that the refractive index plays a crucial role in defining optical behavior, leading to significant variations in transparency and reflectivity across different substrates. This transparency region can be leveraged in experiment design, allowing the probe in a thermoreflectance technique to penetrate the surface and observe thermal transport at deeper interfaces. Conversely, selecting an opaque region enables the technique to mimic conventional metallic transducer-based thermoreflectance methods. This flexibility underscores the importance of a detailed characterization of the complex refractive index, which is provided for each material in Section A of the Supplementary Materials. For an opaque transducer configuration, determining the exact absorption mechanism requires careful consideration.

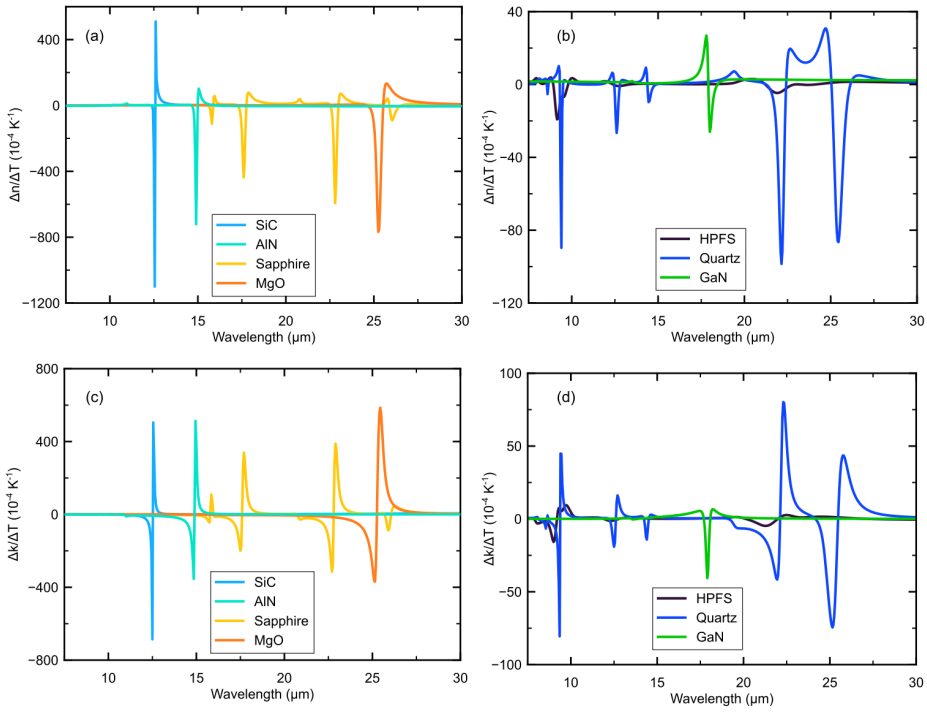

Figure 5.2: Calculated temperature dependence of the (a,b) refractive index and (c,d) extinction coefficient for SiC, AlN, sapphire, MgO, HPFS, Quartz, and GaN.

We present the measured values for the temperature dependence of refractive index and extinction coefficient, i.e., $\Delta n/\Delta T$ and $\Delta k/\Delta T$, for our dielectric sample set in Fig. 5.2. A key observation from these measurements is the rapid variation in $\Delta n/\Delta T$ and $\Delta k/\Delta T$ near TO phonon wavelengths, which occurs due to temperature-induced shifts and broadenings of optical phonon resonances. At elevated temperatures, the TO phonon modes redshift due to anharmonic effects, altering the refractive index profile. Simultaneously, phonon scattering rates increase, leading to broadened absorption features and enhanced damping effects. These changes collectively result in a strong temperature-dependent modulation of the optical properties, making spectral regions near TO phonon resonances highly sensitive for thermoreflectance-based thermometry. Additionally, changes in n and k with temperature are minimal for spectral regions above $\sim$15 μm, due to the diminished influence of optical phonon resonances at far-infrared wavelengths. In contrast to the strong dispersive effects near TO phonon frequencies, the refractive index at longer wavelengths is primarily governed by the low-frequency dielectric response, which is relatively stable with temperature. As a result, materials in this range exhibit weak optical perturbations, leading to smaller reflectivity variations under thermal excitation.

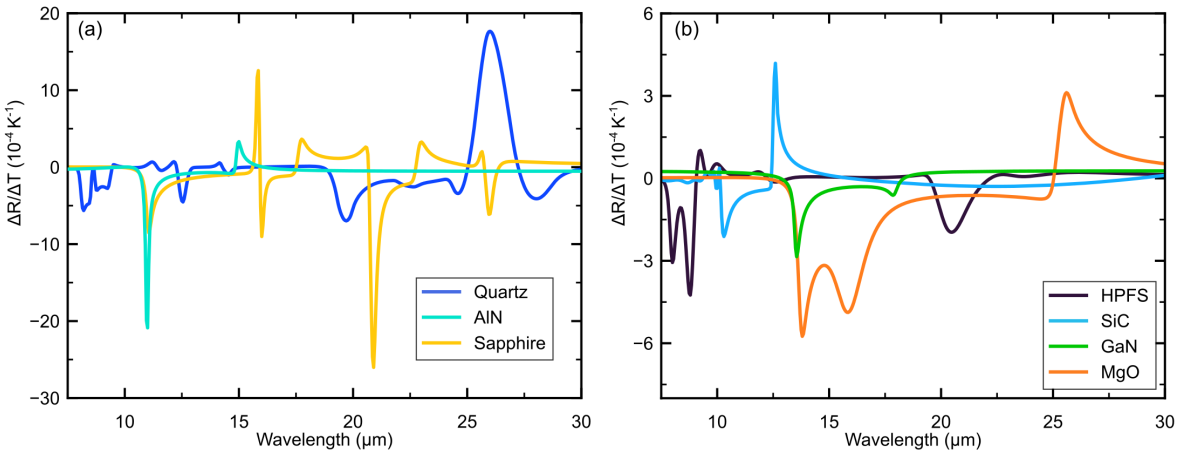

Figure 5.3: Thermoreflectance coefficients extracted from infrared spectroscopic ellipsometry for (a) quartz, AlN, sapphire, and (b) HPFS, SiC, GaN, MgO.

The computed thermoreflectance coefficient ($\Delta R/\Delta T$) for the tested dielectrics is calculated from the complex refractive indices at different temperatures, as presented in Fig. 5.3. Our results indicate that thermoreflectance is highly sensitive to optical phonon resonances, with the largest $\Delta R/\Delta T$ values occurring near TO phonon frequencies. As shown in Fig. 5.3, the tested polar dielectric samples exhibit pronounced thermoreflectance peaks, where strong phonon absorption modulates both the refractive index and extinction coefficient.

These results confirm that phonon-driven modulations dominate thermoreflectance in these dielectrics. The high sensitivity of the refractive index to temperature fluctuations results in a large thermoreflectance coefficient. This effect arises from both the steep dispersion of the refractive index and the rapid modulation of optical absorption, which directly influences reflectivity. Therefore, wavelengths close to TO phonon modes exhibit enhanced thermoreflectance sensitivity, making them optimal for high-precision thermometry. As the material becomes optically transparent or weakly absorbing, dn/dT and dk/dT are relatively small, leading to a lower thermoreflectance response. In this regime, reflectivity changes primarily depend on background dielectric behavior, which varies weakly with temperature. This observation extends to all materials in the test set, reinforcing the importance of selecting appropriate spectral regions when designing thermoreflectance experiments. By choosing probe wavelengths that align with TO phonon resonances, one can maximize the thermoreflectance coefficient, thereby improving the signal-to-noise ratio and enhancing sensitivity in thermal characterization techniques. At these peak wavelengths, $\Delta R/\Delta T$ for these dielectrics in the mid-infrared range surpass that for commonly used metallic transducers [169]. Specifically, the thermoreflectance coefficient of sapphire, quartz, and AlN exceed the highest values reported for metallic transducers by about an order of magnitude, reaching peak $|\Delta R|/\Delta T$ values of 2.6×10^{-3}, 1.7×10^{-3}, and 2.1×10^{-3} near their corresponding TO phonon wavelengths of $\sim$21, $\sim$26, and $\sim$11 μm, respectively. In comparison, The metal transducers reported in Ref. [169] have FOMs which never exceed 1.1×10^{-4}. This highlights the superior sensitivity for thermal measurements shown in polar dielectrics. Moreover, unlike metals, which rely on inter-band electronic transitions for reflectivity modulation, dielectrics allow precise selection of probe wavelengths to maximize thermoreflectance based on phonon dispersion. The narrow, resonance-driven thermoreflectance peaks in dielectrics enable targeted thermal sensing applications, whereas metals exhibit broader, less selective responses.

While our results demonstrate that thermoreflectance is maximized near TO phonon resonances, the overall effectiveness of a transducer is not solely determined by the magnitude of $\Delta R/\Delta T$ at the probe wavelength. For a transducer to efficiently generate a detectable signal, it must also exhibit strong absorption at the pump wavelength, ensuring sufficient optical-to-thermal energy conversion. Thus, the optimization of transducer performance requires a combined evaluation of both thermoreflectance sensitivity and pump light absorption. To systematically quantify this trade-off, we introduce a figure of merit (FOM) that integrates both factors, providing a comprehensive metric for assessing transducer efficiency across different materials and spectral regions. This FOM is expressed as:

$$FOM = k(\lambda_{pump}) * \frac{\Delta R}{\Delta T}(\lambda_{probe}) \tag{5.3}$$

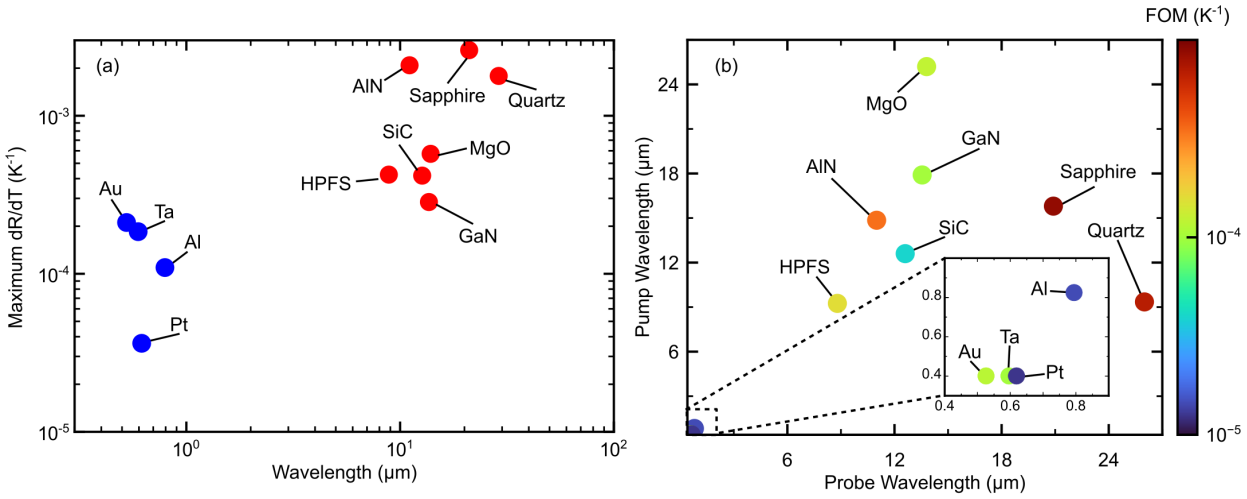

Figure 5.4: Computed maxima of (a) the thermoreflectance coefficient and (b) the figure of merit (FOM). The maximum values obtained for polar dielectrics in this work are compared with those reported for metal transducers measured by Wilson et al. [169]. The color axis in panel (b) Indicates the maximum FOM magnitude achieved by each material system, evaluated at the pump and probe wavelengths corresponding to that maximum.

This formulation ensures that maximizing the FOM leads to both large temperature rises within the transducer and strong thermoreflectance signals, optimizing the overall sensitivity of the measurement. In standard thermoreflectance experiments, the choice of pump and probe wavelengths has been optimized for metallic transducers [169] to maximize the signal-to-noise ratio. Following this approach, we summarize our findings in Fig. 5.4, where we plot the maximum FOM, and thermoreflectance for each prospective transducer studied in this work and in Ref. [169]. The FOMs

are plotted alongside their corresponding pump and probe wavelengths at which these maxima occur. A complete contour map of the FOM for each material is provided in Section B of the Supplemental Materials. As shown in Fig. 5.4, the polar dielectric substrates analyzed in this study exhibit higher FOM values than commonly used metallic transducers. Specifically, the maximum FOM values for polar dielectrics are up to two orders of magnitude higher than those of metallic transducers, with sapphire and AlN reaching maximum FOMs of 0.05 and 0.04, respectively, as compared to 1.1×10^{-4} shown in Au. In metallic transducers, thermoreflectance is primarily driven by absorption due to inter-band transitions, which occur predominantly in the visible to near-infrared range. Consequently, the highest FOM values for metals are confined to these shorter wavelengths, where optical absorption is strongest. In contrast, polar dielectrics exhibit their largest FOM values in the mid-to-far infrared, where optical phonon resonances dominate absorption. These phonon-driven mechanisms lead to strong temperature-dependent modulations of the refractive index and extinction coefficient, significantly enhancing thermoreflectance sensitivity at infrared wavelengths. The enhanced FOM of dielectrics opens the possibility of designing spectrally selective thermoreflectance transducers, where specific probe wavelengths can be chosen to target different functional layers within a device stack. This capability is particularly valuable for next-generation semiconductor technologies, where high spatial and spectral resolution thermal mapping is critical for optimizing device performance and reliability.

5.4 Conclusions

To summarize, we investigate the potential of dielectric materials as effective alternatives to traditional metallic transducers for thermoreflectance-based temperature transduction, particularly in the mid-infrared spectrum. Using infrared spectroscopic ellipsometry, we show that, by capitalizing on optical phonon resonances, dielectric transducers can achieve thermoreflectance coefficients that are up to an order of magnitude higher than the widely used metal transducers, showcasing their ability to detect thermal variations. We introduce a new figure of merit that allows for a comprehensive assessment of transducer efficiency, integrating both thermoreflectance response and pump light absorption. Our measurements demonstrate that dielectric materials such as sapphire and AlN exhibit up to two orders of magnitude improvement over conventional metal transducers in FOM,

with the highest recorded value being 0.05 K^{-1} for sapphire (over two orders of magnitude larger than Al and Au, current metal transducers at visible wavelengths), which confirms their exceptional potential for high-precision thermal detection. The capability to fine-tune probe wavelengths to match phonon dispersion properties opens new possibilities for refined thermal metrology, facilitating more accurate and targeted measurements in semiconductor diagnostics and in-situ material assessments.

Chapter 6

Demonstration of the thermal excitation of polaritons

This section focuses on the experimental observation of near field radiative coupling via an enhancement of flux across the interface of Au and hBN.The experiments and optical simulations were performed by myself, whereas the construction and growth of the measured samples were completed by the groups of Joshua Caldwell and James Edgar, respectively. The work presented in this section has been published in *Nature Materials* [146].

6.1 Background and Motivation

Boron nitride has been revered in the literature in the fields of optics and heat transport due to its dielectric properties [178] and high thermal conductivity [47, 179, 180]. Specifically, the highly anisotropic hexagonal boron nitride (h-BN), supports thermal transport properties higher than most metals in-plane while being quite resistive through its depth. This opens the door for strong control of thermal energy leading to a multitude of engineering possibilities. At the same time, because of the structural ansiotropy, the allowed optical propagation within h-BN are highly confined and support strong HPhP resonances with the lattice [148]. With their high confinement, there has been many works highlighting the possible uses in optics such as sub-diffractional imaging [181], wave-guiding [182] and focusing [183]. However, due to generally low group velocities, optical modes are not typically thought to contribute considerably to the thermal conduction [184] within the lattice and instead serve as scattering sites for acoustic vibrations [185]. There has been considerable work on understanding the thermal conduction of PhPs [186, 187], that is optical phonons which have been accelerated by strong coupling with light. The work in literature focuses on understanding the PhPs as fast polaritons. In the completed work below, which is published in *Nature Materials*

[146], we combine the conductive and radiative approaches to give a more holistic picture. The work detailed in this chapter represents a collaboration between Joshua Caldwell's group, who provided the exfoliated and patterned flakes, grown by James Edgar, and my contributions were the measurments and simulations presented which describe observed mechanisim.

6.2 Motivation

Across nearly all heterogeneous dielectric interfaces, heat is dissipated via conductive processes driven by acoustic phonons, or other vibrational interactions, which limit thermal boundary conductance [69, 113, 188]. Bose-Einstein statistics of nearly thermalized phononic distributions dictate that the typical vibrational energies that contribute to heat transfer across and away from interfaces are lower-energy, higher-group-velocity acoustic phonons, which, at room temperature, are on the order of a few to 10 THz. Due to their larger heat capacities [189], optical phonon branches play an important role in mediating thermal transport [190]. However, the intrinsically slow group velocities [191] restrict these modes' abilities to spread heat away from interfaces and hot spots, thereby putting the burden of thermal dissipation back on the acoustic modes.

In this work, we examine an alternative mechanism to transfer energy across and away from all-solid heterogeneous interfaces by harnessing the local evanescent fields resulting from a hot radiating source to directly launch volume-confined, hyperbolic phonon polaritons (HPhPs) within the frequency range bound by the transverse (TO) and longitudinal (LO) optical phonons of a polar crystalline material, which is referred to as the Reststrahlen band. Hyperbolic polaritons are supported within spectral ranges where a material or structure exhibits dielectric permittivity that are opposite in sign along different crystal axes [192]. Originally explored in metal/dielectric superlattices in the form of hyperbolic metamaterials, HPhPs have been of significant research interest as they can be supported in a homogeneous, low-loss film, with hexagonal boron nitride (hBN) serving as an exemplary material in this regard [193–195]. Isotopic enrichment can also be leveraged to tune the Reststrahlen band and significantly increase the phonon lifetimes (and thus, polariton propagation lengths) of hBN and therefore tune the efficiency of the coupling mechanism [148, 194, 196], which here was employed to provide optimal propagation lengths. More recently, it has been demonstrated that natural, low-symmetry (highly anisotropic) crystals such as orthorhombic

MoO_3 [197, 198] and V_2O_5 [199], and monoclinic crystals such as $\beta-Ga_2O_3$ [200] and $CdWO_4$ [201] can support HPhPs that can be restricted to propagate along a specific direction in space, with the latter two supporting so-called hyperbolic shear polaritons that are not only highly directional, but also exhibit a propagation direction that is frequency-dependent. As such, if these modes can be induced to carry heat, similar studies could also be widely applied to other hyperbolic materials along specific crystallographic directions via optimal material selection. Specifically, MoO_3 [198] and twisted metastructures [202] also support highly directional confined HPhP modes, and heating of such modes would allow for directional thermal mitigation of hot spots across interfaces.

While optical phonons typically cannot be used to efficiently conduct heat away from interfaces due to their slow group velocities, this seemingly insurmountable intrinsic material limitation can be overcome by transducing the broadband radiative thermal energy from a thin metal film in the near field into the HPhPs supported within the underlying anisotropic medium, passing this energy across the heterogeneous interface. Previously, HPhPs in hBN have been demonstrated to have propagation lengths of several micrometers, [202, 203] enabling applications such as hyperlensing [181, 204, 205] and chemical sensing, to enhance thermal transport beyond phonon-limited processes, [147] and a Reststrahlen band that can exhibit reasonable emission even at near room temperatures. [206] Literature has even suggested that this process can occur at interfaces between 2D van der Waal materials, [119, 207, 208] warranting the study of this process at 3D contacts, a direct experimental measurement of which would demonstrate the broad applicability of this unique heat transfer process. Through exploiting time-resolved infrared pump-probe measurements, we directly measure the picosecond cooling of indirectly heated optical modes [209, 210] in a nearly isotopically pure hexagonal boron nitride ($h^{11}BN$; $> 99\%$) flake after the optical pumping of an adjacent gold contact, thereby demonstrating a mechanism for interfacial cooling that is orders of magnitude faster than typical phonon-mediated processes. Previous works have demonstrated fast, efficient near field radiative heat transfer (NFRHT) across narrow vacuum gaps between metallic and dielectric plates, [206] but this approach relies on the inclusion of a nm-scale vacuum gap, thus limiting its utility in certain practices. Our work proves that thermal boundary conductance across heterogeneous interfaces and thermal dissipation in a material away from interfaces can be significantly enhanced through the coupling of a broadband radiating hot spot into propagating PhPs, a finding that surpasses intrinsic material limitations of thermal coupling at interfaces. In doing

so, we establish a new paradigm for interfacial thermal transport that moves beyond the nearly century-old concepts and theories of phonon coupling at dielectric interfaces originally discovered by Kapitza. [211]

Enhanced thermal dissipation in solids via polaritonic heat transfer has been theoretically predicted [186] and the prospect of enhanced speeds and even directional control of heat transfer is enabled by the exotic properties of PhPs, such as long propagation lengths, [202, 203] anisotropic and nonuniform control of their propagation [200, 212–214] and speeds that approach percent levels of the speed of light. [215–218] Experimental works have shown the ability of HPhPs to enhance thermal conductance in dielectrics, [147, 219]. However, experimental evidence differentiating the coupled PhP modes from the thermalized phonon modes intrinsic to the material is still lacking. Thus, the first major finding of our work is the ability to both spectrally and temporally resolve the thermally excited HPhP modes in hBN, providing clear evidence of the more efficient thermal transport that these hot HPhP carriers can provide.

Secondly, our results illustrate that HPhP thermal coupling can occur across an all-solid heterogenous interface, and further, that the HPhP modes do not need to be coherently excited, but rather can be optically stimulated by a graybody radiating in the near field. The latter observation is consistent with Ref. [32] where thermal radiation from a heated SiC diffraction grating resulted in the excitation of propagating SPhPs, which once stimulated were outcoupled via diffraction, giving rise to spatially coherent IR radiation. It is well known that polaritonic modes can enhance heat transfer via NFRHT processes between two radiating bodies separated by a vacuum gap that is less than the Wien wavelength. [220–225] Our work unlocks the possibility of utilizing this NFRHT enhancement at solid-solid interfaces in intimate atomistic contact, by showing that this broadband radiative cooling effect is driven by PhP coupling that can delocalize the thermal energy from a radiating spot into an adjacent hyperbolic medium. This finding will redefine cooling of hot spots in materials and systems limited or dictated by interfacial resistances, such as high power or high frequency electronics, [226] photonic circuits, [163] memory, [227] and thermophotovoltaics. [228]

6.3 Pump-Probe Measurements

Our sample geometry is designed to provide a direct observation of spectrally dependent radiative thermal coupling from a thermally excited source (50-nm Au pad) into HPhPs supported in $h^{11}BN$, referred to hence forth at hBN (Fig. 6.1a). In our pump-probe experiments, we excite the Au pad (Fig. 6.1b) with a 520-nm pump pulse (incident fluence of 0.3 GW m^{-2}) and a 200-μm $1/e^2$ diameter probe pulse centered on the Au pad. The central Au pad acts as the focal point of our experiment. We first overlap our pump and probe on the Si substrate. Then, we alter the position of the sample such that the green pump is focused on the circular pad. The rectangular pads serve as reflectors for the polaritons. This configuration creates standing polaritons, similar to Ref. [202] in the space spanned by the probing region, which should increase our pump-probe signal. The different distances were used in order to be agnostic to the mean free paths of different HPhP modes. The thermoreflectance changes, measured by the reflected probe pulses from the hBN as a function of time after pump absorption by the Au, are monitored as a function of probe wavelength, which are tuned from below to above the Reststrahlen band of hBN ($\approx$ 1355 – 1610 cm^{-1}). [148] Immediately following the pump absorption on the surface of the Au, the Au pad is rapidly volumetrically thermalized via ballistic electron transport, [144] which despite the low thermal emissivity of metals within the mid-IR will radiate efficiently in the near field due to the large imaginary contribution to the Au dielectric permittivity or optical loss. Such near-field radiation is composed of high-momentum, evanescent fields that can directly match the momenta of the HPhPs within the hBN slab. This coupling mechanism is present through the entire area of the Au/hBN interface, a mechanism that our experiment is designed to detect with our tunable IR probe energies. The enhanced coupling between the optical modes and the radiation underneath the pad give rise to large thermoreflectance optical signals within the Reststrahlen band and at the TO phonon frequency of hBN, as shown in the contour plots of the thermoreflectance spectra vs. Pump-probe delay time in Fig. 6.1c. In contrast, in the absence of the Au pad, we do not observe any such increase in thermoreflectance signal, as the hBN is transparent to the pump wavelength. This large spectral dependence on our thermoreflectance signal clearly illustrates that the underlying Si substrate is not playing any significant role, as even though it will absorb the pump photons, it does not induce a significant transient spectral response, further demonstrated

by supplemental spectral measurements on identical Si substrates (see Fig.S5 in Supplementary Information of Ref. [146]).

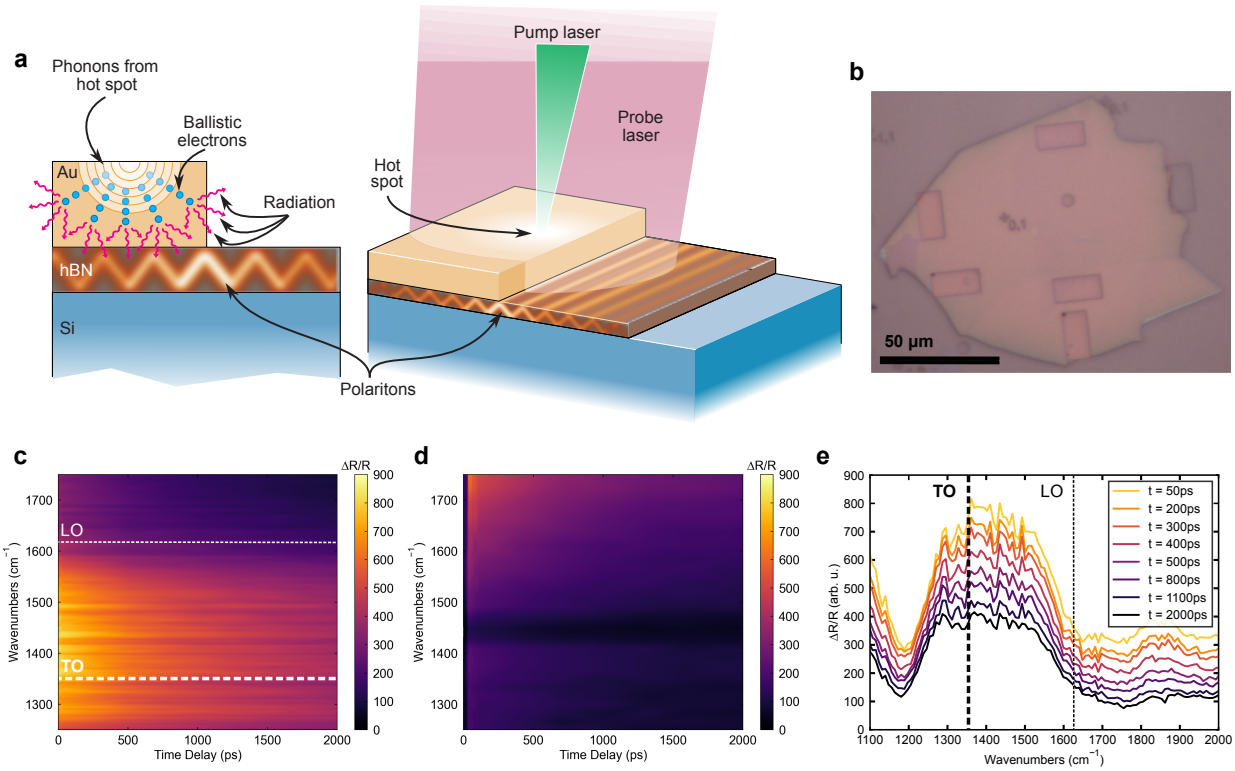

Figure 6.1: **Experimental details and spectral-temporal response of HPhP modes in hBN**. a) Illustration of the proposed mechanism and experimental measurement. A pump pulse (520 nm) heats a gold pad, while a sub-picosecond tunable mid-IR probe pulse measures the modulated reflectivity response of the hBN patterned flake. After pulse absorption in the Au, both phonons and ballistic electrons spread from the hot spot in the Au, depicted by the small blue particles and the background waves emanating from the hot spot. Radiation from the hot electrons (the red arrows) escapes and couples into the HPhP modes of hBN (pump and probe spot sizes not to scale). b) The sample geometry the reliefs in the image show the position of Au excitation pads used for both s-SNOM characterization (see Methods), as well as thermal HPhP launching. c) The measured thermoreflectance signal of the 116-nm hBN flake as a function of probe energy and pump-probe delay time for an incident pump fluence of 95.5 J m^{-2}. The strong ΔR/R response within the Reststrahlen band (indicated by the span of the dotted lines) and near the TO phonon frequency of hBN shows the high thermal activity within the region that can be attributed to ultrafast heating from near-field radiation emitted by the Au-pad. d) For reference, a similar pump fluence of an uncoated (no Au) hBN flake is provided, noting that in this case, no temporal thermoreflectance response is observed within the range of the hBN Reststrahlen band, illustrating the critical role of the Au pad as a thermal transducer in this experiment. The dark band that appears in the middle of the blank hBN contour is attributed to PMMA residue, a photo-resistive polymer in the lithographic patterning process. e) Waterfall plots of the data shown in c) at a variety of pump-probe time delays (80-2030ps) following transient Au heating, indicating more clearly the ultrafast optical response surrounding the TO phonon mode and within the hBN Reststrahlen band (indicated by the span of the dotted lines).

The observation of a strong thermoreflectance signal within the Reststrahlen band at picosecond timescales indicates the role that HPhPs play in this thermal dissipation process. As evidence of this, when we tune our probe energy to frequencies above the Reststrahlen band of hBN following the pumping of the adjacent gold pad, we see minimal temporal changes in the probe thermoreflectance signal (Fig. 6.1c, e; see dashed vertical lines to designate the TO phonon mode and the surrounding active region). However, as the probe energy is tuned to energies within the Reststrahlen band, the thermoreflectance signal exhibits large increases in the thermoreflectance that is maximized at the earliest times, indicative of large optical phonon temperature changes [229] (with an additional peak at the TO phonon energy – dark vertical dashed line in Fig. 6.1e). This significant increase in thermoreflectance drops off at frequencies below the TO phonon, with the broadening below this band potentially due to the deeply subwavelength modes that can also be stimulated in hBN due to the exceptionally high refractive index within this spectral range, as previously discussed for Mie resonators in 4H-SiC nanopillars. [230] The hBN dielectric function does not vary with thickness in this spectral region [178, 231] To support this posit, similar observations were performed measurements on hBN flakes with varying thicknesses ranging between 89 nm and 195 nm, an example of which is presented in Fig.S6 of the Supplementary Information of Ref. [146]; as expected, no size effects are observed.

The sample was constructed such that only $\approx 6\%$ of the probed region is covered with gold (see Fig. 6.1b), effectively diminishing any effect that it might have on the measured thermoreflectance. Yet, we observe a spectrally local thermal event occurring in the Reststrahlen band of hBN. Our lock-in detection scheme isolates any optical effects of the probe. Further, the polaritonic modes in the hBN cannot be directly launched due to the lack of a momentum matching condition from the 520 nm pump. Due to the long time constant of phonon conduction (1000's of ps) compared to the decay time of our observed modal heating, we posit that the Au-to-hBN interfacial heat transfer mechanism is driven by evanescent pumping of the hyperbolic modes in the hBN flake from the radiating Au pad. This mechanism is mediated by the excited carriers in the Au pad. Due to the short timescale of our observed modal heating (10's of ps), we assert that these carriers are the ballistic electrons in the Au that release their heat radiatively at the Au-hBN interface, initiating the ΔT required for radiative transfer.

To further explore the role of HPhPs in the ultrafast interfacial thermal transport between

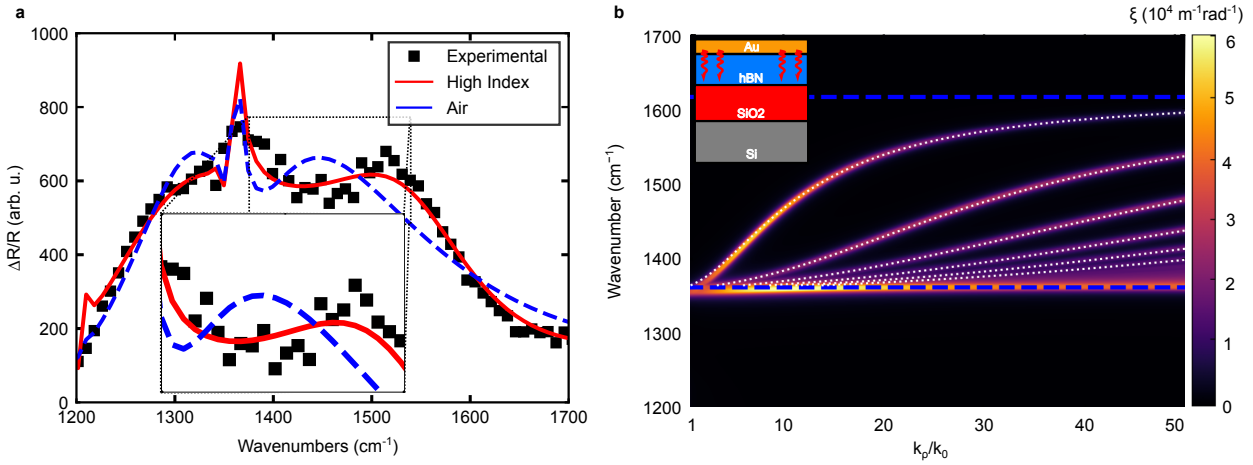

Figure 6.2: **Spectral response of hBN after heating from radiating Au pad**. a) spectral cross sections from the contour of the 116-nm flake (Fig. 6.1e), fitted with and without a polaritonic coupling layer for pump-probe delay time of 45 ps. The spectral-temporal range is representative of the entirety of the activity surrounding the TO phonon mode and shows the improvement of the "Polaritonic" model compared to the standard ambient model ("Air"). The inset plot highlights the advantage of using the high-index layer for momentum matching in the TMM calculation. This "high-index layer" is a better analog to the near-field radiation from the central gold pad effectively increasing sensitivity to the TO phonon band and the polaritons therein. b) Calculated spectral heat flux per unit wavevector between Au and hBN layers in contact. The inset is a schematic of the simulated stack. The white dotted lines show the dispersion relation of HPhPs in hBN, and the blue horizontal lines show the upper and lower limits of the hBN Reststrahlen band. The fluctuational electrodynamics (FED) derived contour directly shows the majority of radiative heat flux across the interface is dominated by modes at the same momentum as HPhPs and thus satisfying our proposed launching condition. This plot begins at a normalized wave vector of 1 which means that all representative momenta are considered in the evanescent regime.

Au and hBN discussed above, we examine the thermoreflectance changes as a function of probe energy measured at short (45 ps, Fig. 6.2a) pump-probe delay times. We employ the transfer matrix method (TMM, [108] details in Section B of the Supplemental Information of Ref. [146]) to simulate the thermoreflectance spectra in the vicinity of the Reststrahlen band using two models. First, we simulate this differential reflectance spectra by employing a plane wave excitation ("Air"), which lacks the high-momenta modes sufficient to launch HPhPs in hBN (Fig. 6.2a, dashed blue line). In contrast, we also perform these TMM calculations using a fictional high-index prism to increase the momentum of optical modes to enable the direct launching of HPhPs (Fig. 6.2a, red line) [232]. This bending of the light line is effectively a simulation of the reflectivity from an attenuated total reflection (ATR) module of an FTIR system which has been experimentally shown to launch polaritons [233–235]. This simulation is therefore an approximation of the reflectivity of a system

while there are active polaritons in the system. A full list of fitted parameter perturbations is available in Section B of the Supplementary Information of Ref. [146] of Ref. [146]. While no prism is employed in the experiments, this is employed as a simple method for simulating the role of the dramatically increased momenta of light, akin to using local dipole coupling to illustrate the role of polaritonic modes within this process. Note that this polaritonic-driven model provides a significant improvement in the fit as compared to the same model without the momentum-matching conditions ("Air"), providing further evidence for the role that HPhPs play in this thermal dissipation process. This effect is significantly muted at longer timescales, whereby other thermal dissipation processes such as phonon-mediated conduction across the Au/hBN interface begin to dominate (See Section B of Supplementary Information of Ref. [146]).

Radiative transport calculation To determine the exact radiative conditions at the Au-hBN interface explored in Fig. 6.2b, we explored the distribution of the spectral radiative heat flux over different momenta. Using the framework of FED [236], the radiative heat flux between the Au pad and hBN slab can be calculated as:

$$q''_{\omega} = \frac{\theta(\omega, T_{\mathrm{Au}}) - \theta(\omega, T_{\mathrm{hBN}})}{4\pi^2} \sum_{\gamma=\mathrm{TE,TM}} \left(\int_0^{\pi/a} k_\rho \xi^\gamma(k_\rho, \omega) dk_\rho \right) \tag{6.1}$$

where k_ρ is the parallel component of wavevector, θ is the mean energy of an electromagnetic state, a is the lattice constant of hBN, and $\mathrm{T_{Au}}$ and $\mathrm{T_{hBN}}$ are the temperatures of Au and hBN layers, respectively. Also, ξ^γ is the energy transfer function, representing spectral radiative heat flux per unit k_ρ, between gold and hBN for γ (TE or TM) polarization. Assuming one-dimensional (that is infinitely long) layered media, the energy transfer function is numerically calculated using scattering matrix method and dyadic green's functions [66]. The contour in Fig. 6.2b shows the energy transfer function between the gold and hBN layers. The white dotted lines in Fig. 6.2b also exhibits the dispersion relation of the HPhPs in hBN, found from the following equation [195]:

$$k_\rho = \mathrm{Re}\left\{ \frac{-\psi}{d} \left[\tan^{-1}\left(\frac{\varepsilon_{\mathrm{Au}}}{\varepsilon_\perp \psi} \right) + \tan^{-1}\left(\frac{\varepsilon_{\mathrm{SiO_2}}}{\varepsilon_\perp \psi} \right) + \pi l \right] \right\} \tag{6.2}$$

where,

$$\psi = \frac{\sqrt{\varepsilon_{||}}}{i\sqrt{\varepsilon_\perp}} \tag{6.3}$$

Also, $\varepsilon_{\mathrm{Au}}$ and $\varepsilon_{\mathrm{SiO_2}}$ respectively represent the dielectric functions of gold and silica, $\varepsilon_{||}$ and $\varepsilon_{\perp}$ are respectively the parallel and perpendicular dielectric functions of hBN, and l is an integer number corresponding to the order of the HPhP modes. Fig. 6.2b shows that the radiative heat emitted by gold is predominantly received by HPhPs in hBN as the heat flux mostly occurs at wavevectors that precisely match the dispersion of HPhPs. As such, the radiative heat flux at any temperature differential between gold and hBN will be carried predominantly through HPhPs.

Beyond the spectral response, it is also critical to quantitatively analyze the temporal relaxation of the thermoreflectance signals within and outside of the Reststrahlen band to delineate the role that HPhPs play in this process. The stark contrast between the time-dependent thermoreflectance signals under these two distinct conditions are provided as a function of pump-probe delay at a probe energy approximately "on resonance" (Fig. 6.3a, black squares) with the TO phonon (probe energy of 7.4 μm = 0.17 eV = 1351 cm^{-1}) compared to the signal with a probe energy "off resonance" (Fig. 6.3a, pink triangles), which is spectrally separated from the Reststrahlen band of hBN (probe energy of 6 μm = 0.21 eV = 1667 cm^{-1}), where hBN is nominally transparent to the probe beam (Fig.S3 in Supplementary Information of Ref. [146]). Additionally, at these photon energies, the thermoreflectance changes in Au provide nearly an order of magnitude smaller thermoreflectance signal compared to that measured from the hBN within the Reststrahlen band, thereby precluding any significant transient response from Au in driving the observed response. Thus, as the large bandgap of hBN (5.95 eV) precludes direct absorption of the incident pump energy (2.38 eV), the measured thermoreflectance signal is instead driven by the changes in the temperature of the hBN that are the result of thermal transport from the heated gold across the interface. The dominant signatures at picosecond timescales occur within the Reststrahlen band of hBN, illustrating the strong correlation of these excitations with thermal transport mediated by optical phonons and HPhPs. Further, our control measurement of pumping and probing directly on the hBN in the absence of Au results in a negligible response (Fig.S4 in Supplementary Information of Ref. [146]), clearly indicating that the measured signal (Fig. 6.33a) is due to a remote heating effect initiated via pump absorption within the Au pad. Thus, the correlation between the ultrafast heating of Au with the dramatic changes in the hBN thermoreflectance within the Reststrahlen band at ps timescales clearly illustrates that the mechanism is mediated through the launching of HPhPs via near-field thermal radiation from the heated gold pads. Our results therefore qualitatively suggest

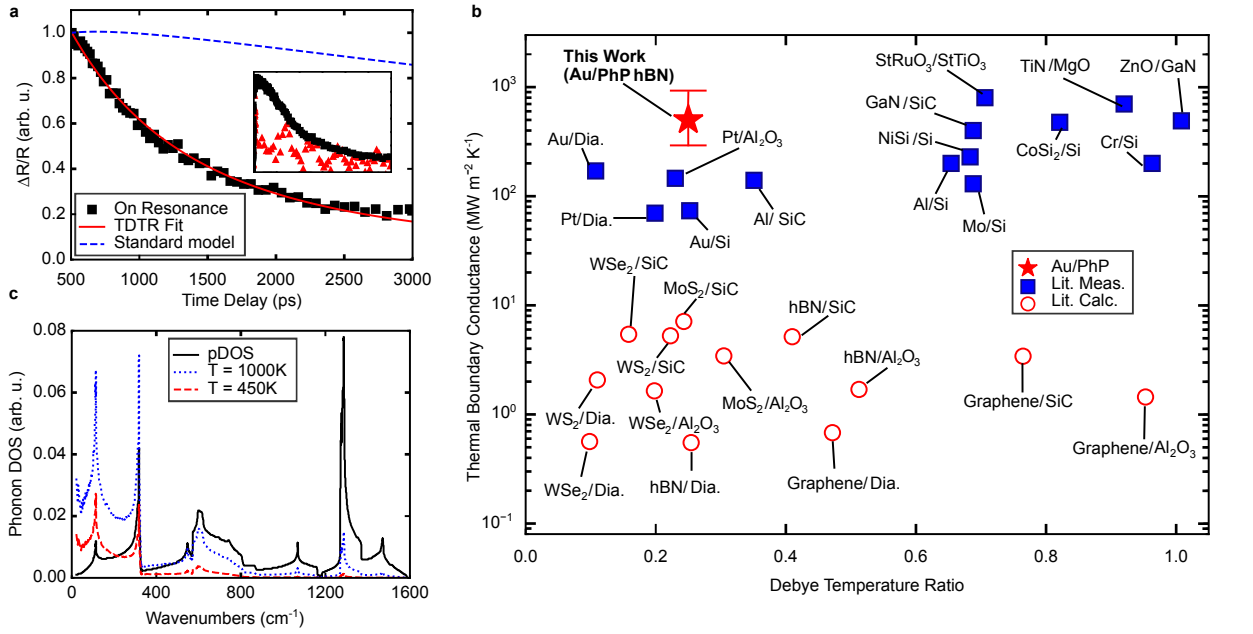

Figure 6.3: **Results from thermal analysis of IR Thermoreflectance**. a) Thermoreflectivity response of hBN as a function of pump-probe delay time after Au pad heating near the TO resonant frequency (black squares, 7.4 μm) of hBN alongside the analytical model fit to the on-resonance data (red solid line). The best fit for the on-resonance data shown resulted in a HPhP-mediated thermal boundary conductance of >500 MW m^{-2} K^{-1}. The standard model (blue dashed line) shows the calculated thermoreflectance signal expected at the surface of the Au pads assuming literature thermal parameters as well as a Au/hBN phonon-phonon thermal boundary conductance of 12.5 MW m^{-2} K^{-1} measured with TDTR (see section D Supplementary Information of Ref. [146] for details) the inset shows a comparison of the raw signal magnitude on resonance (black squares, 7.4 μm) to off resonance (red triangles, 6 μm). The inset represents the difference in magnitude and curvature between the off-resonance and on-resonance data past time zero, highlighting the strong response from the hBN when compared to the Si substrate as well as the extended duration that the hBN remains heated for; b) The current state of experimentally measured bulk thermal boundary conductances across 3D/3D material interfaces (filled blue squares) [113] as well as predicted 2D/3D interface conductances (open red circles region) [237] as well as the best fit Au/hBN HPhP thermal boundary conductance measured in this work with error bars derived from ±5% contour uncertainty presented in figure S9 of the Supplementary Information of Ref. [146], all plotted against film to substrate ratio of Debye temperatures. c) The phonon density of states for hBN was reproduced from a figure in ref. [196] using Density Functional Theory (DFT) plotted with the occupied density of states the at two temperatures showing the lack of activity in the TO phonon mode 150 K above the ambient temperature, implying that the measurements in this work are due to optical phonon activity measured via IR probing, and not from thermally excited phonon modes from conduction alone.

that the Au/hBN thermal boundary conductance (TBC) can be significantly influenced by energy transfer across the Au/hBN interface at ultrafast time scales (sub-nanosecond) mediated by HPhPs.

6.4 Determination of polaritonic conductance rate

The data on resonance with the hBN Reststrahlen band shown in Fig. 6.3a exhibits an exponential decay with a time constant of ≈ 1300 ps. After laser pulse absorption of the gold and the resultant electron-phonon equilibration and thermalization, the majority of the temporal thermal decay is driven by the discharge of energy from the thermalized Au pads into near-field thermal radiation and direct launching of the HPhPs in the hBN. The thermal boundary conductance across the Au/hBN interface from this process can be approximated by $C_v\ d\tau^{-1} \approx 100$ MW m^{-2}K^{-1}, where C_v is the heat capacity of the gold, d is the Au film thickness, and τ is the time constant of the thermal decay. [75] While this calculation is approximate, it suggests that the heat transfer mechanisms that describe the on-resonance data take place at a rate that is nearly an order of magnitude faster than the phonon-phonon driven TBC across the same Au/hBN (12 +/- 2 MW m^{-2} K^{-1} on the same hBN sample) measured using time-domain thermoreflectance (details in Section D of the Supplementary Information of Ref. [146]). To quantify this Au/PhP hBN thermal boundary conductance more rigorously, we solved the analytical solution to the cylindrical heat equation commonly used to fit standard TDTR data, [83] and fit this solution to our data. This solution predicted a TBC of at least 500 MW m^{-2}K^{-1}, restricted to a lower bound due to sensitivities (details in Section C of Supplementary Information of Ref. [146]). This Au/PhP hBN thermal boundary conductance is roughly 1-2 orders of magnitude higher than phonon-phonon TBCs measured across a plethora of 3D and 2D material interfaces (Fig. 6.3b).

It is of note that our model (shown in Fig. 6.3a) predicts a ×300 increase in effective in-plane polariton conductance in the hBN, consistent with the literature showing enhanced thermal transport in the in-plane direction of hBN due to polaritonic coupling [119, 207, 208]. These relative increases in local polaritonic conduction can be reasoned based on examining the maximum allowed near-field heat flux, q''_{max}, which is predicted as [238]:

$$q''_{\mathrm{max}} = \frac{k_{\mathrm{b}}^2 \left(\frac{\pi}{a}\right)^2}{48\hbar}(T^2_{\mathrm{emitter}} - T^2_{\mathrm{absorber}}) \tag{6.4}$$

where the maximum flux allowed in the near field for a Au/hBN interface can lead to a maximum TBC $\left(G_{\mathrm{max}} = \frac{q''_{\mathrm{max}}}{T_{\mathrm{Au}} - T_{\mathrm{hBN}}}\right)$ of 2.5 GW m^{-2} K^{-1} . Thus, with the coupling of emitted Au energy into

hBN hyperbolic modes and non-ideal transfer within this process, the predicted TBC of 500 MW m^{-2} K^{-1} is reasonable. In the same regard, the group velocity of the local phonon modes which harbor HPhPs is given by the slope of the dispersion [239] which is near zero at the zone center. In contrast, the velocities of the launched hyperbolic modes can be approximated similarly from their dispersion [195]. From Kinetic Theory [31], the thermal conductivity of a system is directly proportional to these velocities, and as the group velocities of hyperbolic modes approach large percentages of the speed of light, the radiative energy flow within these modes will be transferred by the polaritons, thus increasing heat transfer. This enhanced thermal boundary conductance is also supported using a fit to the solution of the 1D heat equation described previously (details in Section C of Supplementary Information of Ref. [146]), [179] further supporting that the value for Au/hBN thermal boundary conductance is quantifiably larger than that due to phonon-phonon conduction alone, and is not a derivative of the assumptions used in our data reduction. We repeat these measurements and fits on three different Au patterns across two different hBN samples, with a consistent enhancement in Au/hBN thermal conductance observed among all "on-resonance" data.

Measurements of polaritonic launching are often performed directly with the use of a scattering-type scanning near-field microscopy (s-SNOM) which allows for the direct excitation and measurement of polaritonic modes [148, 201–204, 215, 232]. However, by the nature of measurements in the near field, the system requires careful alignment and interpretation to isolate the effect of the tip launching and nearby reflecting sites. Using far-field optics, our measurement scheme is able to lock-in to the thermal event in the Au pad and probe the thermal trace of the polaritons through changes in reflection of the Brillouin zone center transverse optical modes and neighboring scattering sites (details in section A of the Supplementary Information of Ref. [146]). Thus, our measured signal is isolated temporally from any optical effect caused by the probe and, due to the high Debye temperature of hBN [240], the TO phonon would be frozen out at even the maximum lattice temperature predicted by conduction (Fig. 6.3b). This confluence of factors points directly to the launching of heat carrying thermally excited polaritonic modes.

Our solution to the heat equation predicts a maximum temperature rise in the hBN of approximately 150 K under these experimental conditions. While the absolute value of this increase is certainly prone to uncertainties in assumed input values, it is still orders of magnitude lower than temperatures required to thermally activate a substantial portion of the high frequency TO phonon

and HPhP modes, and thus during the experimental measurements, the optical modes are nearly entirely frozen out from conductive lattice heating alone (Fig. 6.3c). The temperature needed to obtain a sufficient population of these modes is upwards of 1000 K, which is clearly not the case in our experimental measurements. Thus, this implies that the HPhPs are not excited simply by laser induced changes in the thermal populations, and instead are stimulated non-thermally through direct launching from near-field radiation emitted from the hot Au pad, further supporting our observations of indirect polaritonic coupling, and resultant energy transfer via HPhP-driven TBC.

6.5 Ultrafast heat sink effect

To further confirm this conclusion, we measured the NIR pump-probe response of the Au surface. Fig. 6.4a illustrates the normalized magnitude of the data taken from a pump probe scan on the surface of the gold in the cases of a silicon substrate and an hBN flake. The Au seems to be dramatically cooler in the case of the hBN substrate at early times, strengthening the evidence for the ultrafast cooling mechanism described above. The models outlined in the insets are similar to those used in the case of the MIR probe, where the two temperatures (T_p, and T_e) of the Au transducer couple to the temperatures in the substrate. In the case of silicon, when there is no polaritonic coupling in the substrate, only one temperature (T_p) is considered for the substrate, resulting in a two-temperature model (TTM). For an hBN substrate, however, it was found that the early time curvature could not be fit unless a third temperature (T_{HPhP}) to sink the heat to was considered to account for the polaritonic coupling, hence leading to a three-temperature model (3TM). The insets further describe the coupling mechanisms that were fit for. Fig. 6.4b shows the raw data in the same scans as in Fig. 6.4a for comparison of raw magnitude showing that the surface was overall cooler at all times when comparing the two substrates, indicating the superior heat sink capabilities of hBN in the ultrafast time regime. Fig. 6.4c illustrates the relative sensitivity of the NIR and MIR measurement techniques to the polaritonic interface resistances. We can see that the MIR experiment is an order of magnitude more sensitive to the mechanism than the surface of the Au beyond 10 ps, whereas the Au surface dominates sensitivity before 10 ps as it is in this time regime that the heat from the electrons is being sunk to the polaritons.

The above observations coupled with the prior demonstrations of direct launching of propagating

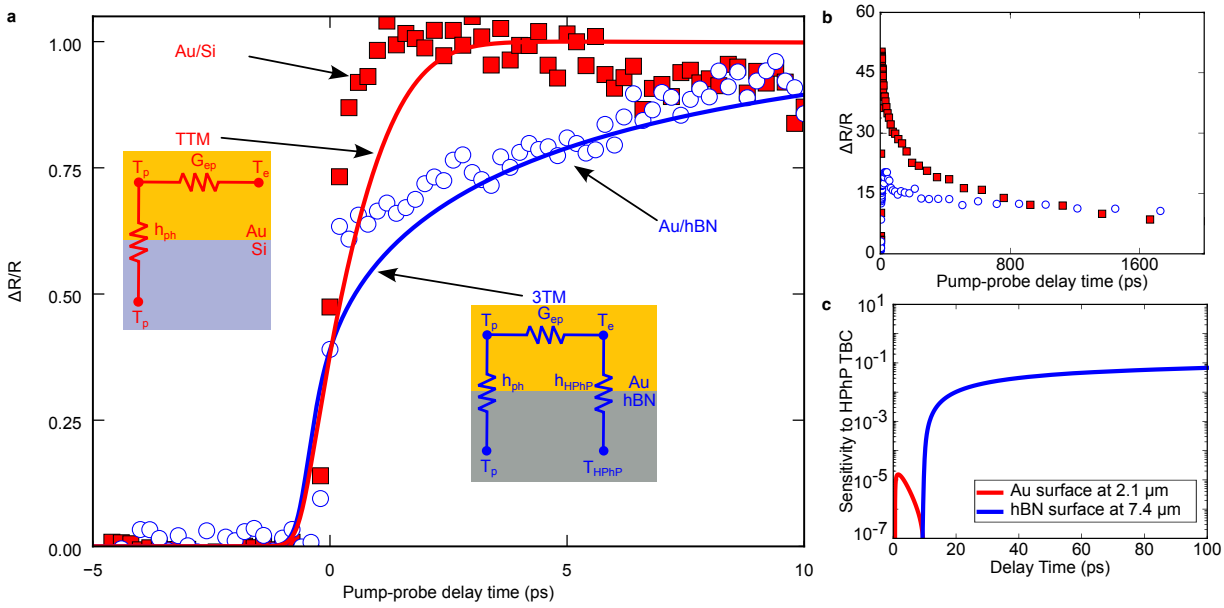

Figure 6.4: **Ultrafast pump-probe response of Au on silicon and hBN substrates using a 520 nm pump and 2.1 um probe.**. At this probe wavelength, the Drude response of the thermoreflectivity of the probe results in sensitivity to the lattice temperature changes in the Au [160, 229]. (a) The solid squares show the measured transient lattice temperature changes in Au when on a Si substrate as well as when on an hBN substrate. The Au lattice temperature changes on hBN during and after the 520-nm pump heating is suppressed at shorter pump-probe delay times and takes longer to rise and equilibrate when coupling to the excited electrons in the Au. This is due to an additional energy loss pathway of the hot electrons in the Au to the hBN substrate, the trends of which we capture with a three-temperature model (3TM) that accounts for a gold electron to hBN HPhP/optical phonon energy transport pathway, shown as a solid blue line assuming this pathway's thermal boundary conductance is 500 MW $m^{-2}K^{-1}$. Note, these ultrafast Au thermoreflectance trends are not captured with a two-temperature model (TTM), which shows a much faster lattice temperature rise when this Au electron-to-substrate thermal boundary conductance is not considered, shown as red solid line. (b) Un-normalized thermoreflectance signal from the data presented in (a), where the reduced magnitude in the signal indicates the overall enhanced cooling of the Au surface. (c) The relative sensitivity of the presented measurements to the HPhP interface coupling.

phonon polaritons via thermal emission reported by Ref. [32] and later by Refs. [241, 242] indicate instead a different model whereby HPhPs serve as the dominant thermal transport mechanism at early timescales. Specifically, we propose the following process. First, the ultrafast visible pump is absorbed by the gold pad, which increases its temperature causing it to radiate. Consistent with phonon-polariton launching via thermal radiation, [32, 242] the local incoherent dipole moment of the thermal radiation provides the energy- and momentum-matching to directly launch HPhPs within the hBN flake. This in turn stimulates a broad spectrum of HPhP (and TO phonon) modes.

Once launched, due to the part optical phonon, part light nature of the HPhP quasiparticles, these modes can carry the thermal energy away from the heat source due to the high heat capacity of the former and the high group velocity (with respect to acoustic phonons) of the latter. A similar mechanism has been recently demonstrated in Ref. [187] where under steady state conditions, the thermal conductivity is enhanced by to surface confined PhPs in silicon carbide. Our work extends these findings to volumetric hyperbolic modes and into the ultrafast regime. This ultrafast mechanism is of critical importance, as while the HPhPs will eventually decay back to conductively heat the local hBN lattice and thus, thermalization of the energy will result in uniform heating of the flake, at ultrafast timescales this provides opportunities for extracting the heat from localized hot-spots before catastrophic processes occur (such as device failure). Our results should lay the groundwork for a new generation of photonic sources and an efficient transport mechanism for mode specific heat sinks in high frequency electronics.

Here, we have experimentally established the potential for ultrafast, thermal transport across solid-solid interfaces via the transduction of thermal energy from a transiently heated gold pad into HPhPs supported within hBN. This mechanism provides insight into the role that polaritonic modes can offer in the realm of interfacial heat transfer, overcoming the traditional limitations of phonon-dictated TBC. Specifically, we demonstrate that polaritonic coupling can facilitate the optical modes to move heat across and away from a Au/hBN interface over an order of magnitude faster than acoustic phonon conduction in the same system. These investigations provide the initial forays into understanding the fundamental guiding principles of such ultrafast transport phenomena. Thus, through further studies of polariton-phonon scattering rates and a quantification of energy tunneling through different interlayers, we hope to elucidate the effectiveness of this energy transfer, including quantifying the maximum heat flux and capacity. The mechanism demonstrated in this work holds significant potential for cooling interconnects via radiative absorption. Subsequent research endeavors can leverage this study as a basis for expanding thermal transport to include transducer cooling, as well as enhancing interfacial flow through more precise nonequilibrium experiments. The impact of this new mechanism has two main features that stand out: speed and controllability. Once the thermal energy is being carried by a polariton, it is travelling at ultrasonic speeds, which means that for high power or high frequency electronic devices that accumulate heat via joule heating, this mechanism can remove heat faster than it is accumulated. This would help next-

generation devices to maintain safe operating temperatures, even at higher current densities or near local defect-induced hot-spots. The ability to design polaritonic modes through selection of materials and patterning of optical devices also allows for several advancements in novel computers, and thermal management. This new mechanism also serves to employ thermal energy to launch polaritons, meaning that photonic circuits may be able to have a useful nanoscale source for photons. Thermally, these results let us design and optimize new devices "shielded" from evanescent radiation by polaritonic absorbers.

6.6 Methods

6.6.1 Device Preparation

The hBN flakes were prepared from ^{11}B isotopically enriched source crystals by the standard mechanical exfoliation process onto oxygen plasma treated silicon substrates. As reported in ref. [148] of the main text and [243, 244] the hBN source crystals were produced by precipitation from a molten metal solution using isotopically enriched precursors (nominally 99.4 % ^{11}B) provided by a commercial source. To fabricate the samples, the hBN flakes were initially exfoliated onto a bilayer resist transfer wafer where they were imaged optically and via AFM to down select the ideal flakes for these experiments. Transfer of the flakes onto a standard thermal SiO_2 film on a silicon substrate was performed via standard approaches in a home-built two-dimensional material transfer microscope. The gold pads were patterned using electron beam lithography, development, electron-beam deposition of a 50-nm thick gold film, followed by a standard liftoff procedure in n-methyl pyrrolidone (NMP). The flake sizes were characterized by atomic force microscopy and patterned using electron beam lithography, followed by electron beam deposition of a 50 nm gold film.

6.6.2 Polariton Characterization

Near-field nano-imaging experiments were carried out in a commercial Neaspec s-SNOM based around a tapping-mode atomic force microscope. A metal-coated Si tip of apex radius R $\sim$ 20 nm that oscillates at a frequency of $\Omega \sim 280$ kHz and tapping amplitude of about 100 nm was illuminated by a monochromatic quantum cascade laser beam at a free-space incident wavelength

λ = 6.9-6.6 µm and at an angle 60° off normal to the sample surface, with the incident light being p-polarized. Because s-SNOM predominantly couples to p-polarized component, the signal detected is dominated by HPhP signals, which can only emerge from p-polarized light (see ref. [216] of the main text). Scattered light launches HPhPs in the device and the tip then rescatters light for detection in the far-field. [182] Similar to previous studies of HPhPs using s-SNOM, the presence of the metallic tip will lead to the presence of a tip-launched mode. Background signals were efficiently suppressed by demodulating the detector signal at the third harmonic of the tip oscillation frequency and using pseudo-heterodyne interferometric detection. In s-SNOM images, HPhPs can be observed in two ways: first, polaritons launched by light scattered from the s-SNOM tip propagate radially away from the tip and reflect back from sample boundaries for example, a flake edge, creating interference fringes with spacing λ_{HPhP} divided by two (as in ref. [195] of the main text and [245, 246]) which are scattered back to free space by the tip and detected. Alternatively, polaritons can be directly launched from the edge of $h^{11}BN$ flakes and then propagate across the surface and interfere with the incident field at the tip, producing fringes with spacing λ_{HPhP} .(see refs. [148, 233, 234] of the main text)The simulated dispersion plot is generated using a transfer matrix method to determine the reflection coefficients from Fresnel's equations using the reported dielectric function from reference [148] of the main text and [108](See Section B of the Supplementary Information of Ref. [146]).

Chapter 7

Engineering ultrafast thermal tunneling

With the experimental observation of ultrafast transfer via polaritonic absorption confirmed, the design and optimization of thermalization from polaritons to the substrate can now be engineered. In this chapter, I use an infrared time-domain thermoreflectance (TTR) system to quantify the effectiveness of an ultrafast heat sink. The samples presented were designed, and grown in collaboration with Jon-Paul Maria's group. I then apply the formalism outlined in 4 to explore the phenomenon of thermal tunneling through a resistive interlayer. The work presented here is currently being prepared for journal submission.

7.1 Motivation

Photonic metamaterials are nanocomposite structures engineered to optimize their dielectric character. In recent years, there have been significant advances in far- and near-field optical control, such as hyperlensing [181, 247–249], radiative cooling [250–255], and invisibility cloaks [256], bringing rich depth to the field of optics. Many metamaterials are constructed by periodically stacking alternating sub-wavelength thin films, forming so-called superlattices. These architectures can be carefully constructed not only to control the reflected light, but also to manipulate the entire dispersion relation of light. Another striking feature of many of these engineered superlattices, which are typically anisotropic, is the emergence of the bulk propagation of vibrational modes [70], which otherwise would be restricted to the interfaces between the superlattice layers. This phenomenon has led to the development of a class of metamaterials featuring quasi-particles with hyperbolic dispersion, so-called hyperbolic metamaterials (HMM) [117, 248, 257]. These HMMs enable sub-diffractional confinement of light due to extreme anisotropy and can enhance the propagation of

engineered quasi-particles.

Among various HMM systems, cadmium oxide (CdO) superlattices have emerged as a particularly promising platform for supporting novel polaritonic behavior. Highly doped CdO superlattices have recently been shown to support the first known hyperbolic plasmon polariton (HPP) [258]. The high carrier mobilities allowed by CdO have been shown to exhibit strong coupling [259], epsilon near zero (ENZ) emission [260], and Tamm plasmon polaritons [261], all with high tunability. Despite these promising features, direct experimental probing of thermal energy transfer in such systems presents unique challenges. As previous experiments have shown [146, 187], intense near-field emission can result in heat being absorbed into PhPs of h-BN and SiC more efficiently than via conductive processes across the same interface. However, optical phonons alone exhibit relatively slow thermal transport unless polaritonically accelerated [47], and strong reflectivity in the Reststrahlen band can obscure direct probing of energy transfer from polaritonic absorbers to substrates.

To address these limitations, I explore an alternative energy extraction strategy based on spectral matching and tunneling principles. The high tunability of hyperbolic CdO superlattices [258] makes engineering their dielectric function more feasible than with phonon polaritons. This tunability enables direct investigation of thermal transport via hyperbolic modes, not only during absorption and generation, but also during intrinsic and substrate scattering. Once the heat is transferred to ultrafast polaritonic modes, it should be extracted just as equally fast; otherwise, the energy will dissipate into the lattice, causing the same bulk heating expected from conduction into the substrate, merely accelerated at early timescales. To avoid this, we employ a spectrally selective thermal sink designed to absorb near-field modes generated in the hyperbolic absorber. This is achieved by using a CdO layer with ENZ mode matched in absorption. Additionally, we explore the principle of thermal tunneling by separating the ultrafast sink and hyperbolic absorber with a thin dielectric.

7.2 Growth and Design

High-power impulse magnetron sputtering (HiPIMS) was used to grow CdO superlattices with alternating carrier concentrations at 3×10^{20} cm^{-3}, and 3×10^{19} cm^{-3}. The resulting thin film has

a complex dielectric structure from strong anisotropy between the intrinsic in-plane carrier density and manufactured variance through plane. These were grown on an alumina substrate as a control, a tuned ENZ CdO to investigate the speed of a polarionic heat sink, and finally a magniesium oxide/ENZ CdO stack to tunnel the thermal energy through a conductively resistive interlayer. The resultant stacks were then optically analyzed with Infrared variable angle spectroscopic ellipsometry (IR-VASE) to determine the dielectric function of each layer, as well as the overall superlattice dielectric function. With the dielectric functions known, predictions of the evanescent transfer (ξ) within each layer were calculated from the fluctuational electrodynamics (FED) formalism detailed in Ref. [66].

To measure the thermal events within the stack, we employ a spectrally resolved infrared (IR) transient thermoreflectance (TTR) technique similar to Ref. [146], which measures the temperature of the superlattice surface within the polaritonic range. To act as a thermal transducer, we pattern a central 50 nm Au pad sized to match the spot size of the visible pump beam, minimizing any heating of the superlattice. Surrounding the Au pad is a reflector ring to confine the hyperbolic plasmon polaritons (HPPs) within the radius of the MIR probe, effectively increasing sensitivity to the reflectance changes that signify HPP activity. The stack is constructed to support a Type I hyperbolic mode in the range of 1.9-2.5 μm and a Type II hyperbolic mode in the range of 2.6-5.3 μm. Both of these are within the spectral sensitivity range of IR-TTR and within the transparency region of alumina. The ENZ sub-layer is selected to be spectrally matched to the translucent edge of the hyperbolic region of the HMM. When heated via a laser source, the electrons in the gold are expected to reach temperatures above 2500 K. The resulting broadband near-field emission from the Drude oscillator directly excites the hyperbolic modes in the superlattice. Those hyperbolic modes will then sink into the CdO ENZ film preempting any thermalization of the heat within the superlattice.

Figure 7.1(a) outlines the experimental design utilizing the IR-TTR system along with the polariton heat sink mechanism proposed for thermalizing the polaritonic energy. The calculated transfer function between the CdO superlattice and the ENZ sink, shown in 7.1(b), indicates that the modes between the type 1 and type 2 hyperbolic regions are the most active in thermal transport. This is confirmed with the experimental IR-TTR data in Fig. 7.1(c), where increased activity can be seen in this region. More information on the thermal process and propagation of

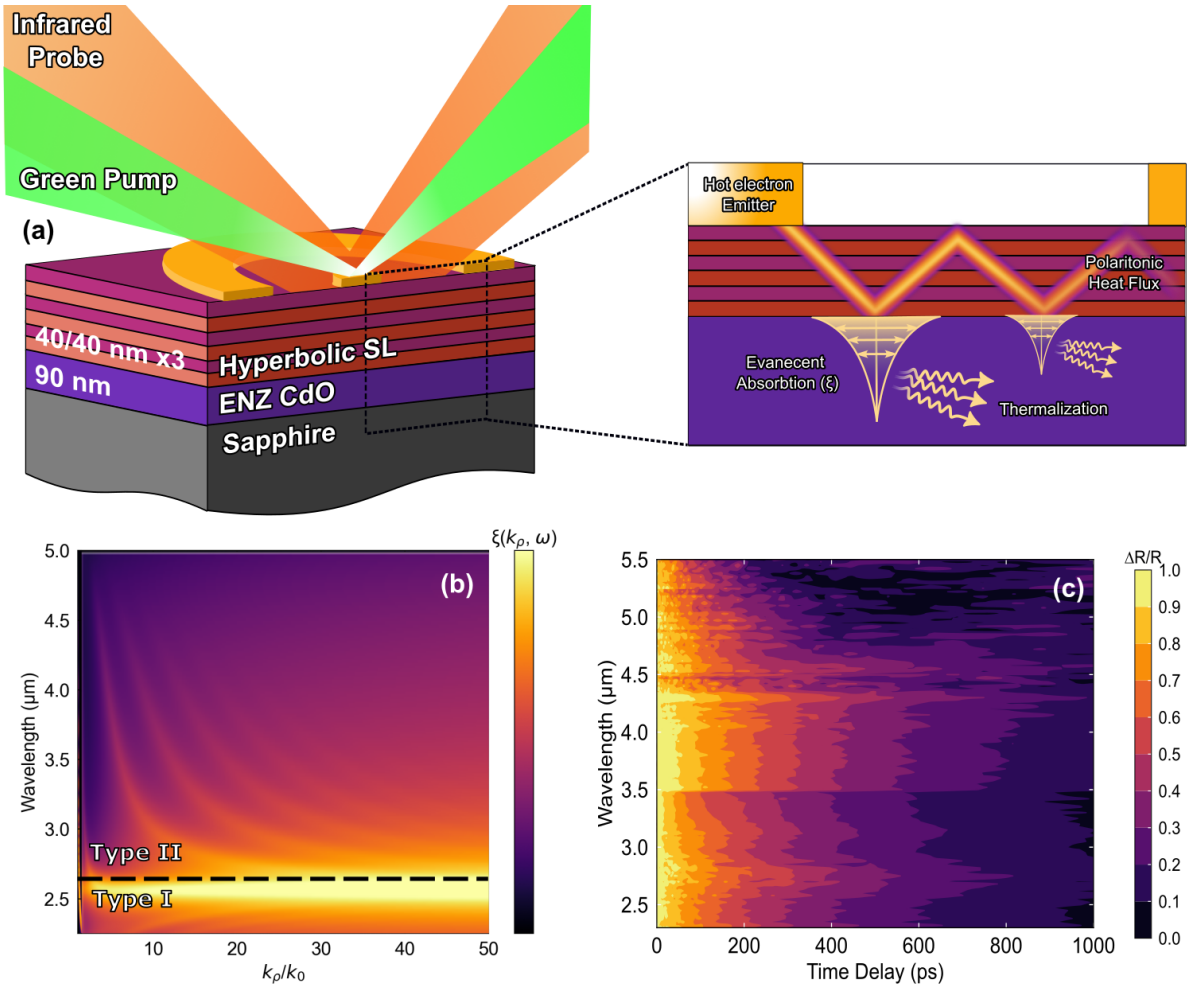

Figure 7.1: **Experimental schematic and radiative transfer in CdO meta-materials**: (a) A schematic of the experiment performed in this work, where a green pump laser is focused onto a circular gold pad exciting hot electrons to radiate energy into the hyperbolic superlattice (SL) inducing polariton launching. A gold ring is used as a reflector to contain the polaritonic energy within the region where a larger infrared probe beam measures the surface temperature of the SL. The polariton then evanescently transfers its energy into a spectrally matched epsilon-near-zero (ENZ) CdO heat sink. (b) The spectral transfer function (ξ) between the hyperbolic SL and the ENZ CdO, specifically around the Type 1 hyperbolic mode. (c) The measured thermal decay spectra from the surface of the SL to the CdO heat sink highlight enhanced thermal transfer at the type-I edge, indicative of polaritonic transport.

energy into the heat sink can be extracted by taking a temporal slice of the measured contour in Fig. 7.1(c) at 2.5 microns, the peak of polaritonic absorption shown in Fig. 7.1(b).

7.3 Discussion

Once polaritonic heat is launched into the superlattice, in the case of no spectrally matched heat sink, the energy remains confined within the CdO superlattice. In this scenario, the heat within these ultrafast modes, physically restricted by the resonating ring, is scattered into slower, conventional conductive transport channels. We see an exhibition of this behavior in Fig. 7.1(a), where, in the absence of an ultrafast sink, the surface of the superlattice cools following a characteristic exponential decay. This decay profile reflects single-mode thermal transport, where the decay lifetime is inversely proportional to thermal conductance.

In contrast, when a thermal heat sink is present, we see a distinctly different transport signature emerging at times shorter than 13.5 ps. In this regime, an additional mode of transport is present quickly reducing the temperature at the surface. This timescale aligns closely with that reported in Ref. [146] as the characteristic duration of interfacial energy exchange between a gold emitter and a hyperbolic absorber. However, in the case measured in this work, we are instead measuring the decay of the polaritonic heat within a hyperbolic material; the 13.5 ps interval observed here marks the characteristic timescale of polaritonic propagation from within the superlattice to the CdO heat sink. This implies that the energy initially present in the polaritonic system at 0 ps is substantially dissipated by 13.5 ps, requiring propagation across a 240 nm interface within that time. Using this, we can estimate the propagation speed of the thermal polaritons as

$$v_{polariton} = \frac{d}{\tau} = \frac{240\text{nm}}{13.5\text{ps}} = 17,778 \text{ m.s.}^{-1} \tag{7.1}$$

However, this speed is a dramatic underestimation, as it assumes that the duration of the polaritonic launching is a Dirac delta function at t = 0 ps. Prior work shows that the magnitude of electron-phonon nonequilibrium required for polaritonic launching in gold is on the order of 10 ps. We then can reassess the propagation speed by subtracting out the duration of the pump event, giving a propagation speed as

$$v_{polariton} = \frac{240\text{nm}}{3.5\text{ps}} = 68,571 \text{ m.s.}^{-1} \tag{7.2}$$

This estimation suggests that the propagation of thermal polaritons is up to $\sim 10\times$ faster than the

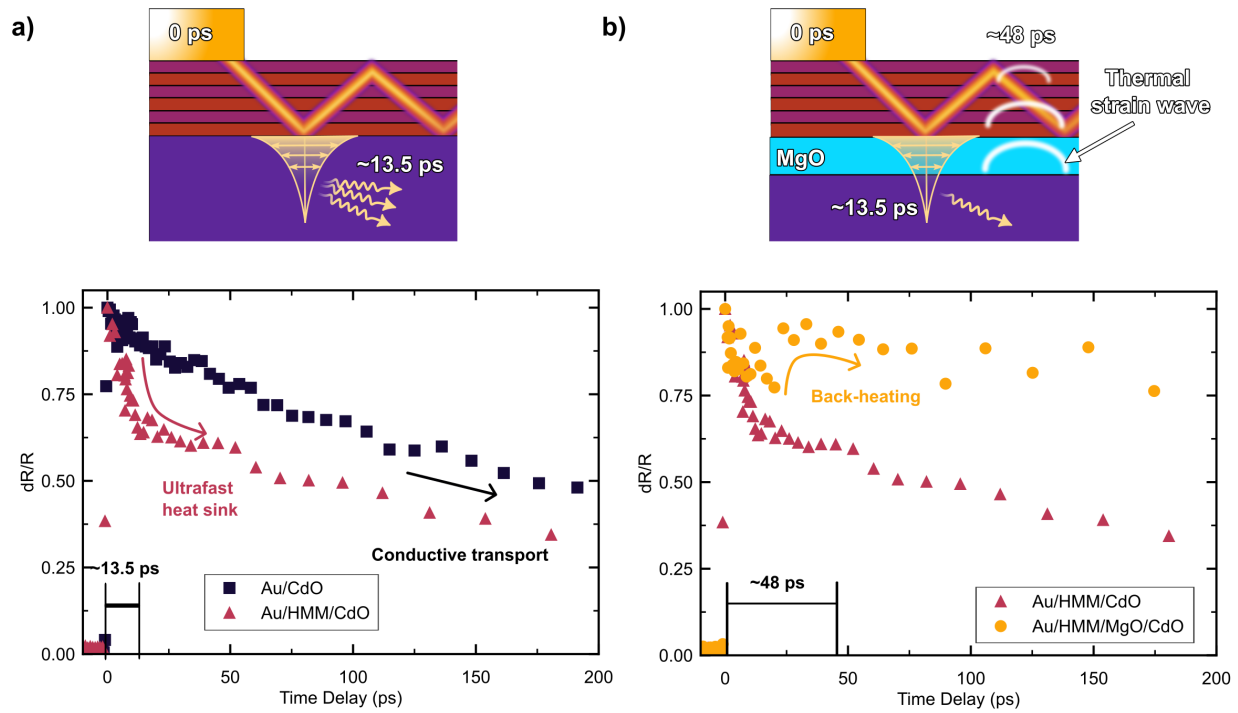

Figure 7.2: **Measured thermal decays at 2.5 μm.** (a) A comparison of normalized thermal decays with and without an ultrafast heat sink, with an accompanying schematic of the heat sink mechanism labeled with the duration of the heat sink effect. Conductive processes dominate at longer times, implied by the convergence to identical slopes. (b) Thermal decays with and without a 30nm magnesia spacing layer, with an example schematic showing back heating caused by conductive thermal wave propagating to the surface after the sinking of thermal energy into the ENZ.

sound speed in the CdO superlattice.

Finally, when separating the superlattice from the heat sink, as depicted in Fig. 7.2(b), we see an identical cooling rate within 3-4 ps after excitation; this mirrors the timescale discussed above, affirming rapid heat extraction. Additionally, a strong secondary signature appears at 48 ps, indicating thermal energy reflecting back to the surface. Both signatures show the effect of an ultrafast thermal tunneling event cooling the superlattice. This delayed signal is consistent with a back-propagating thermal wave moving at the average sound speed of the material stack. Assuming a known literature value for the sound speed in the magnesium oxide (MgO) spacer (9500 m.s.$^{-1}$) [262], we derive an effective sound speed for CdO as

$$v_{s,eff} = \left[48\text{ps} - \frac{30\text{ nm}}{9500\text{ m.s.}^{-1}}\right]^{-1} = 5,352\text{ m.s.}^{-1} \tag{7.3}$$

This value agrees with experimental measurements of CdO and confirms the tunneling of thermal energy beneath the magnesia spacer [263]. It represents the first thermal quantification of evanescent heat tunneling, providing direct evidence of energy transfer through non-radiative, near-field interactions in nanostructured systems. The confirmation of this phenomenon has significant implications for the development of ultrafast thermal diodes, particularly for heat management in sensitive nanoscale devices. Moreover, this discovery opens promising avenues for engineering evanescent transport from the hot electrons of field-effect transistors [7], thermophotovoltaics [228, 264], and tuning the flow of slow-light [181, 182].

7.4 Conclusion

In this study, I experimentally investigated and modeled near-field radiative heat transfer from a radiating gold source into the hyperbolic plasmon polaritons (HPPs) of a CdO metamaterial, followed by the evanescent tunneling of heat across a cold insulating magnesia interlayer into a spectrally matched ENZ CdO absorber. First, radiative predictions from fluctuational electrodynamics guided the design of an ultrafast polaritonic heat sink using an ENZ absorber. Next, spectrally and temporally resolved measurements quantified the magnitude and dynamics of energy extraction. These measurements were then extended to a system with a 30 nm magnesia interlayer, enabling the first experimental demonstration of room-temperature thermal tunneling. Finally, the propagation speeds of polaritonic thermal transfer were found to be approximately $10\times$ faster than the speed of sound, highlighting their potential for rapid heat management. These findings pave the way for the development of ultrafast electronic coolers for high-power circuits and inspire new designs for nanoscale thermal tunneling devices.

Chapter 8

Summary and Future Directions

In this thesis, I investigate the fundamental thermal transport across solid state interfaces, combining conductive transport and near-field radiation formalisms. In Chapter 2, I provide an overview of the basic concepts governing thermal transport for both conductive and radiation. Chapter 3 outlines the metrology used to observe and quantify the mechanisms investigated in this thesis. In Chapter 4, I establish the theoretical framework of interfacial radiative transport in electron-phonon non-equilibrium, and identify the dominant physical parameters dictating the speed and magnitude of the evanescent transfer. An experimental validation and design of a transient thermoreflectance technique, tuned to measure the temperature of specific resonances, is detailed in Chapter 5. The IR-VASE measurements provided in this work also highlight the effectiveness of mid-infrared resonances as thermometers, which exceed the sensitivity of standard metal transducers used in TDTR. In Chapter 6, I employ both the theoretical formulations and experimental design developed thus far to quantify the magnitude of ultrafast interfacial transport from a gold radiator to a hexagonal boron nitride absorber. This represents the first-ever measurement of solid-state near field heat transport across and interface at room temperature. Finally, in Chapter 7, I present the first steps toward functional devices leveraging the implications of my prior work. This work identifies an estimate of the propagation speed of thermal energy, and presents proposed techniques for dissipating polaritonic heat before it thermalizes with the lattice.
Based on the works in this thesis, there are many opportunities for future investigations,

- In chapter 4, I develop current radiative theory to be congruent with conductive heat transport. Extending this, intrinsic and interfacial radiative conduction can be extended to the cases of extreme lattice temperature (i.e., $T_p > 1500$ K). In this case, the radiation across solid state interfaces, especially in the near field, would rival conduction even in weakly absorbing media. Quantifying this process would greatly aid the design of efficient thermal management

systems in extreme environments.

- in chapter 5, I quantify the effectiveness of optical phonon resonances as thermometers. I find that due to the sharpness of these modes, their thermorefectance exceeds the standard metal transducers. The implication of this is that a thermometry technique optimized in the MIR spectral region could provide the most precise optical technique for measuring thermal properties. Furthermore, the transparent regions of dielectric transducers allow for spacial separation of the pump and probe events through the depth of a sample, reproducing a nano-laser-flash measurement.

- In chapter 6, I measure the diffuse thermal transport from a thin gold film into the confined polaritonic modes in h-BN. This effectively focuses and rectifies the thermal energy into momentum confined optical modes. With this idea, one could explore manipulating the optical modes with highly confined hyperbolic systems, or develop a simple thermal circuit triggered by a polaritonic interaction to prevent thermal runaway at the nanoscale.

- In chapter 7, I engineer ultrafast heat CdO heat sinks and quantify the propagation speed of polaritonic heat. Extending the observations at 2.5 microns to the entire hyperbolic region would reveal a spectrally resolved propagation speed of hyperbolic heat transport. Towards this goal, we are currently growing the dataset beyond what was presented in Chapter 7.

Chapter A

Appendix and Supplementary materials for Chapter 4

A.1 Appendix A: Plasma Frequency Calculation

The plasma frequency of the metallic thin film was found as described in Eq. 2 of the manuscript, given by

$$\omega_p(T_e) = \sqrt{\frac{n_e(T_e)e^2}{4\pi m^*(T_e)\epsilon_0}} \tag{A1}$$

where ε_0 and e are the vacuum permittivity and electron charge, respectively. The temperature-dependent parameters in this equation are n_e and m^*, which represent the number density and effective mass of electrons, respectively. The number density of electrons, n_e, was calculated from the integration of the occupied density of states (ODOS), $g(\epsilon, T_e)$, across all energies, ϵ. The ODOS was obtained by multiplying the ground state density of states (DOS), $D(\epsilon)$, by the Fermi Dirac distribution, $f_{FD}(\epsilon, T_e)$, as

$$g(\epsilon, T_e) = D(\epsilon).f_{FD}(\epsilon, T_e) \tag{A2}$$

To find DOS for each metal film, we conducted self-consistent field calculations in the Quantum ESPRESSO package [50] using a $8 \times 8 \times 8$ grid of k-points. The number density of states was then calculated as

$$n_e(T_e) = \int_0^\infty g(\epsilon, T_e)d\epsilon = \int_0^\infty D(\epsilon)f(\epsilon, T_e)d\epsilon \tag{A3}$$

The thermal effective mass for each metal film was retrieved by the Ashcroft and Mermin formulation [60] as

$$m^*(T_e) = \frac{\gamma(T_e)}{\gamma_{\text{free}}(T_e)} \tag{A4}$$

where γ and γ_{free} are the actual and free-electron Sommerfeld Coefficients, respectively. The values of γ and γ_{free} for each metal film at given T_e is found as

$$\gamma(T_e) = \frac{C_e(T_e)}{T_e} \tag{A5}$$

$$\gamma_{\text{free}}(T_e) = \frac{\pi^2 n_e(T_e) k_b^2}{2\mu(T_e)} \tag{A6}$$

where C_e is the heat capacity of electrons, μ is the chemical potential, and k_b is the Boltzmann constant. Finally, with electron effective mass and number density calculated, the plasma frequency of each metal film was found.

A.2 Appendix B: Electron Scattering Rate Calculation

The electron-electron scattering rate was obtained using the Fermi liquid theory formulation, described in Ref. [57], as

$$\begin{aligned}\Gamma_{ee}(T_e) = \frac{e^4 k_F^2}{16\pi^3 \hbar^4 \varepsilon_0^2 v_F^3 q_s^2} &\left[\frac{2k_F}{4k_F + q_s^2} + \frac{1}{q_s}\arctan\left(\frac{2k_F}{q_s}\right)\right] \\ &\times \left[\pi^2 + \left(\frac{\epsilon - \epsilon_F - \mu}{k_B T_e}\right)^2\right](k_B T_e)^2\end{aligned} \tag{B1}$$

where k_F and v_F are the Fermi momentum and velocity respectively and are related to the Fermi energy, ϵ_F, and the rest mass of the electron, m_e, as

$$k_F = \sqrt{2 m_e \epsilon_F}/\hbar \tag{B2}$$

$$v_F = k_F \hbar / m_e \tag{B3}$$

where $\hbar$ and m_e are the reduced Planck constant and the rest mass of an electron, respectively. Also, q_s represents the screening length of the electron, that is the distance at which the electrostatic force of the electron is attenuated. The screening length in the above formulation is given by Bohm and Pines [143] as

$$q_{BP}^{-1} = \frac{4\pi\varepsilon_0 \hbar^2 1.47 r_s^{1/2}}{e^2 m_e} \tag{B4}$$

where r_s is the inter-electron distance of the simulated metal given by

$$r_s = \frac{4\pi\varepsilon_0\hbar^2(3/4\pi n_e)^{1/3}}{e^2 m_e} \tag{B5}$$

The electron-phonon scattering rate for each metal film was found by following the formula reported in Ref. [58]:

$$\Gamma_{ep}^{-1}(T_e) = \frac{\pi^2}{6}\frac{m^*(T_e)C_s^2 n_e(T_e)}{G_{ep}(T_e)T_e} \tag{B6}$$

where C_s is the Debye sound speed of the metal given by

$$\frac{3}{C_s^3} = \frac{1}{u_L^3} + \frac{2}{u_T^3} \tag{B7}$$

In Eq. (S13), u_L and u_T are the longitudinal and transverse sound speeds, respectively. The values of the longitudinal and transverse sound speeds for each simulated metal can be found in Table S1.

To find the electron-boundary scattering rate, we followed the formula reported in Ref. [71] as

$$\Gamma_{eb}(T_e) = \frac{3\pi}{35\zeta(3)\Gamma_{ep}^{-1}(T_e)q_T t}\left[1 + 2\left(\frac{u_L}{u_T}\right)^3\right] \tag{B8}$$

where ζ is the Riemann-Zeta function, q_T is the wavevector of a thermal longitudinal phonon ($q_T = T_p/u_L$), and t is the thickness of the metal film.

A.3 Appendix C: Radiative Heat Flux Calculation

Fig. A1 represents a schematic of the radiative heat transfer problem under consideration as a one-dimensional layered configuration with two solid-state layers. In this configuration, layer 1 is a thin metallic film emitter (with a thickness of t) with a bulk vacuum layer on top, and layer 2 is a receiving dielectric half-space. The dielectric response of each layer is described using a frequency-dependent dielectric function, $\varepsilon(\omega) = \varepsilon'(\omega) + i\varepsilon''(\omega)$. As layers are infinitely long in x- and y-directions, we only consider heat flux along z-axis. Utilizing the framework of fluctuational electrodynamics [66] in Cartesian coordinates, the spectral radiative heat transfer (q_ω) from the

thin film to the substrate is given by the time-averaged z-component of the Poynting vector, as

$$q_\omega = 2\mathbf{Re}[< E_x H_y^* - E_y H_x^* >] \tag{A1}$$

where $*$ denotes the complex conjugate. Here, E_x and E_y (H_x and H_y) are respectively the x- and y-components of the electric (magnetic) field $\mathbf{E}$ ($\mathbf{H}$), thermally emitted by the thin film. These thermally emitted fields can be found using the fluctuation-dissipation theorem and formalism of dyadic Green's function [66]. By adopting a polar coordinate system and considering the azimuthal symmetry of the configuration, the radiative heat flux is then found as

$$\begin{aligned} q_\omega = &\int_0^{k_{\max}} \frac{k_0^2 \Theta(\omega, T)}{\pi^2} \times \\ &\mathbf{Re}\left[i \int_0^t \sum_{\alpha=\rho,\theta,z} \varepsilon''(\omega)(\mathbf{g}^E_{\rho\alpha}\mathbf{g}^{H^*}_{\theta\alpha} - \mathbf{g}^E_{\theta\alpha}\mathbf{g}^{H^*}_{\rho\alpha}) dz \right] k_\rho \mathrm{d}k_\rho \end{aligned} \tag{A2}$$

where Θ is the mean energy of electromagnetic states, k_0 is the vacuum wavevector, and k_ρ is the parallel (relative to the surface) component of the wavevector. In this study, we set the upper wavevector limit $k_{\max} = \pi/a$, where a is the lattice constant of the material. This choice reflects the physical limit imposed by the material's atomic structure and photonic response [147]. Also, $\mathbf{g}$ is the Weyl component of DGFs, given by

$$\mathbf{g}^E(\omega, k_\rho) = \frac{i}{2k_{z1}} \begin{bmatrix} (A_2^{TE}\widehat{\mathbf{ss}} + A_2^{TM}\widehat{\mathbf{p}}_2^+\widehat{\mathbf{p}}_1^+)e^{-ik_{z1}z} \\ +(B_2^{TE}\widehat{\mathbf{ss}} + B_2^{TM}\widehat{\mathbf{p}}_2^-\widehat{\mathbf{p}}_1^+)e^{-ik_{z1}z} \\ +(C_2^{TE}\widehat{\mathbf{ss}} + C_2^{TM}\widehat{\mathbf{p}}_2^+\widehat{\mathbf{p}}_1^-)e^{ik_{z1}z} \\ +(D_2^{TE}\widehat{\mathbf{ss}} + D_2^{TM}\widehat{\mathbf{p}}_2^-\widehat{\mathbf{p}}_1^-)e^{ik_{z1}z} \end{bmatrix} \tag{A3}$$

$$\mathbf{g}^H(\omega, k_\rho) = \frac{k_2}{2k_{z1}} \begin{bmatrix} (A_2^{TE}\widehat{\mathbf{p}}_2^+\widehat{\mathbf{s}} - A_2^{TM}\widehat{\mathbf{s}}\widehat{\mathbf{p}}_1^+)e^{-ik_{z1}z} \\ +(B_2^{TE}\widehat{\mathbf{p}}_2^-\widehat{\mathbf{s}} - B_2^{TM}\widehat{\mathbf{s}}\widehat{\mathbf{p}}_1^+)e^{-ik_{z1}z} \\ +(C_2^{TE}\widehat{\mathbf{p}}_2^+\widehat{\mathbf{s}} - C_2^{TM}\widehat{\mathbf{s}}\widehat{\mathbf{p}}_1^-)e^{ik_{z1}z} \\ +(D_2^{TE}\widehat{\mathbf{p}}_2^-\widehat{\mathbf{s}} - D_2^{TM}\widehat{\mathbf{s}}\widehat{\mathbf{p}}_1^-)e^{ik_{z1}z} \end{bmatrix} \tag{A4}$$

Here, superscript TE and TM refer to the transverse electric and transverse magnetic polarizations, respectively. Also, $\widehat{\mathbf{s}}$ and $\widehat{\mathbf{p}}_i^\pm$ are respectively the Sipe unit vectors inside ith layer for TE-

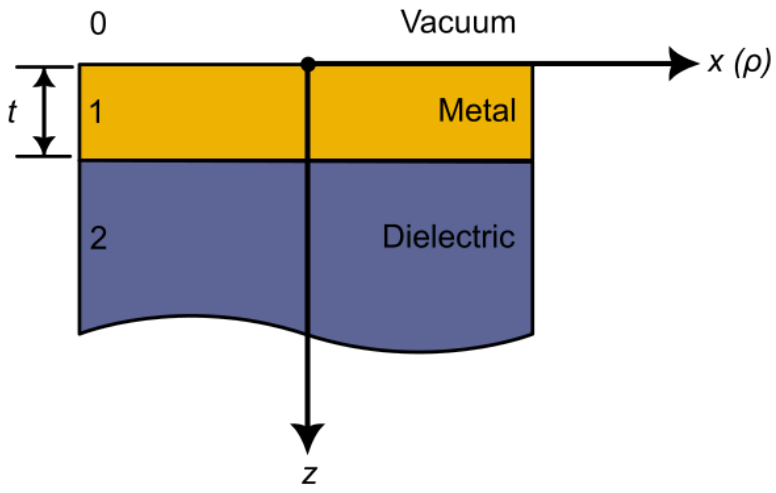

Figure A1: Schematic diagram of the configuration considered for radiative heat flux calculations.

and TM-polarizations, given by

$$\widehat{\mathbf{s}} = -\widehat{\theta} \tag{A5}$$

$$\widehat{\mathbf{p}}_i^{\pm} = \frac{1}{k_i}\left(\mp k_{z1}\widehat{\rho} + k_\rho \widehat{z}\right) \tag{A6}$$

where $k_i = \sqrt{\varepsilon_i} k_0$ and $k_{zi} = \sqrt{k_i^2 - k_\rho^2}$. Finally, the coefficients A_2^γ (B_2^γ) and C_2^γ (D_2^γ) represent the amplitude of waves traveling toward the positive (negative) direction of the z-axis in γ-polarization (where $\gamma = TE$ or TM) due to thermal sources emitting in the positive and negative directions of the z-axis, respectively. These coefficients can be found using the scattering matrix method described in Ref. [66].

A.4 Supplemental Material for Chapter 4

A.5 Section A: Temperature Dependence of Electronic Properties

To find the temperature dependence of plasma frequency, the variation of n_e, found from Eq. A3, with electron temperature was calculated as shown in Fig. S1 across the temperature range of 300-5000 K for each metal considered in this study. We also retrieved the values of C_e and μ across the simulated electron temperature range from the calculations performed by Lin et al. [137], as shown in Figs. S2 and S3, respectively. Using these values, we calculated γ and γ_{free} at

different temperatures and, consequently, the temperature dependence of electron effective mass was computed for each metal film as shown in Fig. S4. Finally, with electron number density and effective mass calculated, the plasma frequency of each metal film was found as shown in Fig. 4.2 of the main manuscript.

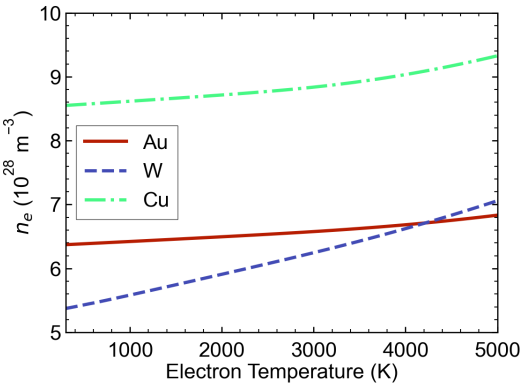

Figure S1: Variation of the electron number density with electron temperature for gold, tungsten, and copper.

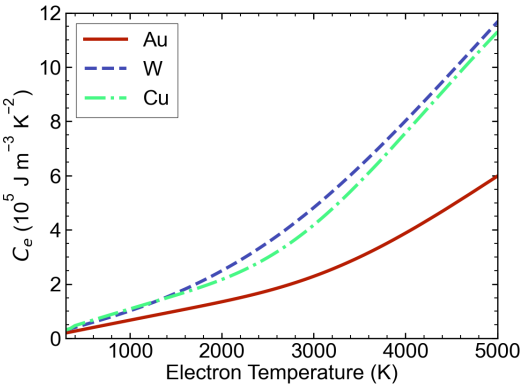

Figure S2: Temperature dependence of the heat capacity of electrons for gold, tungsten, and copper, retrieved from Ref. [137].

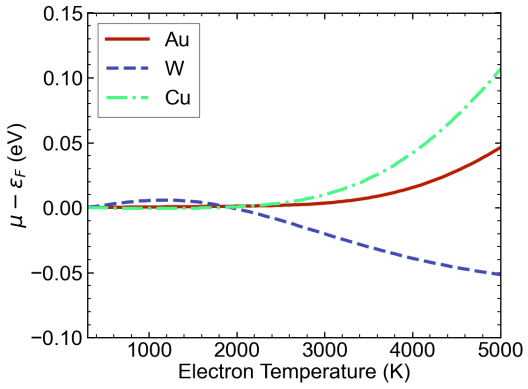

Figure S3: Temperature dependence of the chemical potential for gold, tungsten, and copper, retrieved from Ref. [137]. Here, ε_f is the Fermi energy.

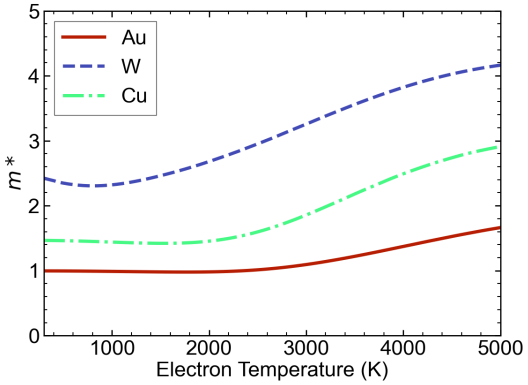

Figure S4: Temperature dependence of the electron effective mass for gold, tungsten, and copper.

A.6 Section B: Temperature Dependence of Electron-Phonon Coupling

The electron-phonon coupling parameter, G_{ep}, was retrieved from Ref. [137] for each metal film and is depicted in Fig. S5. This work used *ab initio* density fluctuational theory (DFT) calculations using *VASP* [265] at electron temperatures ranging from 0 to 5000 K. The functional relationship between Γ_{ep} and G_{ep} is reported in Ref. [96] to describe the case of hot electrons after laser irradiation similar to the situation depicted in Fig. 4.1a of the main manuscript. By inspection, we see that G_{ep} is relatively constant from 0 to 2000 K only increasing significantly above this. By comparison to Fig. 4.2a-c in the main manuscript, we see a slight change in curvature in this region for the calculated values of Γ_{ep}. This implies a direct relationship between G_{ep} and Γ_{ep} as expected from Eq. (B6). However, with the similar change in curvatures found between G_{ep} and

m^*, the two effects compete and contribute to the overall reduction in curvature seen in Fig. 4.2 of the main text. Also, the values of the longitudinal and transverse sound speeds for each simulated metal can be found in Table S1.

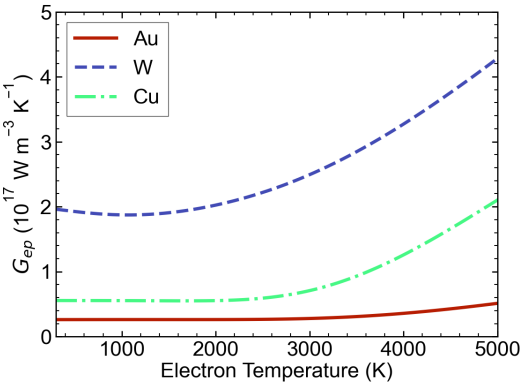

Figure S5: Temperature dependence of the electron-phonon coupling for gold, tungsten, and copper, retrieved from Ref. [137].

Table A.1: Transverse, longitudinal, and Debye sound speeds for each metal film, retrieved from Ref. [266].

	u_T (m/s)	u_L (m/s)	C_s (m/s)
Au	1200	3240	1362
W	2890	5220	3219
Cu	2325	4760	2611

A.7 Section C: Optical Constants of Dielectric Substrates

The isotropic dielectric function of 3C-SiC as well as the ordinary and extraordinary dielectric functions of hBN were simulated using the "TOLO" model as:

$$\varepsilon(\omega) = \varepsilon_\infty \left(\frac{\omega_{\mathrm{LO}} - \omega^2 - i\Gamma}{\omega_{\mathrm{TO}} - \omega^2 - i\Gamma} \right) \tag{S1}$$

where ε_∞, Γ, ω_{LO}, and ω_{TO} represent the high-frequency limit to permittivity, phonon dampening, and longitudinal and transverse optical phonon frequencies, respectively. The values of these parameters for SiC and hBN were retrieved from Refs. [64] and [193] as listed in Table S2. For the silicon substrate, which does not support polaritonic absorption, the tabulated values of dielectric function found in *Palik's Handbook of Optical Constants* [64] were used. The dielectric functions of these substrates, used in radiative heat flux calculations, are plotted in Fig. S6.

Table A.2: Optical constants for the dielectric substrates presented in the main text retrieved from Refs. [64] and [193].

	ε_∞	ω_{TO} [cm^{-1}]	ω_{LO} [cm^{-1}]	Γ [cm^{-1}]
3C-SiC [64]	6.7	969	793	4.8
hBN - Ordinary [193]	4.79	1617	1363	7.3
hBN - Extraordinary [193]	2.95	825	760	7.3

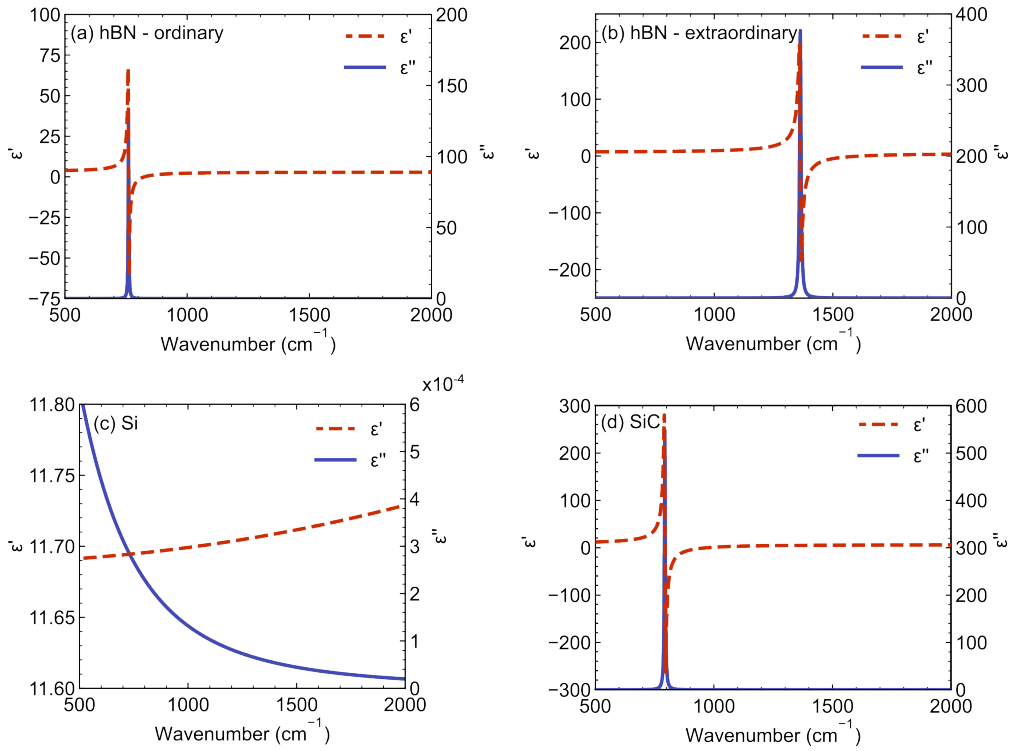

Figure S6: The dielectric functions of (a) hBN in ordinary direction, (b) hBN in extraordinary direction, (c) silicon, and (d) silicon carbide.

A.8 Section D: Sensitivity of h_{rad} to electronic properties

The possible avenues for controlling radiative heat transfer at a metal/insulator interface can be explored through a sensitivity analysis. Fig. S7 describes the sensitivity to each Drude parameter in the case of Au on hBN calculated by computing the change in flux for a ten percent increase in each parameter. Among all, ω_p has the strongest effect on the overall evanescent flux which causes a $\sim$15% decrease in the flux across the interface. This strong impact is a result of the increase in available photonic modes across the interface due to the significant changes in the real part of the dielectric function with changing the plasma frequency. The scattering terms increase the total flux available in the same way, i.e., more scattering in the metal results in a broader Drude peak. The effect of increasing the thickness is that the electrons scatter less with the interface and thus, Γ_{eb} decreases narrowing the breadth of the Drude peak.

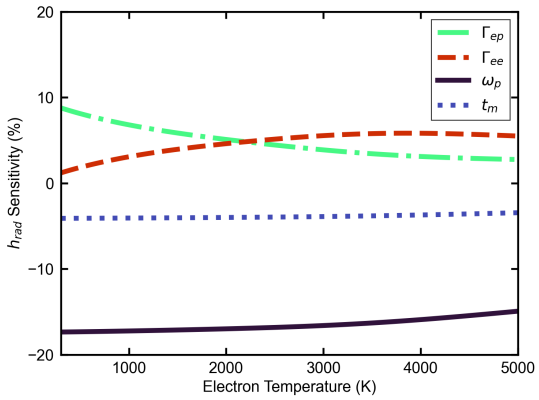

Figure S7: Sensitivity of h_{rad} versus T_e to each electronic property of the Drude model found for the case of Au/hBN.

Bibliography

[1] J. C. Ho, R. Yerushalmi, G. Smith, P. Majhi, J. Bennett, J. Halim, V. N. Faifer, and A. Javey, "Wafer-Scale, Sub-5 nm Junction Formation by Monolayer Doping and Conventional Spike Annealing," *Nano Lett.*, vol. 9, no. 2, pp. 725–730, Feb. 2009, Publisher: American Chemical Society.

[2] G. Basile, A. Bergamin, G. Cavagnero, G. Mana, E. Vittone, and G. Zosi, "Silicon lattice constant: Limits in IMGC X-ray/optical interferometry," en, *IEEE Trans. Instrum. Meas.*, vol. 40, no. 2, pp. 98–102, Apr. 1991.

[3] P. Becker, K. Dorenwendt, G. Ebeling, R. Lauer, W. Lucas, R. Probst, H.-J. Rademacher, G. Reim, P. Seyfried, and H. Siegert, "Absolute Measurement of the (220) Lattice Plane Spacing in a Silicon Crystal," *Phys. Rev. Lett.*, vol. 46, no. 23, pp. 1540–1543, Jun. 1981, Publisher: American Physical Society.

[4] D. G. Cahill, W. K. Ford, K. E. Goodson, G. D. Mahan, A. Majumdar, H. J. Maris, R. Merlin, and S. R. Phillpot, "Nanoscale thermal transport," *Journal of Applied Physics*, vol. 93, no. 2, pp. 793–818, Jan. 2003.

[5] R. Schaller, "Moore's law: Past, present and future," *IEEE Spectr.*, vol. 34, no. 6, pp. 52–59, Jun. 1997.

[6] F. P. Incropera, D. P. DeWitt, T. L. Bergman, and A. S. Lavine, Eds., *Fundamentals of heat and mass transfer*, en, 6. ed. Hoboken, NJ: Wiley, 2007.

[7] G. Chen, *Nanoscale Energy Transport and Conversion: A Parallel Treatment of Electrons, Molecules, Phonons, and Photons* (MIT-Pappalardo Series in Mechanical Engineering). Oxford, New York: Oxford University Press, Mar. 2005.

[8] D. G. Cahill, P. V. Braun, G. Chen, D. R. Clarke, S. Fan, K. E. Goodson, P. Keblinski, W. P. King, G. D. Mahan, A. Majumdar, H. J. Maris, S. R. Phillpot, E. Pop, and L. Shi, "Nanoscale thermal transport. II. 20032012," en, *Applied Physics Reviews*, vol. 1, no. 1, p. 011 305, Mar. 2014.

[9] C. Tien, A. Majumdar, and F. Gerner, "Microscale energy transport," 1998.

[10] A. Majumdar, "Microscale Heat Conduction in Dielectric Thin Films," en, *Journal of Heat Transfer*, vol. 115, no. 1, pp. 7–16, Feb. 1993.

[11] A. N. Smith and J. P. Calame, "Impact of Thin Film Thermophysical Properties on Thermal Management of Wide Bandgap Solid-State Transistors," en, *International Journal of Thermophysics*, vol. 25, no. 2, pp. 409–422, Mar. 2004.

[12] R. Trew, "SiC and GaN transistors - is there one winner for microwave power applications?" *Proceedings of the IEEE*, vol. 90, no. 6, pp. 1032–1047, Jun. 2002, Conference Name: Proceedings of the IEEE.

[13] A. Majumdar, K. Fushinobu, and K. Hijikata, "Effect of gate voltage on hot-electron and hot phonon interaction and transport in a submicrometer transistor," en, *Journal of Applied Physics*, vol. 77, no. 12, pp. 6686–6694, Jun. 1995.

[14] R. Clarke and J. Palmour, "SiC microwave power technologies," *Proceedings of the IEEE*, vol. 90, no. 6, pp. 987–992, Jun. 2002, Conference Name: Proceedings of the IEEE.

[15] A. Garca, J. Monsalve-Serrano, R. Lago Sari, and S. Martinez-Boggio, "An optical investigation of thermal runaway phenomenon under thermal abuse conditions," *Energy Conversion and Management*, vol. 246, p. 114 663, Oct. 2021.

[16] P. G. Emma and E. Kursun, "Is 3D chip technology the next growth engine for performance improvement?" *IBM Journal of Research and Development*, vol. 52, no. 6, pp. 541–552, Nov. 2008, Conference Name: IBM Journal of Research and Development.

[17] S. M. Sze, Y. Li, and K. K. Ng, *Physics of Semiconductor Devices*, en. John Wiley & Sons, Mar. 2021, Google-Books-ID: svYkEAAAQBAJ.

[18] D. Josell, S. H. Brongersma, and Z. Tkei, "Size-Dependent Resistivity in Nanoscale Interconnects," en, *Annu. Rev. Mater. Res.*, vol. 39, no. 1, pp. 231–254, Aug. 2009.

[19] K.-Y. Lee, T.-S. Oh, J.-H. Lee, and T.-S. Oh, "Electrical Characteristics of the Three-Dimensional Interconnection Structure for the Chip Stack Package with Cu through Vias," en, *J. Electron. Mater.*, vol. 36, no. 2, pp. 123–128, Feb. 2007.

[20] C. R. Otey, W. T. Lau, and S. Fan, "Thermal Rectification through Vacuum," en, *Phys. Rev. Lett.*, vol. 104, no. 15, p. 154 301, Apr. 2010.

[21] S. Basu and M. Francoeur, "Near-field radiative transfer based thermal rectification using doped silicon," *Applied Physics Letters*, vol. 98, no. 11, 2011, Publisher: AIP Publishing.

[22] H. Iizuka and S. Fan, "Rectification of evanescent heat transfer between dielectric-coated and uncoated silicon carbide plates," *Journal of Applied Physics*, vol. 112, no. 2, 2012, Publisher: AIP Publishing.

[23] L. P. Wang and Z. M. Zhang, "Thermal Rectification Enabled by Near-Field Radiative Heat Transfer Between Intrinsic Silicon and a Dissimilar Material," *Nanoscale and Microscale Thermophysical Engineering*, vol. 17, no. 4, pp. 337–348, Nov. 2013, Publisher: Taylor & Francis _eprint: https://doi.org/10.1080/15567265.2013.776154.

[24] A. Narayanaswamy and G. Chen, "Surface modes for near field thermophotovoltaics," *Applied Physics Letters*, vol. 82, no. 20, pp. 3544–3546, May 2003.

[25] M. Laroche, R. Carminati, and J.-J. Greffet, "Near-field thermophotovoltaic energy conversion," en, *Journal of Applied Physics*, vol. 100, no. 6, p. 063 704, Sep. 2006.

[26] E. M. Tennyson, C. Gong, and M. S. Leite, "Imaging Energy Harvesting and Storage Systems at the Nanoscale," en, *ACS Energy Lett.*, vol. 2, no. 12, pp. 2761–2777, Dec. 2017.

[27] M. Francoeur, R. Vaillon, and M. P. Meng, "Thermal Impacts on the Performance of Nanoscale-Gap Thermophotovoltaic Power Generators," *IEEE Transactions on Energy Conversion*, vol. 26, no. 2, pp. 686–698, Jun. 2011, Conference Name: IEEE Transactions on Energy Conversion.

[28] P. Sabbaghi, Y. Yang, J.-Y. Chang, and L. Wang, "Near-field thermophotovoltaic energy conversion by excitation of magnetic polariton inside nanometric vacuum gaps with nanostructured Drude emitter and backside reflector," *Journal of Quantitative Spectroscopy and Radiative Transfer*, vol. 234, pp. 108–114, Sep. 2019.

[29] R. Mittapally, B. Lee, L. Zhu, A. Reihani, J. W. Lim, D. Fan, S. R. Forrest, P. Reddy, and E. Meyhofer, "Near-field thermophotovoltaics for efficient heat to electricity conversion at high power density," en, *Nat Commun*, vol. 12, no. 1, p. 4364, Jul. 2021, Publisher: Nature Publishing Group.

[30] J. Stefan, *ber die Beziehung zwischen der Wrmestrahlung und der Temperatur*, de. Aus der k.k. Hof-und Staatsdruckerei, 1879, Google-Books-ID: Rpy1PgAACAAJ.

[31] C. Kittel, *Introduction to Solid State Physics*. New York: Jhon Wiley & Sons, 1996.

[32] J.-J. Greffet, R. Carminati, K. Joulain, J.-P. Mulet, S. Mainguy, and Y. Chen, "Coherent emission of light by thermal sources," *Nature*, vol. 416, no. 6876, pp. 61–64, 2002.

[33] S. Zare, "Engineering the Spectrum of Near-Field Thermal Radiation," en,

[34] T. J. Coutts and M. C. Fitzgerald, "Thermophotovoltaics," *Scientific American*, vol. 279, no. 3, pp. 90–95, 1998, Publisher: Scientific American, a division of Nature America, Inc.

[35] S. Y. Lin, J. Moreno, and J. G. Fleming, "Three-dimensional photonic-crystal emitter for thermal photovoltaic power generation," *Applied Physics Letters*, vol. 83, no. 2, pp. 380–382, Jul. 2003.

[36] R. L. Cummerow, "Photovoltaic Effect in pn Junctions," in *Renewable Energy*, Routledge, 2011.

[37] H. Salihoglu, W. Nam, L. Traverso, M. Segovia, P. K. Venuthurumilli, W. Liu, Y. Wei, W. Li, and X. Xu, "Near-Field Thermal Radiation between Two Plates with Sub-10 nm Vacuum Separation," *Nano Lett.*, vol. 20, no. 8, pp. 6091–6096, Aug. 2020, Publisher: American Chemical Society.

[38] X. Liu, L. Wang, and Z. M. Zhang, "Near-Field Thermal Radiation: Recent Progress and Outlook," en, *Nanoscale and Microscale Thermophysical Engineering*, vol. 19, no. 2, pp. 98–126, Apr. 2015.

[39] A. Einstein, "Die Plancksche Theorie der Strahlung und die Theorie der spezifischen Wrme," en, *Annalen der Physik*, vol. 327, no. 1, pp. 180–190, 1907.

[40] M. Planck, "Nobel Prize in Physics 1918," en-US, Lecture, Jun. 1920.

[41] L. Brillouin, *Wave Propagation and Group Velocity*, en. Academic Press, Oct. 2013, Google-Books-ID: gdQ3BQAAQBAJ.

[42] G. P. Srivastava, *The Physics of Phonons*, 2nd ed. Boca Raton: CRC Press, Sep. 2022.

[43] H. A. Lorentz, *The Theory of Electrons and Its Applications to the Phenomena of Light and Radiant Heat: A Course of Lectures Delivered in Columbia University, New York, in March and April, 1906*, en. B.G. Teubner, 1909, Google-Books-ID: DGFDAAAAIAAJ.

[44] Bose, "Plancks Gesetz und Lichtquantenhypothese," de, *Z. Physik*, vol. 26, no. 1, pp. 178–181, Dec. 1924.

[45] N. Mingo, "Calculation of Si nanowire thermal conductivity using complete phonon dispersion relations," *Phys. Rev. B*, vol. 68, no. 11, p. 113 308, Sep. 2003, Publisher: American Physical Society.

[46] Z. Tian, K. Esfarjani, J. Shiomi, A. S. Henry, and G. Chen, "On the importance of optical phonons to thermal conductivity in nanostructures," *Applied Physics Letters*, vol. 99, no. 5, p. 053 122, Aug. 2011.

[47] A. Giri and P. E. Hopkins, "Achieving a better heat conductor," *Nature Materials 2020 19:5*, vol. 19, no. 5, pp. 482–484, Apr. 2020, Publisher: Nature Publishing Group.

[48] E. Schrdinger, "Quantisierung als Eigenwertproblem," en, *Annalen der Physik*, vol. 384, no. 4, pp. 361–376, 1926.

[49] D. J. Griffiths and D. F. Schroeter, *Introduction to Quantum Mechanics*, en. Cambridge University Press, Aug. 2018, Google-Books-ID: LWRnDwAAQBAJ.

[50] P. Giannozzi, S. Baroni, N. Bonini, M. Calandra, R. Car, C. Cavazzoni, D. Ceresoli, G. L. Chiarotti, M. Cococcioni, I. Dabo, A. Dal Corso, S. De Gironcoli, S. Fabris, G. Fratesi, R. Gebauer, U. Gerstmann, C. Gougoussis, A. Kokalj, M. Lazzeri, L. Martin-Samos, N. Marzari, F. Mauri, R. Mazzarello, S. Paolini, A. Pasquarello, L. Paulatto, C. Sbraccia, S. Scandolo, G. Sclauzero, A. P. Seitsonen, A. Smogunov, P. Umari, and R. M. Wentzcovitch, "QUANTUM ESPRESSO: A modular and open-source software project for quantum simulations of materials," en, *J. Phys.: Condens. Matter*, vol. 21, no. 39, p. 395 502, Sep. 2009.

[51] J. Fischer and M. Wendland, "On the history of key empirical intermolecular potentials," *Fluid Phase Equilibria*, vol. 573, p. 113 876, Oct. 2023.

[52] F. Bloch, "Ber die Quantenmechanik der Elektronen in Kristallgittern," de, *Z. Physik*, vol. 52, no. 7, pp. 555–600, Jul. 1929.

[53] *Pauli: Ber den Zusammenhang des Abschlusses der... - Google Scholar.*

[54] A. Zannoni, *On the Quantization of the Monoatomic Ideal Gas*, arXiv:cond-mat/9912229, Dec. 1999.

[55] *The Theory of Electrons and Its Applications to the Phenomena of Light and Radiant Heat (Paperback) | Harvard Book Store*, en.

[56] E. A. Desloge and S. W. Matthysse, "Collision Term in the Boltzmann Transport Equation," en, *American Journal of Physics*, vol. 28, no. 1, pp. 1–11, Jan. 1960.

[57] V. Gasparov and R. Huguenin, "Electron-phonon, electron-electron and electron-surface scattering in metals from ballistic effects," en, *Advances in Physics*, vol. 42, no. 4, pp. 393–521, Aug. 1993.

[58] M. I. Kaganov, E. M. Lifshitz, and L. V. Tanatarov, "Relaxation between electrons and the crystalline lattice," *Soviet Physics-JETP*, vol. 4, pp. 173–178, 1957.

[59] J. C. Maxwell, d. D. Burndy Library, and Royal Society (Great Britain), *A dynamical theory of the electromagnetic field*, eng. [London : The Royal Society], 1865.

[60] N. W. Ashcroft and N. D. Mermin, *Solid State Physics*, en. Holt, Rinehart and Winston, 1976, Google-Books-ID: 1C9HAQAAIAAJ.

[61] *Principles of Statistical Radiophysics 4*, en.

[62] P. Drude, "Zur Elektronentheorie der Metalle," en, *Annalen der Physik*, vol. 306, no. 3, pp. 566–613, 1900, _eprint: https://onlinelibrary.wiley.com/doi/pdf/10.1002/andp.19003060312.

[63] E. Silaeva, L. Saddier, and J.-P. Colombier, "Drude-Lorentz Model for Optical Properties of Photoexcited Transition Metals under Electron-Phonon Nonequilibrium," en, *Applied Sciences*, vol. 11, no. 21, p. 9902, Jan. 2021, Number: 21 Publisher: Multidisciplinary Digital Publishing Institute.

[64] E. D. Palik, *Handbook of Optical Constants of Solids*, en. Academic Press, 1998, Google-Books-ID: nxoqxyoHfbIC.

[65] K. Joulain, J.-P. Mulet, F. Marquier, R. Carminati, and J.-J. Greffet, "Surface electromagnetic waves thermally excited: Radiative heat transfer, coherence properties and Casimir forces revisited in the near field," *Surface Science Reports*, vol. 57, no. 3, pp. 59–112, May 2005.

[66] M. Francoeur, M. Pinar Meng, and R. Vaillon, "Solution of near-field thermal radiation in one-dimensional layered media using dyadic Green's functions and the scattering matrix method," *Journal of Quantitative Spectroscopy and Radiative Transfer*, vol. 110, no. 18, pp. 2002–2018, 2009, Publisher: Elsevier Ltd.

[67] S. M. Rytov, I. A. Kravtsov, and V. I. Tatarskii, *Principles of Statistical Radiophysics*, en. Springer-Verlag, 1987, Google-Books-ID: crZPAAAAYAAJ.

[68] *Classical Electrodynamics Third Edition: Jackson, John David: 9780471309321: Amazon.com: Books.*

[69] E. T. Swartz and R. O. Pohl, "Thermal boundary resistance," *Reviews of Modern Physics*, vol. 61, no. 3, pp. 605–688, 1989, Publisher: American Physics Society.

[70] E. R. Hoglund, D.-L. Bao, A. OHara, S. Makarem, Z. T. Piontkowski, J. R. Matson, A. K. Yadav, R. C. Haislmaier, R. Engel-Herbert, J. F. Ihlefeld, J. Ravichandran, R. Ramesh, J. D. Caldwell, T. E. Beechem, J. A. Tomko, J. A. Hachtel, S. T. Pantelides, P. E. Hopkins, and J. M. Howe, "Emergent interface vibrational structure of oxide superlattices," en, *Nature*, vol. 601, no. 7894, pp. 556–561, Jan. 2022, Publisher: Nature Publishing Group.

[71] A. V. Sergeev, "Electronic Kapitza conductance due to inelastic electron-boundary scattering," en, *Phys. Rev. B*, vol. 58, no. 16, R10199–R10202, Oct. 1998.

[72] W. G. Vincenti and C. H. Kruger, *Introduction to Physical Gas Dynamics*, en. Wiley, 1965, Google-Books-ID: rvlQAAAAMAAJ.

[73] A. Giri, B. M. Foley, and P. E. Hopkins, "Influence of Hot Electron Scattering and Electron-Phonon Interactions on Thermal Boundary Conductance at Metal/Nonmetal Interfaces," *Journal of Heat Transfer*, vol. 136, no. 092401, Jun. 2014.

[74] T. Q. Qiu and C. L. Tien, "Size Effects on Nonequilibrium Laser Heating of Metal Films," *Journal of Heat Transfer*, vol. 115, no. 4, pp. 842–847, Nov. 1993.

[75] P. E. Hopkins, P. M. Norris, and R. J. Stevens, "Influence of inelastic scattering at metal-dielectric interfaces," *Journal of Heat Transfer*, vol. 130, no. 2, Feb. 2008.

[76] R. J. Stoner and H. J. Maris, "Kapitza conductance and heat flow between solids at temperatures from 50 to 300 K," *Phys. Rev. B*, vol. 48, no. 22, pp. 16 373–16 387, Dec. 1993, Publisher: American Physical Society.

[77] R. E. Prange and L. P. Kadanoff, "Transport Theory for Electron-Phonon Interactions in Metals," *Phys. Rev.*, vol. 134, no. 3A, A566–A580, May 1964, Publisher: American Physical Society.

[78] E. Y. Wilner, H. Wang, M. Thoss, and E. Rabani, "Nonequilibrium quantum systems with electron-phonon interactions: Transient dynamics and approach to steady state," *Phys. Rev. B*, vol. 89, no. 20, p. 205 129, May 2014, Publisher: American Physical Society.

[79] W. J. Scouler, "Temperature-Modulated Reflectance of Gold from 2 to 10 eV," *Phys. Rev. Lett.*, vol. 18, no. 12, pp. 445–448, Mar. 1967, Publisher: American Physical Society.

[80] C. A. Paddock and G. L. Eesley, "Transient thermoreflectance from thin metal films," *Journal of Applied Physics*, vol. 60, no. 1, pp. 285–290, Jul. 1986.

[81] A. J. Schmidt, R. Cheaito, and M. Chiesa, "A frequency-domain thermoreflectance method for the characterization of thermal properties," *Rev. Sci. Instrum*, vol. 80, p. 94 901, 2009, ISBN: 0949012009.

[82] J. L. Braun, D. H. Olson, J. T. Gaskins, and P. E. Hopkins, "A steady-state thermoreflectance method to measure thermal conductivity," *Review of Scientific Instruments*, vol. 90, no. 2, p. 024 905, Feb. 2019, Publisher: AIP Publishing LLC AIP Publishing.

[83] D. G. Cahill, "Analysis of heat flow in layered structures for time-domain thermoreflectance," *Review of Scientific Instruments*, vol. 75, no. 12, pp. 5119–5122, Dec. 2004.

[84] R. L. Olmon, B. Slovick, T. W. Johnson, D. Shelton, S.-H. Oh, G. D. Boreman, and M. B. Raschke, "Optical dielectric function of gold," *Phys. Rev. B*, vol. 86, no. 23, p. 235 147, Dec. 2012, Publisher: American Physical Society.

[85] H. U. Yang, J. D'Archangel, M. L. Sundheimer, E. Tucker, G. D. Boreman, and M. B. Raschke, "Optical dielectric function of silver," *Phys. Rev. B*, vol. 91, no. 23, p. 235 137, Jun. 2015, Publisher: American Physical Society.

[86] R. M. A. Azzam, *Ellipsometry and polarized light*, eng. Amsterdam ; New York : North-Holland Pub. Co. ; New York : sole distributors for the U.S.A. and Canada, Elsevier North-Holland, 1977.

[87] *Principles of Optics: Electromagnetic Theory of Propagation, Interference and Diffraction of Light: Born, Max, Wolf, Emil, Bhatia, A. B., Clemmow, P. C., Gabor, D., Stokes, A. R., Taylor, A. M., Wayman, P. A., Wilcock, W. L.: 9780521642224: Amazon.com: Books.*

[88] J. A. Woollam, B. D. Johs, C. M. Herzinger, J. N. Hilfiker, R. A. Synowicki, and C. L. Bungay, "Overview of variable-angle spectroscopic ellipsometry (VASE): I. Basic theory and typical applications," in *Optical Metrology: A Critical Review*, vol. 10294, SPIE, Jul. 1999, pp. 3–28.

[89] M. Hilse, X. Wang, P. Killea, F. Peiris, and R. Engel-Herbert, "Spectroscopic ellipsometry as an in-situ monitoring tool for Bi2Se3 films grown by molecular beam epitaxy," *Journal of Crystal Growth*, vol. 566–567, p. 126 177, Jul. 2021.

[90] M. Born and R. Oppenheimer, "Zur Quantentheorie der Molekeln," en, *Annalen der Physik*, vol. 389, no. 20, pp. 457–484, 1927.

[91] P. Hohenberg and W. Kohn, "Inhomogeneous Electron Gas," en, *Phys. Rev.*, vol. 136, no. 3B, B864–B871, Nov. 1964.

[92] W. Kohn and L. J. Sham, "Self-Consistent Equations Including Exchange and Correlation Effects," *Phys. Rev.*, vol. 140, no. 4A, A1133–A1138, Nov. 1965, Publisher: American Physical Society.

[93] J. Gerratt and I. M. Mills, "Force Constants and DipoleMoment Derivatives of Molecules from Perturbed HartreeFock Calculations. I," *The Journal of Chemical Physics*, vol. 49, no. 4, pp. 1719–1729, Aug. 1968.

[94] S. Baroni, S. de Gironcoli, A. Dal Corso, and P. Giannozzi, "Phonons and related crystal properties from density-functional perturbation theory," *Rev. Mod. Phys.*, vol. 73, no. 2, pp. 515–562, Jul. 2001, Publisher: American Physical Society.

[95] M. J. van Setten, M. Giantomassi, E. Bousquet, M. J. Verstraete, D. R. Hamann, X. Gonze, and G. M. Rignanese, "The PseudoDojo: Training and grading a 85 element optimized norm-conserving pseudopotential table," *Computer Physics Communications*, vol. 226, pp. 39–54, May 2018.

[96] S. Anisimov, B. Kapeliovich, and T. Perel'man, "Electron emission from the metal surfaces induced by ultrashort lasers pulses," *Zhurnal Ehksperimental'noj i Teoreticheskoj Fiziki*, Ehlektronnaya ehmissiya s poverkhnosti metallov pod dejstviem ul'trakorotkikh lazernykh impul'sov, vol. 66, no. 2, pp. 776–781, 1974, Place: USSR INIS Reference Number: 5131223.

[97] J. K. Chen, D. Y. Tzou, and J. E. Beraun, "A semiclassical two-temperature model for ultrafast laser heating," *International Journal of Heat and Mass Transfer*, vol. 49, no. 1, pp. 307–316, Jan. 2006.

[98] Y. Ishida, T. Togashi, K. Yamamoto, M. Tanaka, T. Taniuchi, T. Kiss, M. Nakajima, T. Suemoto, and S. Shin, "Non-thermal hot electrons ultrafastly generating hot optical phonons in graphite," en, *Sci Rep*, vol. 1, no. 1, p. 64, Aug. 2011, Publisher: Nature Publishing Group.

[99] S. Sinha, E. Pop, R. W. Dutton, and K. E. Goodson, "Non-equilibrium phonon distributions in sub-100 nm silicon transistors," 2006.

[100] F. Murphy-Armando, D. Murray, I. Savi, M. Trigo, D. A. Reis, and S. Fahy, "Electronic heat generation in semiconductors: Non-equilibrium excitation and evolution of zone-edge phonons via electronphonon scattering in photo-excited germanium," *Applied Physics Letters*, vol. 122, no. 1, p. 012 202, Jan. 2023.

[101] V. V. Kabanov, "Electron-electron and electron-phonon relaxation in metals excited by optical pulse," en, *Low Temperature Physics*, vol. 46, no. 4, pp. 414–419, Apr. 2020, arXiv:2002.04343 [cond-mat].

[102] W. Park, A. Sood, J. Park, M. Asheghi, R. Sinclair, and K. E. Goodson, "Enhanced Thermal Conduction Through Nanostructured Interfaces," en, *Nanoscale and Microscale Thermophysical Engineering*, vol. 21, no. 3, pp. 134–144, Jul. 2017.

[103] F. Caruso and D. Novko, "Ultrafast dynamics of electrons and phonons: From the two-temperature model to the time-dependent Boltzmann equation," en, *Advances in Physics: X*, vol. 7, no. 1, p. 2 095 925, Dec. 2022.

[104] G. W. Recktenwald, "Finite-Dierence Approximations to the Heat Equation," en,

[105] M. Auslender and S. Hava, "Scattering-matrix propagation algorithm in full-vectorial optics of multilayer grating structures," EN, *Opt. Lett., OL*, vol. 21, no. 21, pp. 1765–1767, Nov. 1996, Publisher: Optica Publishing Group.

[106] N. P. K. Cotter, T. W. Preist, and J. R. Sambles, "Scattering-matrix approach to multilayer diffraction," EN, *J. Opt. Soc. Am. A, JOSAA*, vol. 12, no. 5, pp. 1097–1103, May 1995, Publisher: Optica Publishing Group.

[107] J. Hao and L. Zhou, "Electromagnetic wave scatterings by anisotropic metamaterials: Generalized 44 transfer-matrix method," *Physical Review B - Condensed Matter and Materials Physics*, vol. 77, no. 9, Mar. 2008.

[108] N. C. Passler and A. Paarmann, "Generalized 4 4 matrix formalism for light propagation in anisotropic stratified media: Study of surface phonon polaritons in polar dielectric heterostructures," *Journal of the Optical Society of America B*, vol. 34, no. 10, p. 2128, Oct. 2017, arXiv: 1707.00462 Publisher: The Optical Society.

[109] W. Xu, L. T. Wood, and T. D. Golding, "Optical degeneracies in anisotropic layered media: Treatment of singularities in a 4\ifmmode\times\else\texttimes\fi{}4 matrix formalism," *Phys. Rev. B*, vol. 61, no. 3, pp. 1740–1743, Jan. 2000, Publisher: American Physical Society.

[110] D. W. Berreman, "Optics in Stratified and Anisotropic Media: 44-Matrix Formulation," EN, *J. Opt. Soc. Am., JOSA*, vol. 62, no. 4, pp. 502–510, Apr. 1972, Publisher: Optica Publishing Group.

[111] P. Yeh, "Electromagnetic propagation in birefringent layered media," EN, *J. Opt. Soc. Am., JOSA*, vol. 69, no. 5, pp. 742–756, May 1979, Publisher: Optica Publishing Group.

[112] P. E. Hopkins, "Thermal Transport across Solid Interfaces with Nanoscale Imperfections: Effects of Roughness, Disorder, Dislocations, and Bonding on Thermal Boundary Conductance," en, *ISRN Mechanical Engineering*, vol. 2013, pp. 1–19, Jan. 2013.

[113] A. Giri and P. E. Hopkins, "A Review of Experimental and Computational Advances in Thermal Boundary Conductance and Nanoscale Thermal Transport across Solid Interfaces," *Advanced Functional Materials*, vol. 30, no. 8, p. 21, Feb. 2020, Publisher: Wiley-VCH Verlag.

[114] C. Monachon, L. Weber, and C. Dames, "Thermal Boundary Conductance: A Materials Science Perspective," en, *Annu. Rev. Mater. Res.*, vol. 46, no. 1, pp. 433–463, Jul. 2016.

[115] J. Chen, X. Xu, J. Zhou, and B. Li, "Interfacial thermal resistance: Past, present, and future," *Rev. Mod. Phys.*, vol. 94, no. 2, p. 025 002, Apr. 2022, Publisher: American Physical Society.

[116] A. Giri, S. G. Walton, J. Tomko, N. Bhatt, M. J. Johnson, D. R. Boris, G. Lu, J. D. Caldwell, O. V. Prezhdo, and P. E. Hopkins, "Ultrafast and Nanoscale Energy Transduction Mechanisms and Coupled Thermal Transport across Interfaces," en, *ACS Nano*, vol. 17, no. 15, pp. 14 253–14 282, Aug. 2023.

[117] S.-A. Biehs, M. Tschikin, and P. Ben-Abdallah, "Hyperbolic Metamaterials as an Analog of a Blackbody in the Near Field," en, *Phys. Rev. Lett.*, vol. 109, no. 10, p. 104 301, Sep. 2012.

[118] Y. Guo and Z. Jacob, "Fluctuational electrodynamics of hyperbolic metamaterials," *Journal of Applied Physics*, vol. 115, no. 23, p. 234 306, Jun. 2014.

[119] A. Principi, M. B. Lundeberg, N. C. Hesp, K. J. Tielrooij, F. H. Koppens, and M. Polini, "Super-Planckian Electron Cooling in a van der Waals Stack," *Physical Review Letters*, vol. 118, no. 12, Mar. 2017, arXiv: 1608.01516 Publisher: American Physical Society.

[120] E. G. Cravalho, C. L. Tien, and R. P. Caren, "Effect of Small Spacings on Radiative Transfer Between Two Dielectrics," *Journal of Heat Transfer*, vol. 89, no. 4, pp. 351–358, Nov. 1967.

[121] V. Chiloyan, J. Garg, K. Esfarjani, and G. Chen, "Transition from near-field thermal radiation to phonon heat conduction at sub-nanometre gaps," en, *Nat Commun*, vol. 6, no. 1, p. 6755, Apr. 2015, Publisher: Nature Publishing Group.

[122] J. Zhang, K. Shi, L. Lu, D. Feng, H. Liu, and X. Wu, "Experiments on near-field radiative heat transfer: A review," en, *CEST*, vol. 1, no. 1, Sep. 2023.

[123] M. Ghashami, A. Jarzembski, M. Lim, B. J. Lee, and K. Park, "Experimental exploration of near-field radiative heat transfer," English, in *Annual Review of Heat Transfer*, Begell House Inc., 2020, pp. 13–58.

[124] A. Lenert, D. M. Bierman, Y. Nam, W. R. Chan, I. Celanovi, M. Soljai, and E. N. Wang, "A nanophotonic solar thermophotovoltaic device," en, *Nature Nanotech*, vol. 9, no. 2, pp. 126–130, Feb. 2014.

[125] W. A. Challener, C. Peng, A. V. Itagi, D. Karns, W. Peng, Y. Peng, X. Yang, X. Zhu, N. J. Gokemeijer, Y.-T. Hsia, G. Ju, R. E. Rottmayer, M. A. Seigler, and E. C. Gage, "Heat-assisted magnetic recording by a near-field transducer with efficient optical energy transfer," en, *Nature Photon*, vol. 3, no. 4, pp. 220–224, Apr. 2009.

[126] B. C. Stipe, T. C. Strand, C. C. Poon, H. Balamane, T. D. Boone, J. A. Katine, J.-L. Li, V. Rawat, H. Nemoto, A. Hirotsune, O. Hellwig, R. Ruiz, E. Dobisz, D. S. Kercher, N. Robertson, T. R. Albrecht, and B. D. Terris, "Magnetic recording at 1.5 Pb m2 using an integrated plasmonic antenna," en, *Nature Photon*, vol. 4, no. 7, pp. 484–488, Jul. 2010.

[127] Y. De Wilde, F. Formanek, R. Carminati, B. Gralak, P.-A. Lemoine, K. Joulain, J.-P. Mulet, Y. Chen, and J.-J. Greffet, "Thermal radiation scanning tunnelling microscopy," en, *Nature*, vol. 444, no. 7120, pp. 740–743, Dec. 2006.

[128] A. Kittel, U. F. Wischnath, J. Welker, O. Huth, F. Rting, and S.-A. Biehs, "Near-field thermal imaging of nanostructured surfaces," *Applied Physics Letters*, vol. 93, no. 19, p. 193 109, Nov. 2008.

[129] A. C. Jones, B. T. OCallahan, H. U. Yang, and M. B. Raschke, "The thermal near-field: Coherence, spectroscopy, heat-transfer, and optical forces," en, *Progress in Surface Science*, vol. 88, no. 4, pp. 349–392, Dec. 2013.

[130] R. Carminati and J.-J. Greffet, "Near-Field Effects in Spatial Coherence of Thermal Sources," *Phys. Rev. Lett.*, vol. 82, no. 8, pp. 1660–1663, Feb. 1999, Publisher: American Physical Society.

[131] J.-P. Mulet, K. Joulain, R. Carminati, and J.-J. Greffet, "Enhanced Radiative Heat Transfer at Nanometric Distances," *Microscale Thermophysical Engineering*, vol. 6, no. 3, pp. 209–222, Jul. 2002, Publisher: Taylor & Francis _eprint: https://doi.org/10.1080/10893950290053321.

[132] H. Iizuka and S. Fan, "Analytical treatment of near-field electromagnetic heat transfer at the nanoscale," *Phys. Rev. B*, vol. 92, no. 14, p. 144 307, Oct. 2015, Publisher: American Physical Society.

[133] M. Francoeur, M. P. Meng, and R. Vaillon, "Spectral tuning of near-field radiative heat flux between two thin silicon carbide films," en, *J. Phys. D: Appl. Phys.*, vol. 43, no. 7, p. 075 501, Feb. 2010.

[134] E. Minamitani, "Ab initio analysis for the initial process of Joule heating in semiconductors," *Phys. Rev. B*, vol. 104, no. 8, p. 085 202, Aug. 2021, Publisher: American Physical Society.

[135] W. Cai, M. C. Marchetti, and M. Lax, "Nonequilibrium electron-phonon scattering in semiconductor heterojunctions," en, *Phys. Rev. B*, vol. 34, no. 12, pp. 8573–8580, Dec. 1986.

[136] K. Krl, "Electrophonon resonance in Al x Ga 1 - x As-GaAs quasi-two-dimensional quantum wells," *Phys. Rev. B*, vol. 50, no. 11, pp. 7640–7654, Sep. 1994, Publisher: American Physical Society.

[137] Z. Lin, L. V. Zhigilei, and V. Celli, "Electron-phonon coupling and electron heat capacity of metals under conditions of strong electron-phonon nonequilibrium," en, *Phys. Rev. B*, vol. 77, no. 7, p. 075 133, Feb. 2008.

[138] A. Giri, M. V. Tokina, O. V. Prezhdo, and P. E. Hopkins, "Electronphonon coupling and related transport properties of metals and intermetallic alloys from first principles," *Materials Today Physics*, vol. 12, p. 100 175, Mar. 2020.

[139] A. Giri, J. T. Gaskins, B. M. Foley, R. Cheaito, and P. E. Hopkins, "Experimental evidence of excited electron number density and temperature effects on electron-phonon coupling in gold films," en, *Journal of Applied Physics*, vol. 117, no. 4, p. 044 305, Jan. 2015.

[140] P. E. Hopkins and D. A. Stewart, "Contribution of d-band electrons to ballistic transport and scattering during electron-phonon nonequilibrium in nanoscale Au films using an *ab*

initio density of states," en, *Journal of Applied Physics*, vol. 106, no. 5, p. 053 512, Sep. 2009.

[141] J.-J. Greffet, P. Bouchon, G. Brucoli, and F. Marquier, "Light Emission by Nonequilibrium Bodies: Local Kirchhoff Law," en, *Phys. Rev. X*, vol. 8, no. 2, p. 021 008, Apr. 2018.

[142] M. R. Islam, J. A. Tomko, M. S. B. Hoque, K. Aryana, K. Carver, C. Jezewski, C. Landon, S. King, and P. E. Hopkins, "Measurements of the in-plane thermal conductivity and electron-phonon coupling factor of Cu thin films for evaluation of Matthiessens Rule," *Nature Communications*, 2024.

[143] D. Pines and D. Bohm, "A Collective Description of Electron Interactions: II. Collective vs Individual Particle Aspects of the Interactions," en, *Phys. Rev.*, vol. 85, no. 2, pp. 338–353, Jan. 1952.

[144] J. Hohlfeld, S. S. Wellershoff, J. Gdde, U. Conrad, V. Jhnke, and E. Matthias, "Electron and lattice dynamics following optical excitation of metals," *Chemical Physics*, vol. 251, no. 1-3, pp. 237–258, Jan. 2000, Publisher: North-Holland.

[145] S. Yngvesson, *Microwave Semiconductor Devices*. Boston, MA: Springer US, 1991.

[146] W. Hutchins, S. Zare, D. M. Hirt, J. A. Tomko, J. R. Matson, K. Diaz-Granados, M. Long, M. He, T. Pfeifer, J. Li, J. H. Edgar, J.-P. Maria, J. D. Caldwell, and P. E. Hopkins, "Ultrafast evanescent heat transfer across solid interfaces via hyperbolic phononpolariton modes in hexagonal boron nitride," en, *Nat. Mater.*, pp. 1–9, Mar. 2025, Publisher: Nature Publishing Group.

[147] H. Salihoglu, V. Iyer, T. Taniguchi, K. Watanabe, P. D. Ye, and X. Xu, "Energy Transport by Radiation in Hyperbolic Material Comparable to Conduction," *Advanced Functional Materials*, vol. 30, no. 6, Feb. 2020, Publisher: Wiley-VCH Verlag.

[148] A. J. Giles, S. Dai, I. Vurgaftman, T. Hoffman, S. Liu, L. Lindsay, C. T. Ellis, N. Assefa, I. Chatzakis, T. L. Reinecke, J. G. Tischler, M. M. Fogler, J. H. Edgar, D. N. Basov, and J. D. Caldwell, "Ultralow-loss polaritons in isotopically pure boron nitride," *Nature Materials*, vol. 17, no. 2, pp. 134–139, Feb. 2018, Publisher: Nature Publishing Group.

[149] R. Pouria, P. K. Chow, T. Tiwald, S. Zare, and S. Edalatpour, "Far-field thermal radiation from short-pitch silicon-carbide nanopillar arrays," *Applied Physics Letters*, vol. 121, no. 13, p. 131 702, Sep. 2022.

[150] S. Zare, R. Pouria, P. K. Chow, T. Tiwald, C. P. Tripp, and S. Edalatpour, "Probing Near-Field Thermal Emission of Localized Surface Phonons from Silicon Carbide Nanopillars," *ACS Photonics*, vol. 10, no. 2, pp. 401–411, Feb. 2023, Publisher: American Chemical Society.

[151] S. Zare, C. P. Tripp, and S. Edalatpour, "Measurement of near-field thermal emission spectra using an internal reflection element," en, *Phys. Rev. B*, vol. 100, no. 23, p. 235 450, Dec. 2019.

[152] M. Heiblum and M. V. Fischetti, "Ballistic hot-electron transistors," *IBM Journal of Research and Development*, vol. 34, no. 4, pp. 530–549, Jul. 1990, Conference Name: IBM Journal of Research and Development.

[153] S. Vaziri, A. D. Smith, M. stling, G. Lupina, J. Dabrowski, G. Lippert, W. Mehr, F. Driussi, S. Venica, V. Di Lecce, A. Gnudi, M. Knig, G. Ruhl, M. Belete, and M. C. Lemme, "Going ballistic: Graphene hot electron transistors," *Solid State Communications*, vol. 224, pp. 64–75, Dec. 2015.

[154] B. Yang, B. Song, F. J. G. de Abajo, and Q. Dai, "Ultrafast Thermal Switching Enabled by Transient Polaritons," *ACS Nano*, Dec. 2024, Publisher: American Chemical Society.

[155] N. H. Thomas, M. C. Sherrott, J. Broulliet, H. A. Atwater, and A. J. Minnich, "Electronic Modulation of Near-Field Radiative Transfer in Graphene Field Effect Heterostructures," en, *Nano Lett.*, vol. 19, no. 6, pp. 3898–3904, Jun. 2019.

[156] R. Mittapally, A. Majumder, P. Reddy, and E. Meyhofer, "Near-Field Thermophotovoltaic Energy Conversion: Progress and Opportunities," *Phys. Rev. Appl.*, vol. 19, no. 3, p. 037 002, Mar. 2023, Publisher: American Physical Society.

[157] S. Kim, B. Zhang, Z. Wang, J. Fischer, S. Brodbeck, M. Kamp, C. Schneider, S. Hfling, and H. Deng, "Coherent Polariton Laser," en, *Phys. Rev. X*, vol. 6, no. 1, p. 011 026, Mar. 2016.

[158] R. K. Willardson and A. C. Beer, *Modulation Techniques*, en. Academic Press, 1972, Google-Books-ID: sd8_xR1ZuOwC.

[159] A. J. Schmidt, R. Cheaito, and M. Chiesa, "Characterization of thin metal films via frequency-domain thermoreflectance," en, *Journal of Applied Physics*, vol. 107, no. 2, p. 024 908, Jan. 2010.

[160] D. Hirt, M. R. Islam, M. S. B. Hoque, W. Hutchins, S. Makarem, M. K. Lenox, W. T. Riffe, J. F. Ihlefeld, E. A. Scott, G. Esteves, and P. E. Hopkins, "Increased thermal conductivity and decreased electronphonon coupling factor of the aluminum scandium intermetallic phase (Al3Sc) compared to solid solutions," *Applied Physics Letters*, vol. 124, no. 20, p. 202 202, May 2024.

[161] M. R. Islam, P. Karna, J. A. Tomko, E. R. Hoglund, D. M. Hirt, M. S. B. Hoque, S. Zare, K. Aryana, T. W. Pfeifer, C. Jezewski, A. Giri, C. D. Landon, S. W. King, and P. E. Hopkins, "Evaluating size effects on the thermal conductivity and electron-phonon scattering rates of copper thin films for experimental validation of Matthiessens rule," en, *Nat Commun*, vol. 15, no. 1, p. 9167, Oct. 2024, Publisher: Nature Publishing Group.

[162] M. S. B. Hoque, Y. R. Koh, S. Zare, M. E. Liao, K. Huynh, M. S. Goorsky, Z. Liu, J. Shi, S. Graham, T. Luo, H. Ahmad, W. A. Doolittle, and P. E. Hopkins, "Experimental observation of ballistic to diffusive transition in phonon thermal transport of AlN thin films," *Applied Physics Letters*, vol. 125, no. 26, p. 262 201, Dec. 2024.

[163] K. Aryana, Y. Zhang, J. A. Tomko, M. S. B. Hoque, E. R. Hoglund, D. H. Olson, J. Nag, J. C. Read, C. Ros, J. Hu, and P. E. Hopkins, "Suppressed electronic contribution in thermal conductivity of Ge2Sb2Se4Te," *Nature Communications*, vol. 12, no. 1, Dec. 2021, Publisher: Nature Research.

[164] A. B. Kuzmenko, E. van Heumen, F. Carbone, and D. van der Marel, "Universal Optical Conductance of Graphite," *Phys. Rev. Lett.*, vol. 100, no. 11, p. 117 401, Mar. 2008, Publisher: American Physical Society.

[165] H. Jamgotchian, N. Bergeon, D. Benielli, P. Voge, and B. Billia, "In situ observation and interferometric characterization of solidliquid interface morphology in directionally growing transparent model systems," en, *Journal of Microscopy*, vol. 203, no. 1, pp. 119–127, 2001, _eprint: https://onlinelibrary.wiley.com/doi/pdf/10.1046/j.1365-2818.2001.00900.x.

[166] M. Otter, "Temperaturabhngigkeit der optischen Konstanten massiver Metalle," de, *Z. Physik*, vol. 161, no. 5, pp. 539–549, Oct. 1961.

[167] R. Rosei and D. W. Lynch, "Thermomodulation Spectra of Al, Au, and Cu," *Phys. Rev. B*, vol. 5, no. 10, pp. 3883–3894, May 1972, Publisher: American Physical Society.

[168] E. Colavita, A. Franciosi, C. Mariani, and R. Rosei, "Thermoreflectance test of W, Mo, and paramagnetic Cr band structures," *Phys. Rev. B*, vol. 27, no. 8, pp. 4684–4693, Apr. 1983, Publisher: American Physical Society.

[169] R. B. Wilson, B. A. Apgar, L. W. Martin, and D. G. Cahill, "Thermoreflectance of metal transducers for optical pump-probe studies of thermal properties," EN, *Opt. Express, OE*, vol. 20, no. 27, pp. 28 829–28 838, Dec. 2012, Publisher: Optica Publishing Group.

[170] V. Halt, A. Benabbas, and J.-Y. Bigot, "Optical response of periodically modulated nanostructures near the interband transition threshold of noble metals," EN, *Opt. Express, OE*, vol. 14, no. 7, pp. 2909–2920, Apr. 2006, Publisher: Optica Publishing Group.

[171] W. P. Dumke, "Interband Transitions and Maser Action," en, *Phys. Rev.*, vol. 127, no. 5, pp. 1559–1563, Sep. 1962.

[172] R. Rosei, E. Colavita, A. Franciosi, J. H. Weaver, and D. T. Peterson, "Electronic structure of the bcc transition metals: Thermoreflectance studies of bulk V, Nb, Ta, and alpha TaHx$," *Phys. Rev. B*, vol. 21, no. 8, pp. 3152–3157, Apr. 1980, Publisher: American Physical Society.

[173] P. Delfyett, L. Florez, N. Stoffel, T. Gmitter, N. Andreadakis, Y. Silberberg, J. Heritage, and G. Alphonse, "High-power ultrafast laser diodes," *IEEE Journal of Quantum Electronics*, vol. 28, no. 10, pp. 2203–2219, Oct. 1992, Conference Name: IEEE Journal of Quantum Electronics.

[174] U. Morgner, F. X. Krtner, S. H. Cho, Y. Chen, H. A. Haus, J. G. Fujimoto, E. P. Ippen, V. Scheuer, G. Angelow, and T. Tschudi, "Sub-two-cycle pulses from a Kerr-lens mode-locked Ti:sapphire laser," EN, *Opt. Lett., OL*, vol. 24, no. 6, pp. 411–413, Mar. 1999, Publisher: Optica Publishing Group.

[175] D. Brida, C. Manzoni, G. Cirmi, M. Marangoni, S. D. Silvestri, and G. Cerullo, "Generation of broadband mid-infrared pulses from an optical parametric amplifier," EN, *Opt. Express, OE*, vol. 15, no. 23, pp. 15 035–15 040, Nov. 2007, Publisher: Optica Publishing Group.

[176] J. A. Tomko, E. L. Runnerstrom, Y.-S. Wang, W. Chu, J. R. Nolen, D. H. Olson, K. P. Kelley, A. Cleri, J. Nordlander, J. D. Caldwell, O. V. Prezhdo, J.-P. Maria, and P. E. Hopkins, "Long-lived modulation of plasmonic absorption by ballistic thermal injection," en, *Nat. Nanotechnol.*, vol. 16, no. 1, pp. 47–51, Jan. 2021, Publisher: Nature Publishing Group.

[177] J. A. Tomko, K. Aryana, Y. Wu, G. Zhou, Q. Zhang, P. Wongwiset, V. Wheeler, O. V. Prezhdo, and P. E. Hopkins, "Ultrafast Charge Carrier Dynamics in Vanadium Dioxide, VO2: Nonequilibrium Contributions to the Photoinduced Phase Transitions," *J. Phys. Chem. Lett.*, vol. 16, no. 5, pp. 1312–1319, Feb. 2025, Publisher: American Chemical Society.

[178] A. Laturia, M. L. Van de Put, and W. G. Vandenberghe, "Dielectric properties of hexagonal boron nitride and transition metal dichalcogenides: From monolayer to bulk," *npj 2D Materials and Applications*, vol. 2, no. 1, Dec. 2018, Publisher: Nature Publishing Group.

[179] P. Jiang, X. Qian, R. Yang, and L. Lindsay, "Anisotropic thermal transport in bulk hexagonal boron nitride," *Phys. Rev. Mater.*, vol. 2, no. 6, p. 064 005, Jun. 2018, Publisher: American Physical Society.

[180] G. R. Jaffe, K. J. Smith, K. Watanabe, T. Taniguchi, M. G. Lagally, M. A. Eriksson, and V. W. Brar, "Thickness-Dependent Cross-Plane Thermal Conductivity Measurements of Exfoliated Hexagonal Boron Nitride," *ACS Appl. Mater. Interfaces*, vol. 15, no. 9, pp. 12 545–12 550, Mar. 2023, Publisher: American Chemical Society.

[181] M. He, G. R. Iyer, S. Aarav, S. S. Sunku, A. J. Giles, T. G. Folland, N. Sharac, X. Sun, J. Matson, S. Liu, J. H. Edgar, J. W. Fleischer, D. N. Basov, and J. D. Caldwell, "Ultrahigh-Resolution, Label-Free Hyperlens Imaging in the Mid-IR," *Nano Letters*, vol. 21, no. 19, pp. 7921–7928, Oct. 2021, Publisher: American Chemical Society.

[182] M. He, S. I. Halimi, T. G. Folland, S. S. Sunku, S. Liu, J. H. Edgar, D. N. Basov, S. M. Weiss, and J. D. Caldwell, "Guided Mid-IR and Near-IR Light within a Hybrid Hyperbolic-

Material/Silicon Waveguide Heterostructure," en, *Advanced Materials*, vol. 33, no. 11, p. 2 004 305, 2021, _eprint: https://onlinelibrary.wiley.com/doi/pdf/10.1002/adma.202004305.

[183] A. Fali, S. T. White, T. G. Folland, M. He, N. A. Aghamiri, S. Liu, J. H. Edgar, J. D. Caldwell, R. F. Haglund, and Y. Abate, "Refractive Index-Based Control of Hyperbolic Phonon-Polariton Propagation," en, *Nano Lett.*, vol. 19, no. 11, pp. 7725–7734, Nov. 2019.

[184] G. P. Srivastava, "Phonon conductivity of insulators and semiconductors," *Journal of Physics and Chemistry of Solids*, vol. 41, no. 4, pp. 357–368, Jan. 1980.

[185] A. Giri and P. E. Hopkins, "Role of interfacial mode coupling of optical phonons on thermal boundary conductance," en, *Sci Rep*, vol. 7, no. 1, p. 11 011, Sep. 2017, Publisher: Nature Publishing Group.

[186] D. Z. A. Chen, A. Narayanaswamy, and G. Chen, "Surface phonon-polariton mediated thermal conductivity enhancement of amorphous thin films," *Physical Review B - Condensed Matter and Materials Physics*, vol. 72, no. 15, Oct. 2005.

[187] Z. Pan, G. Lu, X. Li, J. R. McBride, R. Juneja, M. Long, L. Lindsay, J. D. Caldwell, and D. Li, "Remarkable heat conduction mediated by non-equilibrium phonon polaritons," *Nature*, vol. 623, no. 7986, pp. 307–312, Nov. 2023.

[188] E. Pop, "Energy dissipation and transport in nanoscale devices," *Nano Research*, vol. 3, no. 3, pp. 147–169, 2010, arXiv: 1003.4058 Publisher: Tsinghua University Press.

[189] G Chen, "Size and Interface Effects on Thermal Conductivity of Superlattices and Periodic Thin-Film Structures," *Journal of Heat Transfer*, vol. 119, no. 2, pp. 220–229, 1997.

[190] A. S. Barker, "Infrared Absorption of Localized Longitudinal-Optical Phonons," *Physical Review B*, vol. 7, no. 6, pp. 2507–2520, Apr. 1973, Publisher: Physical Review B.

[191] S. Adachi, *Optical Properties of Crystalline and Amorphous Semiconductors*. Springer US, 1999, Publication Title: Optical Properties of Crystalline and Amorphous Semiconductors.

[192] A. Poddubny, I. Iorsh, P. Belov, and Y. Kivshar, "Hyperbolic metamaterials," *Nature Photonics*, vol. 7, no. 12, pp. 958–967, Dec. 2013, arXiv: 1510.07137.

[193] J. D. Caldwell, A. V. Kretinin, Y. Chen, V. Giannini, M. M. Fogler, Y. Francescato, C. T. Ellis, J. G. Tischler, C. R. Woods, A. J. Giles, M. Hong, K. Watanabe, T. Taniguchi, S. A. Maier, and K. S. Novoselov, "Sub-diffractional volume-confined polaritons in the natural hyperbolic material hexagonal boron nitride," *Nature Communications*, vol. 5, Oct. 2014, Publisher: Nature Publishing Group.

[194] J. D. Caldwell, I. Aharonovich, G. Cassabois, J. H. Edgar, B. Gil, and D. N. Basov, "Photonics with hexagonal boron nitride," *Nature Reviews Materials*, vol. 4, no. 8, pp. 552–567, Aug. 2019, Publisher: Nature Publishing Group.

[195] S. Dai, Z. Fei, Q. Ma, A. S. Rodin, M. Wagner, A. S. McLeod, M. K. Liu, W. Gannett, W. Regan, K. Watanabe, T. Taniguchi, M. Thiemens, G. Dominguez, A. H. Castro Neto, A. Zettl, F. Keilmann, P. Jarillo-Herrero, M. M. Fogler, and D. N. Basov, "Tunable phonon polaritons in atomically thin van der Waals crystals of boron nitride," *Science*, vol. 343, no. 6175, pp. 1125–1129, Mar. 2014, Publisher: American Association for the Advancement of Science.

[196] R. Cusc, L. Arts, J. H. Edgar, S. Liu, G. Cassabois, and B. Gil, "Isotopic effects on phonon anharmonicity in layered van der Waals crystals: Isotopically pure hexagonal boron nitride," *Physical Review B*, vol. 97, no. 15, Apr. 2018, Publisher: American Physical Society.

[197] W. Ma, P. Alonso-Gonzlez, S. Li, A. Y. Nikitin, J. Yuan, J. Martn-Snchez, J. Taboada-Gutirrez, I. Amenabar, P. Li, S. Vlez, C. Tollan, Z. Dai, Y. Zhang, S. Sriram, K. Kalantar-Zadeh, S. T. Lee, R. Hillenbrand, and Q. Bao, "In-plane anisotropic and ultra-low-loss polaritons in a natural van der Waals crystal," *Nature*, vol. 562, no. 7728, pp. 557–562, Oct. 2018, Publisher: Nature Publishing Group.

[198] Z. Zheng, J. Chen, Y. Wang, X. Wang, X. Chen, P. Liu, J. Xu, W. Xie, H. Chen, S. Deng, and N. Xu, "Highly Confined and Tunable Hyperbolic Phonon Polaritons in Van Der Waals Semiconducting Transition Metal Oxides," *Advanced Materials*, vol. 30, no. 13, Mar. 2018, Publisher: Wiley-VCH Verlag.

[199] J. Taboada-Gutirrez, G. lvarez Prez, J. Duan, W. Ma, K. Crowley, I. Prieto, A. Bylinkin, M. Autore, H. Volkova, K. Kimura, T. Kimura, M. H. Berger, S. Li, Q. Bao, X. P. Gao, I. Errea, A. Y. Nikitin, R. Hillenbrand, J. Martn-Snchez, and P. Alonso-Gonzlez, "Broad

spectral tuning of ultra-low-loss polaritons in a van der Waals crystal by intercalation," *Nature Materials*, vol. 19, no. 9, pp. 964–968, Sep. 2020, Publisher: Nature Research.

[200] N. C. Passler, X. Ni, G. Hu, J. R. Matson, G. Carini, M. Wolf, M. Schubert, A. Al, J. D. Caldwell, T. G. Folland, and A. Paarmann, "Hyperbolic shear polaritons in low-symmetry crystals," *Nature*, vol. 602, no. 7898, pp. 595–600, Feb. 2022, Publisher: Nature Research.

[201] G. Hu, W. Ma, D. Hu, J. Wu, C. Zheng, K. Liu, X. Zhang, X. Ni, J. Chen, X. Zhang, Q. Dai, J. D. Caldwell, A. Paarmann, A. Al, P. Li, and C. W. Qiu, "Real-space nanoimaging of hyperbolic shear polaritons in a monoclinic crystal," *Nature Nanotechnology*, Jan. 2022, Publisher: Nature Research.

[202] G. Pavlidis, J. J. Schwartz, J. Matson, T. Folland, S. Liu, J. H. Edgar, J. D. Caldwell, and A. Centrone, "Experimental confirmation of long hyperbolic polariton lifetimes in monoisotopic (10B) hexagonal boron nitride at room temperature," *APL Materials*, vol. 9, no. 9, Sep. 2021, Publisher: American Institute of Physics Inc.

[203] G. Ni, A. S. McLeod, Z. Sun, J. R. Matson, C. F. B. Lo, D. A. Rhodes, F. L. Ruta, S. L. Moore, R. A. Vitalone, R. Cusco, L. Arts, L. Xiong, C. R. Dean, J. C. Hone, A. J. Millis, M. M. Fogler, J. H. Edgar, J. D. Caldwell, and D. N. Basov, "Long-Lived Phonon Polaritons in Hyperbolic Materials," *Nano Letters*, vol. 21, no. 13, pp. 5767–5773, Jul. 2021, Publisher: American Chemical Society.

[204] P. Li, M. Lewin, A. V. Kretinin, J. D. Caldwell, K. S. Novoselov, T. Taniguchi, K. Watanabe, F. Gaussmann, and T. Taubner, "Hyperbolic phonon-polaritons in boron nitride for near-field optical imaging and focusing," *Nature Communications*, vol. 6, Jun. 2015, Publisher: Nature Publishing Group.

[205] S. Dai, Q. Ma, T. Andersen, A. S. McLeod, Z. Fei, M. K. Liu, M. Wagner, K. Watanabe, T. Taniguchi, M. Thiemens, F. Keilmann, P. Jarillo-Herrero, M. M. Fogler, and D. N. Basov, "Subdiffractional focusing and guiding of polaritonic rays in a natural hyperbolic material," *Nature Communications*, vol. 6, Apr. 2015, Publisher: Nature Publishing Group.

[206] X. Wu and C. Fu, "Near-field radiative heat transfer between uniaxial hyperbolic media: Role of volume and surface phonon polaritons," *Journal of Quantitative Spectroscopy and Radiative Transfer*, vol. 258, Jan. 2021, Publisher: Elsevier Ltd.

[207] K. J. Tielrooij, N. C. Hesp, A. Principi, M. B. Lundeberg, E. A. Pogna, L. Banszerus, Z. Mics, M. Massicotte, P. Schmidt, D. Davydovskaya, D. G. Purdie, I. Goykhman, G. Soavi, A. Lombardo, K. Watanabe, T. Taniguchi, M. Bonn, D. Turchinovich, C. Stampfer, A. C. Ferrari, G. Cerullo, M. Polini, and F. H. Koppens, "Out-of-plane heat transfer in van der Waals stacks through electron-hyperbolic phonon coupling," *Nature Nanotechnology*, vol. 13, no. 1, pp. 41–46, Jan. 2018, arXiv: 1702.03766 Publisher: Nature Publishing Group.

[208] W. Yang, S. Berthou, X. Lu, Q. Wilmart, A. Denis, M. Rosticher, T. Taniguchi, K. Watanabe, G. Fve, J. M. Berroir, G. Zhang, C. Voisin, E. Baudin, and B. Plaais, "A graphene Zener-Klein transistor cooled by a hyperbolic substrate," *Nature Nanotechnology*, vol. 13, no. 1, pp. 47–52, Jan. 2018, arXiv: 1702.02829 Publisher: Nature Publishing Group.

[209] H. Wang, J. H. Strait, P. A. George, S. Shivaraman, V. B. Shields, M. Chandrashekhar, J. Hwang, F. Rana, M. G. Spencer, C. S. Ruiz-Vargas, and J. Park, "Ultrafast relaxation dynamics of hot optical phonons in graphene," *Applied Physics Letters*, vol. 96, no. 8, 2010, arXiv: 0909.4912.

[210] A. Tokmakoff, B. Sauter, and M. D. Fayer, "Temperature-dependent vibrational relaxation in polyatomic liquids: Picosecond infrared pump-probe experiments," *The Journal of Chemical Physics*, vol. 100, no. 12, pp. 9035–9043, 1994.

[211] P. L. Kapitza, "Heat Transfer and Superfluidity of Helium II," *Physical Reviews*, vol. 60, no. 4, pp. 354–355, 1941.

[212] D. Thompson, L. Zhu, E. Meyhofer, and P. Reddy, "Nanoscale radiative thermal switching via multi-body effects," *Nature Nanotechnology*, vol. 15, no. 2, pp. 99–104, Feb. 2020, Publisher: Nature Research.

[213] S. Guddala, F. Komissarenko, S. Kiriushechkina, A. Vakulenko, M. Li, V. M. Menon, A. Al, and A. B. Khanikaev, "Topological phonon-polariton funneling in midinfrared metasur-

faces," *Science*, vol. 374, no. 6564, pp. 225–227, Oct. 2021, Publisher: American Association for the Advancement of Science.

[214] W. Ma, G. Hu, D. Hu, R. Chen, T. Sun, X. Zhang, Q. Dai, Y. Zeng, A. Al, C. W. Qiu, and P. Li, "Ghost hyperbolic surface polaritons in bulk anisotropic crystals," *Nature*, vol. 596, no. 7872, pp. 362–366, Aug. 2021, Publisher: Nature Research.

[215] J. D. Caldwell, L. Lindsay, V. Giannini, I. Vurgaftman, T. L. Reinecke, S. A. Maier, and O. J. Glembocki, "Low-loss, infrared and terahertz nanophotonics using surface phonon polaritons," *Nanophotonics*, vol. 4, no. 1, pp. 44–68, Jan. 2015, Publisher: Walter de Gruyter GmbH.

[216] S. Foteinopoulou, G. C. R. Devarapu, G. S. Subramania, S. Krishna, and D. Wasserman, "Phonon-polaritonics: Enabling powerful capabilities for infrared photonics," *Nanophotonics*, 2019, Publisher: De Gruyter.

[217] E. Yoxall, M. Schnell, A. Y. Nikitin, O. Txoperena, A. Woessner, M. B. Lundeberg, F. Casanova, L. E. Hueso, F. H. Koppens, and R. Hillenbrand, "Direct observation of ultraslow hyperbolic polariton propagation with negative phase velocity," *Nature Photonics*, vol. 9, no. 10, pp. 674–678, Sep. 2015, Publisher: Nature Publishing Group.

[218] J. D. Caldwell, I. Vurgaftman, and J. G. Tischler, "Mid-infrared nanophotonics: Probing hyperbolic polaritons," *Nature Photonics*, vol. 9, no. 10, pp. 638–640, Sep. 2015, Publisher: Nature Publishing Group.

[219] E. J. Tervo, O. S. Adewuyi, J. S. Hammonds, and B. A. Cola, "High thermal conductivity in polaritonic SiO2 nanoparticle beds," *Materials Horizons*, vol. 3, no. 5, pp. 434–441, Sep. 2016, Publisher: Royal Society of Chemistry.

[220] D. Thompson, L. Zhu, R. Mittapally, S. Sadat, Z. Xing, P. McArdle, M. M. Qazilbash, P. Reddy, and E. Meyhofer, "Hundred-fold enhancement in far-field radiative heat transfer over the blackbody limit," *Nature*, vol. 561, no. 7722, pp. 216–221, Sep. 2018, Publisher: Nature Publishing Group.

[221] A. Narayanaswamy, S. Shen, L. Hu, X. Chen, and G. Chen, "Breakdown of the Planck blackbody radiation law at nanoscale gaps," *Applied Physics A: Materials Science and Processing*, vol. 96, no. 2, pp. 357–362, Aug. 2009.

[222] A. Fiorino, D. Thompson, L. Zhu, B. Song, P. Reddy, and E. Meyhofer, "Giant Enhancement in Radiative Heat Transfer in Sub-30 nm Gaps of Plane Parallel Surfaces," *Nano Letters*, vol. 18, no. 6, pp. 3711–3715, Jun. 2018, Publisher: American Chemical Society.

[223] S. Shen, A. Narayanaswamy, and G. Chen, "Surface phonon polaritons mediated energy transfer between nanoscale gaps," *Nano Letters*, vol. 9, no. 8, pp. 2909–2913, Aug. 2009.

[224] D. P. Sellan, E. S. Landry, K. Sasihithlu, A. Narayanaswamy, A. J. McGaughey, and C. H. Amon, "Phonon transport across a vacuum gap," *Physical Review B - Condensed Matter and Materials Physics*, vol. 85, no. 2, Jan. 2012.

[225] B. Song, Y. Ganjeh, S. Sadat, D. Thompson, A. Fiorino, V. Fernndez-Hurtado, J. Feist, F. J. Garcia-Vidal, J. C. Cuevas, P. Reddy, and E. Meyhofer, "Enhancement of near-field radiative heat transfer using polar dielectric thin films," *Nature Nanotechnology*, vol. 10, no. 3, pp. 253–258, Mar. 2015, Publisher: Nature Publishing Group.

[226] R. J. Warzoha, A. A. Wilson, B. F. Donovan, N. Donmezer, A. Giri, P. E. Hopkins, S. Choi, D. Pahinkar, J. Shi, S. Graham, Z. Tian, and L. Ruppalt, "Applications and Impacts of Nanoscale Thermal Transport in Electronics Packaging," *Journal of Electronic Packaging, Transactions of the ASME*, vol. 143, no. 2, Jun. 2021, Publisher: American Society of Mechanical Engineers (ASME).

[227] K. Aryana, J. T. Gaskins, J. Nag, D. A. Stewart, Z. Bai, S. Mukhopadhyay, J. C. Read, D. H. Olson, E. R. Hoglund, J. M. Howe, A. Giri, M. K. Grobis, and P. E. Hopkins, "Interface controlled thermal resistancesof ultra-thin chalcogenide-based phase change memory devices," *Nature Communications*, vol. 12, no. 1, Dec. 2021, arXiv: 2011.05492 Publisher: Nature Research.

[228] A. Fiorino, L. Zhu, D. Thompson, R. Mittapally, P. Reddy, and E. Meyhofer, "Nanogap near-field thermophotovoltaics," *Nature Nanotechnology*, vol. 13, no. 9, pp. 806–811, Sep. 2018, Publisher: Nature Publishing Group.

[229] J. A. Tomko, S. Kumar, R. Sundararaman, and P. E. Hopkins, "Temperature dependent electron-phonon coupling of Au resolved via lattice dynamics measured with sub-picosecond infrared pulses," *Journal of Applied Physics*, vol. 129, no. 19, May 2021, Publisher: American Institute of Physics Inc.

[230] A. Howes, J. R. Nolen, J. D. Caldwell, and J. Valentine, "Near-Unity and Narrowband Thermal Emissivity in Balanced Dielectric Metasurfaces," *Advanced Optical Materials*, vol. 8, no. 4, Feb. 2020, Publisher: Wiley-VCH Verlag.

[231] P. Kumar, Y. S. Chauhan, A. Agarwal, and S. Bhowmick, "Thickness and Stacking Dependent Polarizability and Dielectric Constant of Graphene-Hexagonal Boron Nitride Composite Stacks," *Journal of Physical Chemistry C*, vol. 120, no. 31, pp. 17 620–17 626, Aug. 2016, Publisher: American Chemical Society.

[232] T. Low, A. Chaves, J. D. Caldwell, A. Kumar, N. X. Fang, P. Avouris, T. F. Heinz, F. Guinea, L. Martin-Moreno, and F. Koppens, "Polaritons in layered two-dimensional materials," *Nature Materials*, vol. 16, no. 2, pp. 182–194, Feb. 2017, Publisher: Nature Publishing Group.

[233] T. G. Folland, T. W. W. Ma, J. R. Matson, J. R. Nolen, S. Liu, K. Watanabe, T. Taniguchi, J. H. Edgar, T. Taubner, and J. D. Caldwell, "Probing hyperbolic polaritons using infrared attenuated total reflectance micro-spectroscopy," en, *MRS Communications*, vol. 8, no. 4, pp. 1418–1425, Dec. 2018.

[234] S. Dai, Q. Ma, Y. Yang, J. Rosenfeld, M. D. Goldflam, A. McLeod, Z. Sun, T. I. Andersen, Z. Fei, M. Liu, Y. Shao, K. Watanabe, T. Taniguchi, M. Thiemens, F. Keilmann, P. Jarillo-Herrero, M. M. Fogler, and D. N. Basov, "Efficiency of Launching Highly Confined Polaritons by Infrared Light Incident on a Hyperbolic Material," *Nano Lett.*, vol. 17, no. 9, pp. 5285–5290, Sep. 2017, Publisher: American Chemical Society.

[235] Y. V. Bludov and M. I. Vasilevskiy, *ATR excitation of surface polaritons at the interface between a metal and a layer of nanocrystal quantum dots*, en, arXiv:1102.2320 [cond-mat], Feb. 2011.

[236] M. Francoeur, M. P. Meng, and R. Vaillon, "Near-field radiative heat transfer enhancement via surface phonon polaritons coupling in thin films," *Applied Physics Letters*, vol. 93, no. 4, p. 043 109, Jul. 2008.

[237] C. J. Foss and Z. Aksamija, "Quantifying thermal boundary conductance of 2D-3D interfaces," *2D Materials*, vol. 6, no. 2, Feb. 2019, Publisher: IOP Publishing Ltd.

[238] S. Basu and Z. M. Zhang, "Maximum energy transfer in near-field thermal radiation at nanometer distances," *Journal of Applied Physics*, vol. 105, no. 9, p. 093 535, May 2009.

[239] B. Gil, G. Cassabois, R. Cusco, G. Fugallo, and L. Artus, "Boron nitride for excitonics, nano photonics, and quantum technologies," *Nanophotonics*, vol. 9, no. 11, pp. 3483–3504, Sep. 2020, Publisher: De Gruyter Open Ltd.

[240] T. Tohei, A. Kuwabara, F. Oba, and I. Tanaka, "Debye temperature and stiffness of carbon and boron nitride polymorphs from first principles calculations," en, *Phys. Rev. B*, vol. 73, no. 6, p. 064 304, Feb. 2006.

[241] G. Lu, M. Tadjer, J. D. Caldwell, and T. G. Folland, "Multi-frequency coherent emission from superstructure thermal emitters," *Applied Physics Letters*, vol. 118, no. 14, Apr. 2021, Publisher: American Institute of Physics Inc.

[242] G. Lu, C. R. Gubbin, J. R. Nolen, T. Folland, M. J. Tadjer, S. de Liberato, and J. D. Caldwell, "Engineering the spectral and spatial dispersion of thermal emission via polariton-phonon strong coupling," *Nano Letters*, vol. 21, no. 4, pp. 1831–1838, Feb. 2021, Publisher: American Chemical Society.

[243] T. Q. Vuong, S. Liu, A. Van Der Lee, R. Cusc, L. Arts, T. Michel, P. Valvin, J. H. Edgar, G. Cassabois, and B. Gil, "Isotope engineering of van der Waals interactions in hexagonal boron nitride," *Nature Materials 2017 17:2*, vol. 17, no. 2, pp. 152–158, Dec. 2017, Publisher: Nature Publishing Group.

[244] S. Liu, R. He, L. Xue, J. Li, B. Liu, and J. H. Edgar, "Single Crystal Growth of Millimeter-Sized Monoisotopic Hexagonal Boron Nitride," *Chemistry of Materials*, vol. 30, no. 18, pp. 6222–6225, Sep. 2018, Publisher: American Chemical Society.

[245] Z. Fei, A. S. Rodin, G. O. Andreev, W. Bao, A. S. McLeod, M. Wagner, L. M. Zhang, Z. Zhao, M. Thiemens, G. Dominguez, M. M. Fogler, A. H. C. Neto, C. N. Lau, F. Keilmann, and D. N. Basov, "Gate-tuning of graphene plasmons revealed by infrared nano-imaging," en, *Nature*, vol. 487, no. 7405, pp. 82–85, Jul. 2012, Publisher: Nature Publishing Group.

[246] J. Chen, M. Badioli, P. Alonso-Gonzlez, S. Thongrattanasiri, F. Huth, J. Osmond, M. Spasenovi, A. Centeno, A. Pesquera, P. Godignon, A. Zurutuza Elorza, N. Camara, F. J. G. de Abajo, R. Hillenbrand, and F. H. L. Koppens, "Optical nano-imaging of gate-tunable graphene plasmons," en, *Nature*, vol. 487, no. 7405, pp. 77–81, Jul. 2012, Publisher: Nature Publishing Group.

[247] Z. Liu, H. Lee, Y. Xiong, C. Sun, and X. Zhang, "Far-Field Optical Hyperlens Magnifying Sub-Diffraction-Limited Objects," *Science*, vol. 315, no. 5819, pp. 1686–1686, Mar. 2007, Publisher: American Association for the Advancement of Science.

[248] P. Shekhar, J. Atkinson, and Z. Jacob, "Hyperbolic metamaterials: Fundamentals and applications," en, *Nano Convergence*, vol. 1, no. 1, p. 14, Jun. 2014.

[249] W. Wang, H. Xing, L. Fang, Y. Liu, J. Ma, L. Lin, C. Wang, and X. Luo, "Far-field imaging device: Planar hyperlens with magnification using multi-layer metamaterial," *Optics express*, vol. 16, no. 25, pp. 21 142–21 148, 2008, Publisher: Optica Publishing Group.

[250] W. Gao, C. F. Doiron, X. Li, J. Kono, and G. V. Naik, "Macroscopically Aligned Carbon Nanotubes as a Refractory Platform for Hyperbolic Thermal Emitters," en, *ACS Photonics*, vol. 6, no. 7, pp. 1602–1609, Jul. 2019.

[251] M. M. Hossain, B. Jia, and M. Gu, "A metamaterial emitter for highly efficient radiative cooling," *Adv. Opt. Mater*, vol. 3, no. 8, pp. 1047–1051, 2015.

[252] A. P. Raman, M. A. Anoma, L. Zhu, E. Rephaeli, and S. Fan, "Passive radiative cooling below ambient air temperature under direct sunlight," en, *Nature*, vol. 515, no. 7528, pp. 540–544, Nov. 2014.

[253] Z. Yu, N. P. Sergeant, T. Skauli, G. Zhang, H. Wang, and S. Fan, "Enhancing far-field thermal emission with thermal extraction," en, *Nat Commun*, vol. 4, no. 1, p. 1730, Apr. 2013, Publisher: Nature Publishing Group.

[254] Y. Qu, M. Pan, and M. Qiu, "Directional and Spectral Control of Thermal Emission and Its Application in Radiative Cooling and Infrared Light Sources," en, *Phys. Rev. Applied*, vol. 13, no. 6, p. 064 052, Jun. 2020.

[255] Z. Chen, L. Zhu, A. Raman, and S. Fan, "Radiative cooling to deep sub-freezing temperatures through a 24-h daynight cycle," en, *Nat Commun*, vol. 7, no. 1, p. 13 729, Dec. 2016, Publisher: Nature Publishing Group.

[256] J. B. Pendry, D. Schurig, and D. R. Smith, "Controlling Electromagnetic Fields," *Science*, vol. 312, no. 5781, pp. 1780–1782, Jun. 2006, Publisher: American Association for the Advancement of Science.

[257] C. L. Cortes, W Newman, S Molesky, and Z Jacob, "Quantum nanophotonics using hyperbolic metamaterials," en, *J. Opt.*, vol. 14, no. 6, p. 063 001, Jun. 2012.

[258] A. J. Cleri, J. R. Nolen, K. G. Wirth, M. He, E. L. Runnerstrom, K. P. Kelley, J. Nordlander, T. Taubner, T. G. Folland, J.-P. Maria, and J. D. Caldwell, "Tunable, Homoepitaxial Hyperbolic Metamaterials Enabled by High Mobility CdO," en, *Advanced Optical Materials*, vol. 11, no. 1, p. 2 202 137, 2023.

[259] E. L. Runnerstrom, K. P. Kelley, T. G. Folland, J. R. Nolen, N. Engheta, J. D. Caldwell, and J.-P. Maria, "Polaritonic Hybrid-Epsilon-near-Zero Modes: Beating the Plasmonic Confinement vs Propagation-Length Trade-Off with Doped Cadmium Oxide Bilayers," en, *Nano Lett.*, vol. 19, no. 2, pp. 948–957, Feb. 2019.

[260] K. P. Kelley, E. L. Runnerstrom, E. Sachet, C. T. Shelton, E. D. Grimley, A. Klump, J. M. LeBeau, Z. Sitar, J. Y. Suen, W. J. Padilla, and J.-P. Maria, "Multiple Epsilon-Near-Zero Resonances in Multilayered Cadmium Oxide: Designing Metamaterial-Like Optical Properties in Monolithic Materials," *ACS Photonics*, vol. 6, no. 5, pp. 1139–1145, May 2019, Publisher: American Chemical Society.

[261] M. He, J. R. Nolen, J. Nordlander, A. Cleri, N. S. McIlwaine, Y. Tang, G. Lu, T. G. Folland, B. A. Landman, J.-P. Maria, and J. D. Caldwell, "Deterministic inverse design of Tamm plasmon thermal emitters with multi-resonant control," en, *Nat. Mater.*, vol. 20, no. 12, pp. 1663–1669, Dec. 2021.

[262] X. Zhang, C. Li, F. Xu, J. Zhang, C. Gao, Z. Cheng, Y. Wu, X. Liu, A. Zerr, and H. Huang, "Sound Velocity Anisotropy and Single-Crystal Elastic Moduli of MgO to 43 GPa," en, *Journal of Geophysical Research: Solid Earth*, vol. 128, no. 6, e2022JB026311, 2023, _eprint: https://onlinelibrary.wiley.com/doi/pdf/10.1029/2022JB026311.

[263] J. Bala, V. Bhalla, D. Singh, C. P. Yadav, and D. K. Pandey, "Elastic and ultrasonic properties of cadmium oxide," *Journal of Pure and Applied*, p. 78,

[264] M. Habibi, S. C. Yelishala, Y. Zhu, E. J. Tervo, M. A. Steiner, and L. Cui, "Enhanced power density in zero-vacuum-gap thermophotovoltaic devices," *Energy & Environmental Science*, vol. 18, no. 3, pp. 1514–1523, 2025.

[265] G. Kresse, J. Furthmller, and J. Hafner, "Theory of the crystal structures of selenium and tellurium: The effect of generalized-gradient corrections to the local-density approximation," *Phys. Rev. B*, vol. 50, no. 18, pp. 13 181–13 185, Nov. 1994, Publisher: American Physical Society.

[266] W. M. Haynes, *CRC Handbook of Chemistry and Physics*, en. CRC Press, Jun. 2016, Google-Books-ID: VVezDAAAQBAJ.